Title

Atomic and Molecular Photoelectron and Auger Electron Spectroscopy Studies Using Synchrotron Radiation

Permalink

https://escholarship.org/uc/item/166640nb

Author

Southworth, Stephen H

Publication Date

1982

Lawrence Berkeley Laboratory
UNIVERSITY OF CALIFORNIA

Materials & Molecular Research Division

RECEIVED
LAWRENCE
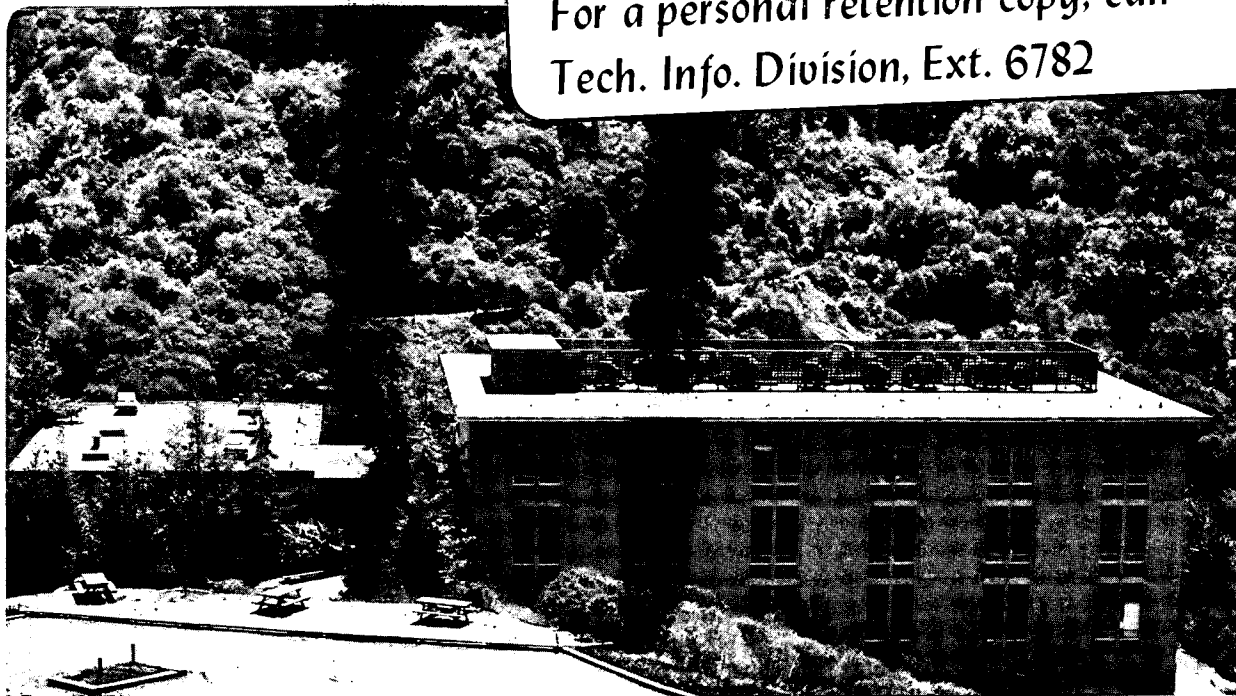BERKELEY LABORATORY

8 1982

LIBRARY AND
DOCUMENTS SECTION

ATOMIC AND MOLECULAR PHOTOELECTRON AND AUGER
ELECTRON SPECTROSCOPY STUDIES USING SYNCHROTRON
RADIATION

Stephen H. Southworth
(Ph.D. thesis)

January 1982

DISCLAIMER

ATOMIC AND MOLECULAR PHOTOELECTRON AND AUGER ELECTRON SPECTROSCOPY STUDIES USING SYNCHROTRON RADIATION

Stephen H. Southworth
Ph.D. Thesis

January 1982

Atomic and Molecular Photoelectron
and Auger Electron Spectroscopy Studies
using Synchrotron Radiation

Stephen Hunt Southworth

Materials and Molecular Research Division
Lawrence Berkeley Laboratory

and

Department of Chemistry
University of California
Berkeley, California 94720

Abstract

Electron spectroscopy, combined with synchrotron radiation, was used to measure the angular distributions of photoelectrons and Auger electrons from atoms and molecules as functions of photon energy. The branching ratios and partial cross sections were also measured in certain cases. By comparison with theoretical calculations, the experimental results are interpreted in terms of the characteristic electronic structure and ionization dynamics of the atomic or molecular sample.

The time structure of the synchrotron radiation source was used to record time-of-flight (TOF) spectra of the ejected electrons. The "double-angle-TOF" method for the measurement of photoelectron angular distributions is discussed. This technique offers the advantages of increased electron collection efficiency and the elimination of certain systematic errors.

Several results were obtained for Xe using photon energies in the range $h\nu = 60$–190 eV, where excitation and ionization of the inner-subshell 4d electrons dominates. The 4d asymmetry parameter β exhibits strong oscillations with energy, in agreement with several theoretical calculations. As predicted, the 5p asymmetry parameter was observed to deviate strongly from that calculated using the independent-electron model, due to intershell correlation with the 4d electrons.

The Xe $N_{4,5}OO$ Auger electrons were produced with energy-dependent, anisotropic angular distributions, resulting from alignment of Xe^{+} by photoionization. The theoretical analysis of Auger electron angular distributions is discussed, and theoretical calculations are compared with experiment. Relatively large asymmetries β were measured for $N_{4,5}OO$ Auger electrons near the 4d ionization threshold, in good agreement with theory. In addition, Auger electron peaks were observed to shift and broaden at photon energies near the ionization threshold, as a result of post-collision interaction. The measured shifts of the $N_5O_1O_1\ ^1S_0$ line are in good agreement with previous measurements and theory.

Electron spectra were recorded through the energy region of the Xe $4d^9 5s^2 5p^6 (^2D_{5/2,3/2})np\ ^1P_1$ autoionizing resonances. Though the excitation bandpass was somewhat larger than the widths of the resonances, certain strong qualitative features were observed. As expected, these $4d \rightarrow np$ resonances decay predominantly by the Auger process, and the 5p and 5s photoionization cross sections are relatively

unaffected. However, pronounced resonance structure appears in the asymmetry parameters β for $5p_{3/2}$ and $5p_{1/2}$ photoelectrons. The 5s photoelectrons are produced with large asymmetries, $\beta \simeq 1.8$–2.0, and no effect of the 4d → np resonances was observed.

The photoelectron asymmetry parameters β of H_2 and D_2 were measured over $h\nu = 19$–27 eV and compared with previous measurements and several theoretical calculations. A few of the theoretical calculations are in good agreement with experiment, but most of them predict asymmetries which are too large. Essentially identical β values were measured for H_2 and D_2. This result is discussed in terms of differences which could arise due to vibrational and rotational structure.

Partial photoionization cross sections and photoelectron asymmetry parameters were measured for the valence orbitals of NO over the energy range $h\nu = 16$–31 eV. The results are compared with previous measurements and with theoretical curves based on the multiple-scattering model. Maxima observed in the partial cross sections are attributed to continuum shape resonances. The multiple-scattering model calculations predict the observed photoelectron asymmetries of the 5σ and 1π orbitals very well, but the theoretical asymmetry curves are shifted strongly from the measured β values for the 2π and 4σ orbitals. The π molecular orbitals are observed to produce qualitatively different photoelectron asymmetry curves than do the σ orbitals.

Table of Contents

I. THEORY

A. Introduction

Experimental measurements of the energies, intensities, and angular distributions of photoelectrons and Auger electrons, when combined with theoretical calculations, can provide a sensitive probe of electronic structure and dynamics. The full potential of electron spectroscopy is realized only when measurements and theoretical calculations are made over a range of photon energies, as the spectral variation of cross sections and angular distributions characterizes the electronic structure and ionization dynamics. In this thesis work, electron spectroscopy combined with the tunable VUV continuum provided by synchrotron radiation was used to make wavelength-dependent measurements of photoelectron and Auger electron angular distributions and of branching ratos and partial cross sections for photoionization and Auger processes.

Close interaction between theory and experiment is emphasized in photoionization studies. Theoretical calculations provide a basis for interpretation of experimental results; experimental measurements provide a sensitive test of the accuracy of theoretical models. Comparison with experiment of a set of theoretical calculations made in varying degrees of approximation allows a determination of the structural and dynamical factors which are necessary for an accurate description of the photoionization process.

Considerable progress has been made in atomic photoionization studies, where increasingly accurate knowledge of many-electron and

relativistic interactions has emerged.[1-4] Molecular photoionization
studies are at an earlier stage. On the theoretical side, there is
difficulty in calculating accurate continuum wavefunctions for the
multi-center molecular field. Experimentally, it is desirable to
resolve the vibrational structure in molecular photoelectron spectra,
which generally requires a high resolution electron energy analyzer.
Still, progress has been made, both theoretically[5-7], and
experimentally.[3,8-10]

This thesis presents measurements of partial photoionization
cross sections and photoelectron angular distributions from Xe, H_2,
D_2, and NO. Also measured were the angular distributions of Xe
$N_{4,5}OO$ Auger electrons which are produced by core-hole decay
following inner-shell photoionization. Theoretical background is
given in the remainder of this chapter. The experimental apparatus
and methods are described in Chapter II. The results are discussed in
comparison with theoretical calculations in Chapters III-V.

B.   Photoelectron Angular Distributions

In a photoionization experiment, a monochromatic beam of photons
having energy $h\nu$ is passed through an atomic (or molecular) target
gas. Usually the target atoms are in the neutral ground state Ψ_0.
In the photoionization process, an electron is ejected and the atom is
left in an ionic state:

$$h\nu + A(\Psi_0) \rightarrow A^+(\Psi_j^+) + e^-, \tag{1}$$

where Ψ_j^+ represents the jth ionic state. The energy level difference,

$$I_j = E_j^+ - E_0 \quad , \tag{2}$$

between the ground and ionic states is called the ionization energy for production of the jth ionic state. Energy conservation requires that the photoelectron be ejected with a definite kinetic energy

$$\epsilon_j = h\nu - I_j \quad . \tag{3}$$

In general, all of the energetically accessible ionic states (those with $I_j < h\nu$) are produced in a photoionization experiment, and photoelectrons are ejected with distinctive kinetic energies determined by Eq. (3). In the technique of photoelectron spectroscopy, the ejected electrons are energy-analyzed and counted. One obtains a spectrum of photoelectron peaks at characteristic energies, which correspond to the various ionic states. In a one-electron picture, peaks in the photoelectron spectrum are associated with photoemission from the occupied orbitals of the ground state configuration.[11]

A single photon energy suffices to measure ionization energies. However, for a given final state, the photoionization process is further characterized by an energy-dependent cross section and photoelectron angular distribution. The form of the angular distribution of photoelectrons, or of any photofragment, is determined by conservation of angular momentum and parity. This topic has been discussed and

developed by several authors (for example, Refs. 12-15). Angular momentum and parity conservation in the general photoionization process are expressed in the following equations:

$$h\nu(j_r = 1, \pi_r = -1) + A(J_0, \pi_0) \rightarrow A^+(J_c, \pi_c) + e^-(s\ell, \pi_e = (-1)^\ell) \quad (4)$$

$$\vec{J} = \vec{J}_r + \vec{J}_0 = \vec{J}_c + \vec{s} + \vec{\ell} \quad (5)$$

$$\pi = \pi_r \pi_0 = \pi_c \pi_e \quad . \quad (6)$$

In Eq. (4), the values $j_r = 1$ and $\pi_r = -1$ specify that the photon absorption occurs via the electric-dipole interaction, and the other angular momentum and parity symbols are defined implicitly. Assuming pure electric dipole photoionization of randomly oriented target atoms or molecules (gas-phase experiment) by a linearly-polarized photon beam, the differential cross section can be expressed in the form

$$\frac{d\sigma(\epsilon)}{d\Omega} = \frac{\sigma(\epsilon)}{4\pi} [1 + \beta(\epsilon) P_2(\cos\theta)] \quad . \quad (7)$$

Here $\sigma(\epsilon)$ is the angle-integrated partial cross section, $P_2(\cos\theta) = (1/2)(3 \cos^2\theta - 1)$, θ is the photoelectron ejection angle with respect to the photon polarization vector, ϵ is the photoelectron energy, and $\beta(\epsilon)$ is the photoelectron asymmetry parameter. The requirement that the differential cross section be non-negative restricts the allowed values of the asymmetry parameter to the range $-1 \leq \beta(\epsilon) \leq 2$.

Eq. (7) shows that the angular distribution is completely characterized by a single parameter $\beta(\epsilon)$, as a consequence of adopting the dipole approximation. This approximation is quite good at low photon energies, but at higher energies (generally, several hundred eV) a more complicated form of the angular distribution can result due to the contributions of additional multipole components.[1,13,16] In the present work, photon energies $h\nu \leq 330$ eV were used, and the measurements were interpreted using Eq. (7), i.e., the dipole approximation was assumed to be valid.

The observable parameters $\sigma(\epsilon)$ and $\beta(\epsilon)$ are determined by the electronic structure and photoionization dynamics of the atom or molecule. In theoretical studies, the continuum wavefunction is expanded in terms of angular momentum wavefunctions (alternative values of the orbital momentum ℓ in Eq. (4)), and dipole transition amplitudes are calculated for each partial wave.[14,17,18] Thus, theoretical studies show how $\sigma(\epsilon)$ and $\beta(\epsilon)$ are determined by the energy-dependent dipole transition amplitudes. An important result of the theoretical analysis is that the angle-integrated cross section $\sigma(\epsilon)$ depends only on the squares of the dipole matrix elements, while the asymmetry parameter $\beta(\epsilon)$ depends in addition, through interference terms, on the signs of the matrix elements and on the relative phases of the partial waves. The sensitivity of $\beta(\epsilon)$ to the continuum wave phase shifts has been emphasized.[1,17]

A clarification and simplification of the $\beta(\epsilon)$ problem has been obtained in several cases by use of the angular momentum transfer formulation of angular distributions.[15] The angular momentum transfer for the general photoionization process (Eq. (4)) is defined by

$$\vec{J}_t = \vec{J}_c + \vec{s} - \vec{J}_0 = \vec{J}_r - \vec{\ell} \quad . \tag{8}$$

In the angular momentum transfer formulation, the photoionization process is described in terms of contributions from the alternative values of j_t which are allowed by angular momentum and parity conservation (Eqs. (5) and (6)). The asymmetry parameter $\beta(\epsilon)$ is expressed as a weighted average over values $\beta(j_t)$ associated with each allowed j_t value. The power of the j_t-formulation lies in showing how particular dynamical factors in the photoionization process are associated with particular j_t and $\beta(j_t)$ values. The observed $\beta(\epsilon)$ can then be interpreted as a measure of the relative importance of particular dynamical factors. Among the systems to which the j_t-formulation has been applied are the photoionization of H_2[19] and of the Xe 5s subshell.[20] Measurements for these systems will be presented in the following chapters of this thesis. A review of the j_t-formulation is given in Ref. 1.

C. Auger Electron Angular Distributions

Photoemission from an inner-shell of an atom or molecule leaves an excited ionic state which can decay by an Auger process: an outer-shell electron fills the inner vacancy and a second outer-shell

electron is ejected, creating a doubly-charged ionic state. Some reference works on the Auger effect are listed in Refs. 21-24. Here, the relevant theoretical background will be described for the case of the Xe $N_{4,5}OO$ Auger transitions, for which measurements will be presented in Chapter III.

In the two-step model of the Auger process the decay of the excited ionic state is considered independent of the excitation process. In the present example, excitation is produced by photoionization of the Xe 4d subshell:

$$h\nu + Xe(4d^{10}5s^{2}5p^{6} \, ^{1}S_{0}) \rightarrow Xe^{+}(4d^{9}5s^{2}5p^{6} \, ^{2}D_{3/2,5/2}) + e^{-} \quad . \quad (9)$$
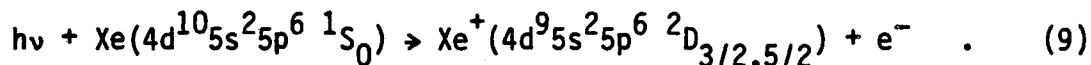
In the subsequent Auger process, a 5p or 5s electron fills the 4d hole, and a second O-shell electron is ejected. The Auger effect is a type of autoionization process, i.e., the transition is caused by the electron-electron Coulomb interaction. The primary Auger transitions are described by the following processes:

$$Xe^{+}(4d^{9}5s^{2}5p^{6} \, ^{2}D_{3/2,5/2}) \rightarrow Xe^{2+}(4d^{10}5s^{2}5p^{4} \, SLJ) + e^{-} \quad (10)$$

$$\rightarrow Xe^{2+}(4d^{10}5s5p^{5} \, ^{1,3}P_{J}) + e^{-} \quad (11)$$

$$\rightarrow Xe^{2+}(4d^{10}5s^{0}5p^{6} \, ^{1}S_{0}) + e^{-} \quad . \quad (12)$$
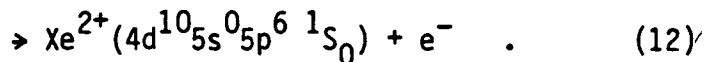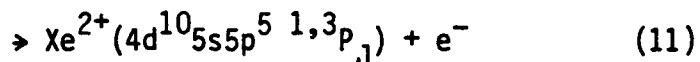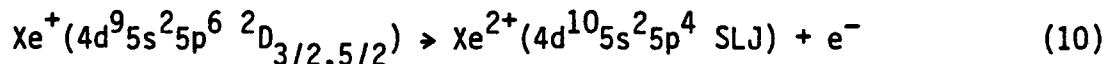
The kinetic energy of an Auger electron is equal to the energy difference between the inner-vacancy state and the doubly-charged final state:

$$\epsilon = E^+ - E^{2+} \quad . \tag{13}$$

Thus, a series of Auger lines are produced, corresponding to transitions to various Xe^{2+} final states. Actually, a double series of Auger lines appears, due to decay from each of the fine-structure levels of the 4d vacancy. In accordance with Eq. (13), the corresponding lines in the two series (produced by transition to the same Xe^{2+} final state) are shifted in energy by 1.97 eV, the spin-orbit splitting of the Xe^+ $^2D_{5/2}$ and $^2D_{3/2}$ levels.

Flügge et al.[25] showed that photoionization of an atomic subshell with $j > 1/2$ produces an aligned ionic state if its total angular momentum $J > 1/2$. "Alignment" means that the magnetic sublevels JM are unequally populated, and as a result, the Auger electrons should exhibit anisotropic angular distributions. Berezhko et al.[26] have calculated a strong, energy-dependent alignment of the Xe^+ $^2D_{5/2}$ and $^2D_{3/2}$ ions following photoionization of the 4d subshell. To our knowledge, no experimental observation of this effect had been made previous to the present measurements (given in Chapter III), although Auger anisotropies had been measured following inner-shell ionization by electron impact.[27]

A very general formulation of angular correlations in scattering processes is obtained using the density matrix[28] and its statistical tensors.[29] This formulation is particularly advantageous for the description of successive radiations (in the present case, Auger emission following photoemission), or other effects, such as the

spin-polarization of photoelectrons, which depend on the angular symmetry properties of the system. The statistical tensors formalism has been used to derive expressions for the angular distributions of photoelectrons[13,14] and of Auger electrons following photoionization.[26] Here I present some of the basic concepts used in the analysis of Auger electron angular distributions. As background reading for understanding these topics in angular momentum theory, I found the review works by Ferguson[30] and by Blum and Kleinpoppen[31] and the book by Brink and Satchler helpful.[32]

The density matrix is useful for describing the properties of a "mixed state" of a system consisting of a large number of identical, non-interacting atoms (or molecules, photons, etc.). The relevant example in the present case is an ensemble of particles with definite total angular momentum J, but consisting of a distribution over magnetic substates $M = -J, -J + 1,..., J$. The eigenstate $|i)$ of the i<u>th</u> particle can be expressed as a linear combination in the JM basis:

$$|i) = \sum_M a_M(i)|JM).$$

(14)

The elements of the density matrix ρ for the ensemble of particles can be defined as (neglecting normalization):

$$(JM'|\rho|JM) = \sum_i a_{M'}(i)a_M(i)^*\,.$$

(15)

The properties of the ensemble of particles are averages over the components, and the density matrix contains this averaging effect. For describing the angular symmetry properties of the system, however, it is convenient to define the statistical tensors or "state multipoles" T_{KQ}. The T_{KQ} ($Q = -K, -K+1, \ldots, K$) are linear combinations of the density matrix elements which transform under coordinate rotations like the spherical harmonics Y_{KQ}. They are defined by the expression

$$T_{KQ}(J) = \sum_{M'M} (-1)^{J-M}(JM'J-M|KQ)(JM'|\rho|JM) , \tag{16}$$

where $(JM'J-M|KQ)$ is a Clebsch-Gordon coefficient.

Consider the process of atomic (or molecular) photoionization of a gas-phase sample. Prior to interaction with the photon beam, the target atoms are randomly oriented, i.e., the atomic density matrix is spherically symmetric and only the monopole component T_{00} is nonzero. However, photon absorption by the electric-dipole interaction introduces statistical tensors of rank $K \leq 2$. With use of a linearly-polarized photon beam, the natural choice for a quantization axis is parallel to the photon polarization vector, because the photoexcited atomic system has axial symmetry about that direction. In addition, the photoexcited system is symmetric with respect to reversal of the quantization axis. As a result of axial symmetry, the density matrix is diagonal:

$$(JM'|\rho|JM) = (JM|\rho|JM)\delta_{M'M}. \tag{17}$$

Symmetry with respect to reversal of the quantization axis requires that

$$(J-M|\rho|J-M) = (JM|\rho|JM) \quad . \tag{18}$$

With these symmetry properties, all of the statistical tensors vanish except $T_{00}(J)$ and $T_{20}(J)$. As a consequence, the angular distributions of photofragments take the form

$$I(\theta) \propto 1 + \beta P_2(\cos\theta) \quad , \tag{19}$$

where P_2 is the Legendre polynomial, θ is measured with respect to the quantization axis (photon polarization vector), and β is an "asymmetry parameter." This is the form of the angular distribution given in Eq. (7) for photoelectrons. The photoelectron asymmetry parameter β is determined by the dipole transition amplitudes, including interference terms, for the photoionization process. Here we want to analyze the Auger electron angular distribution, which is determined by two processes: photoionization followed by decay of the inner-shell vacancy.

Consider, in particular, photoionization of a $4d_{5/2}$ electron from Xe to produce an ensemble of $Xe^+ \; {}^2D_{5/2}$ ions (Eq. (9)). Since axial symmetry results in a diagonal density matrix (Eq. (17)), the ${}^2D_{5/2}$ ensemble has the properties, statistically, of an incoherent

superposition of magnetic substates JM (J = 5/2; M = ±5/2, ±3/2, ±1/2). The relative populations of the magnetic sublevels are proportional to the partial photoionization cross sections $\sigma(JM)$, and we equate these with the density matrix elements:

$$(JM|\rho|JM) = \sigma(JM). \tag{20}$$

With this identification, the trace of the density matrix is equal to the photoionization cross section summed over the magnetic substates:

$$\text{tr}\rho = \sum_{M} \sigma(JM) = \sigma(J) . \tag{21}$$

Eq. (21) specifies the normalization of the density matrix. Symmetry with respect to reversal of the quantization axis (Eq. (18)) implies that the sublevels M and -M are equally populated:

$$\sigma(J-M) = \sigma(JM) . \tag{22}$$

Explicit expressions can be given for the two nonzero tensor components $T_{00}(J)$ and $T_{20}(J)$ by use of formulae for the Clebsch-Gordon coefficients:[32]

$$T_{00}(J) = \frac{1}{(2J+1)^{1/2}} \sum_{M} \sigma(JM) = \frac{\sigma(J)}{(2J+1)^{1/2}} \tag{23}$$

$$T_{20}(J) = \left[\frac{5}{J(J+1)(2J+3)(2J+1)(2J-1)}\right]^{1/2} \sum_{M} [3M^2 - J(J+1)]\sigma(JM). \tag{24}$$

For the case of Xe^+ $^2D_{5/2}$ the tensor components are

$$T_{00}(5/2) = \frac{2}{\sqrt{6}} \left[\sigma(\tfrac{5}{2}\tfrac{5}{2}) + \sigma(\tfrac{5}{2}\tfrac{3}{2}) + \sigma(\tfrac{5}{2}\tfrac{1}{2}) \right] \qquad (25)$$

$$T_{20}(5/2) = \frac{1}{\sqrt{21}} \left[5\sigma(\tfrac{5}{2}\tfrac{5}{2}) - \sigma(\tfrac{5}{2}\tfrac{3}{2}) - 4\sigma(\tfrac{5}{2}\tfrac{1}{2}) \right], \qquad (26)$$

where the symmetry property of Eq. (22) has been used. The monopole term $T_{00}(J)$ is essentially a normalization factor. The "alignment" component $T_{20}(J)$ contains the angular information about the system which is needed for describing the angular distributions of Auger electrons. Note that $T_{20}(5/2)$ is nonzero if the partial cross sections $\sigma(JM)$ are different for the different magnetic sublevels. The system is then said to be aligned.

The angular symmetry properties of an aligned axially symmetric ensemble of Xe^+ $^2D_{5/2}$ ions are illustrated in Fig. 1 (adopted from Ref. 31). The arrows are labeled by the values M of the magnetic sublevels and are directed in the corresponding directions with respect to the quantization (Z) axis. The lengths of the arrows are proportional to the partial photoionization cross sections $\sigma(JM)$ for the magnetic substates. Equivalent arrows are drawn to the left and right of the Z axis to illustrate the axial symmetry. Arrows of the same length are drawn for sublevels M and -M to represent the reflection symmetry.

For describing the anisotropy of Auger electrons it is useful to define the "alignment tensor"

$$A_{20}(J) \equiv T_{20}(J)/T_{00}(J) \quad . \tag{27}$$

Then for $Xe^+\ ^2D_{5/2}$ the alignment can be expressed as

$$A_{20}(5/2) = \frac{1}{\sqrt{14}} \left[\frac{5\sigma(\frac{5}{2}\ \frac{5}{2}) - \sigma(\frac{5}{2}\ \frac{3}{2}) - 4\sigma(\frac{5}{2}\ \frac{1}{2})}{\sigma(\frac{5}{2}\ \frac{5}{2}) + \sigma(\frac{5}{2}\ \frac{3}{2}) + \sigma(\frac{5}{2}\ \frac{1}{2})} \right] . \tag{28}$$

Photoejection of a $4d_{3/2}$ electron produces $Xe^+\ ^2D_{3/2}$, and the corresponding alignment tensor is

$$A_{20}(3/2) = \frac{\sigma(\frac{3}{2}\ \frac{3}{2}) - \sigma(\frac{3}{2}\ \frac{1}{2})}{\sigma(\frac{3}{2}\ \frac{3}{2}) + \sigma(\frac{3}{2}\ \frac{1}{2})} \quad . \tag{29}$$

Since Auger electrons are a type of "photofragment," their angular distributions take the form expressed in Eq. (19). The asymmetry parameter β for a particular Auger transition is proportional to the alignment tensor:[26]

$$\beta(h\nu) = \alpha A_{20}(h\nu) \quad , \tag{30}$$

where α depends on transition matrix elements of the Coulomb operator and on the phases of the partial waves which describe the ejected Auger electron. The simple form of Eq. (30) demonstrates the utility of the statistical tensor formalism. The alignment tensor A_{20} contains the angular symmetry properties established in the atomic system by the photoionization process. The parameter α contains the dependence of the angular distribution on the Auger decay process. In the two-step model, the Auger emission process is independent of the photoionization process. As indicated in Eq. (30), the energy

dependence of the Auger asymmetry is determined only by the photon energy dependence of the alignment tensor. For a given Auger transition, the Coulomb matrix elements and continuum wave phases are fixed, so α is independent of photon energy. However, the two-step model breaks down at photon energies very near the photoionization threshold, due to the so-called "post-collision interaction" (PCI) among the ion, Auger electron, and the slowly moving photoelectron.[33] In the near threshold region, the photoionization and Auger decay are more properly treated as a single process.[34-36] To my knowledge, it has not yet been theoretically investigated whether or not PCI would significantly modify the Auger electron angular distributions.

In a nonrelativistic model, the photoionization of an atomic subshell with orbital angular momentum $\ell \geq 1$ is characterized by two dipole-allowed channels: $n\ell \rightarrow \epsilon\ell-1$ and $n\ell \rightarrow \epsilon\ell+1$. Theoretical expressions for the alignment tensor show that $A_{20}(h\nu)$ is determined by the ratio of the partial photoionization cross sections $\sigma(\epsilon\ell-1)$ and $\sigma(\epsilon\ell+1)$ for the two partial waves.[25,26] Berezhko et al.[26] have calculated $A_{20}(h\nu)$ curves which vary significantly among different atoms and subshells. A strong energy dependence of A_{20} may occur near the ionization threshold, where $\sigma(\epsilon\ell+1)$ can be small due to the centrifugal barrier,[37] and again near the Cooper minimum,[38] where the $n\ell \rightarrow \epsilon\ell+1$ matrix element passes through a zero. Thus, Eq. (30) shows that the Auger electron angular distribution is sensitive to the atomic subshell structure and the photoionization dynamics.

The Auger angular distribution is also dependent on the Coulomb decay process through the factor α in Eq. (30). $A_{20}(h\nu)$ is a property of a given inner-shell vacancy, for example, $Xe^{+}\ ^{2}D_{5/2}$ in Eq. (9). However the factor α is determined by the Auger process and varies among the final states (Eqs. (10) - (12)). The asymmetry parameters of all of the Auger lines produced from the same inner-shell vacancy should display the same energy dependence, but differ in magnitude by constant scale factors. For the case of a doubly-ionized final state having total angular momentum $J_f = 0$, there is a single continuum wave, and Cleff and Mehlhorn[39] have shown that the Auger angular distribution is then independent of the Coulomb matrix element and the phase shift. The factor α in Eq. (30) is then given by angular momentum coupling coefficients[40] (see Ref. 41).

Consider again the two photoionization processes described in Eq. (9), i.e., formation of $Xe^{+}\ ^{2}D_{5/2}$ and $^{2}D_{3/2}$. These processes are characterized by the alignment tensors $A_{20}(5/2)$ and $A_{20}(3/2)$ (Eqs. (28) and (29)). And consider the case that the final states of the Auger process are $^{1}S_{0}$ levels:

$$Xe^{+}(4d^{9}5s^{2}5p^{6}\ ^{2}D_{J}) \rightarrow Xe^{2+}(^{1}S_{0}) + e^{-}(\epsilon d_{J}), \quad J = \tfrac{5}{2}, \tfrac{3}{2} \quad . \qquad (31)$$
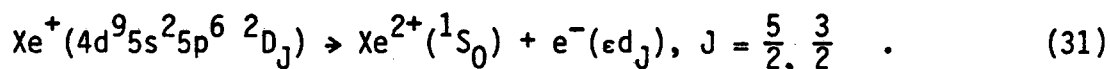
In both cases there is a single partial wave with angular momenta fixed by the selection rules[39] for Coulomb matrix elements. The decay factors α of Eq. (30) are calculated[40,41] to give the following expressions for the Auger asymmetry parameters:

$$\beta(^2D_{5/2} \rightarrow {}^1S_0) = 4\sqrt{\frac{2}{7}} A_{20}(5/2) \tag{32}$$

$$\beta(^2D_{3/2} \rightarrow {}^1S_0) = 2A_{20}(3/2) \quad . \tag{33}$$

So measurement of the asymmetry parameters for these Auger transitions provides a direct determination of the alignment tensors. Additional discussion of the theoretical analysis of Auger electron angular distributions will be given in Chapter III along with the experimental results.

References

1. S. T. Manson and D. Dill, in Electron Spectroscopy: Theory, Techniques, and Applications, Vol. 2, edited by C. R. Brundle and A. D. Baker (Academic, New York, 1978), p. 157.

2. A. F. Starace, Appl. Opt. 19, 4051 (1980).

3. M. O. Krause, in Synchrotron Radiation Research, edited by S. Doniach and H. Winick (Plenum, New York, 1980).

4. F. J. Wuilleumier, Atom. Phys. 7, 491 (1981).

5. J. L. Dehmer and D. Dill, in Electron-Molecule and Photon-Molecule Collisions, edited by T. Rescigno, V. McKoy, and B. Schneider (Plenum, New York, 1979), p. 225.

6. P. W. Langhoff, in Ref. 5, p. 183.

7. R. R. Lucchese and V. McKoy, Phys. Rev. A 21, 112 (1980).

8. J. A. R. Samson, in Ref. 1, Vol. 4 (1981), p. 361.

9. J. B. West, Appl. Opt. 19, 4063 (1980); P. M. Guyon and I. Nenner, ibid. 19, 4068 (1980).

10. R. Stockbauer et al., Extended Abstracts of the VIth Intnl. Conf. VUV Rad. Phys. (1980), No. II-15; J. L. Dehmer et al., ibid., No. II-86.

11. J. W. Rabalais, Principles of Ultraviolet Photoelectron Spectroscopy (Wiley, New York, 1977).

12. C. N. Yang, Phys. Rev. 74, 764 (1948).

13. M. Peshkin, Adv. Chem. Phys. 18, 1 (1970).

14. V. L. Jacobs, J. Phys. B 5, 2257 (1972).

15. U. Fano and D. Dill, Phys. Rev. A $\underline{6}$, 185 (1972); D. Dill and
U. Fano, Phys. Rev. Lett. $\underline{29}$, 1203 (1972).

16. H. K. Tseng, R. H. Pratt, S. Yu, and A. Ron, Phys. Rev. A $\underline{17}$, 1061
(1978).

17. S. T. Manson, Adv. Electron. Electron Phys. $\underline{41}$, 73 (1976); ibid.
$\underline{44}$, 1 (1977).

18. For diatomic molecules: J. C. Tully, R. S. Berry, and
B. J. Dalton, Phys. Rev. $\underline{176}$, 95 (1968); A. D. Buckingham, B.
J. Orr, and J. M. Sichel, Phil. Trans. Roy. Soc. Lond. A $\underline{268}$, 147
(1970).

19. D. Dill, Phys. Rev. A $\underline{6}$, 160 (1972).

20. J. L. Dehmer and D. Dill, Phys. Rev. Lett. $\underline{37}$, 1049 (1976).

21. E. H. S. Burhop and W. N. Asaad, Adv. Atom. Molec. Phys. $\underline{8}$, 163
(1972).

22. E. J. McGuire, in Atomic Inner-Shell Processes, Vol. I, edited by
B. Crasemann (Academic, New York, 1975), p. 293.

23. T. A. Carlson, Photoelectron and Auger Spectroscopy (Plenum, New
York, 1975).

24. D. Chattarji, The Theory of Auger Transitions (Academic, New York,
1976).

25. S. Flügge, W. Mehlhorn, and V. Schmidt, Phys. Rev. Lett. $\underline{29}$, 7
(1972).

26. E. G. Berezhko, N. M. Kabachnik, and V. S. Rostovsky, J. Phys. B
$\underline{11}$, 1749 (1978).

27. B. Cleff and W. Mehlhorn, Phys. Lett. 37A, 3 (1971); J. Phys. B 7, 605 (1974).

28. U. Fano, Rev. Mod. Phys. 29, 74 (1957).

29. U. Fano, Phys. Rev. 90, 577 (1953).

30. A. J. Ferguson, Angular Correlation Methods in Gamma-Ray Spectroscopy (Wiley, New York, 1965).

31. K. Blum and H. Kleinpoppen, Phys. Reports 52, 203 (1979).

32. D. M. Brink and G. R. Satchler, Angular Momentum (Oxford, London, 1968).

33. V. Schmidt, S. Krummacher, F. Wuilleumier, and P. Dhez, Phys. Rev. A 24, 1803 (1981), and references therein.

34. G. Wendin, in Photoionization of Atoms and Molecules, edited by B. D. Buckley (Daresbury Laboratory report DL/SCI/R11, 1978), p. 1.

35. T. Åberg, Phys. Scr. 21, 495 (1980).

36. M. Ya. Amusia, Appl. Opt. 19, 4042 (1980).

37. S. T. Manson and J. W. Cooper, Phys. Rev. 165, 126 (1968).

38. J. W. Cooper, Phys. Rev. 128, 681 (1962).

39. B. Cleff and W. Mehlhorn, J. Phys. B 7, 593 (1974).

40. E. G. Berezhko and N. M. Kabachnik, J. Phys. B 10, 2467 (1977).

41. The expressions for α given in Ref. 40 are for the case where angles are measured with respect to the propagation direction of the photon beam rather than the polarization direction. To make the factor α in Eq. (30) consistent with the general definition of an asymmetry parameter β (Eq. (19)), it is necessary to multiply the α values of Ref. 40 by -2.

Figure Caption

Fig. 1. Diagram illustrating the angular symmetry properties of an aligned axially symmetric ensemble of Xe^+ $^2D_{5/2}$ ions. Explanation is given in the text.
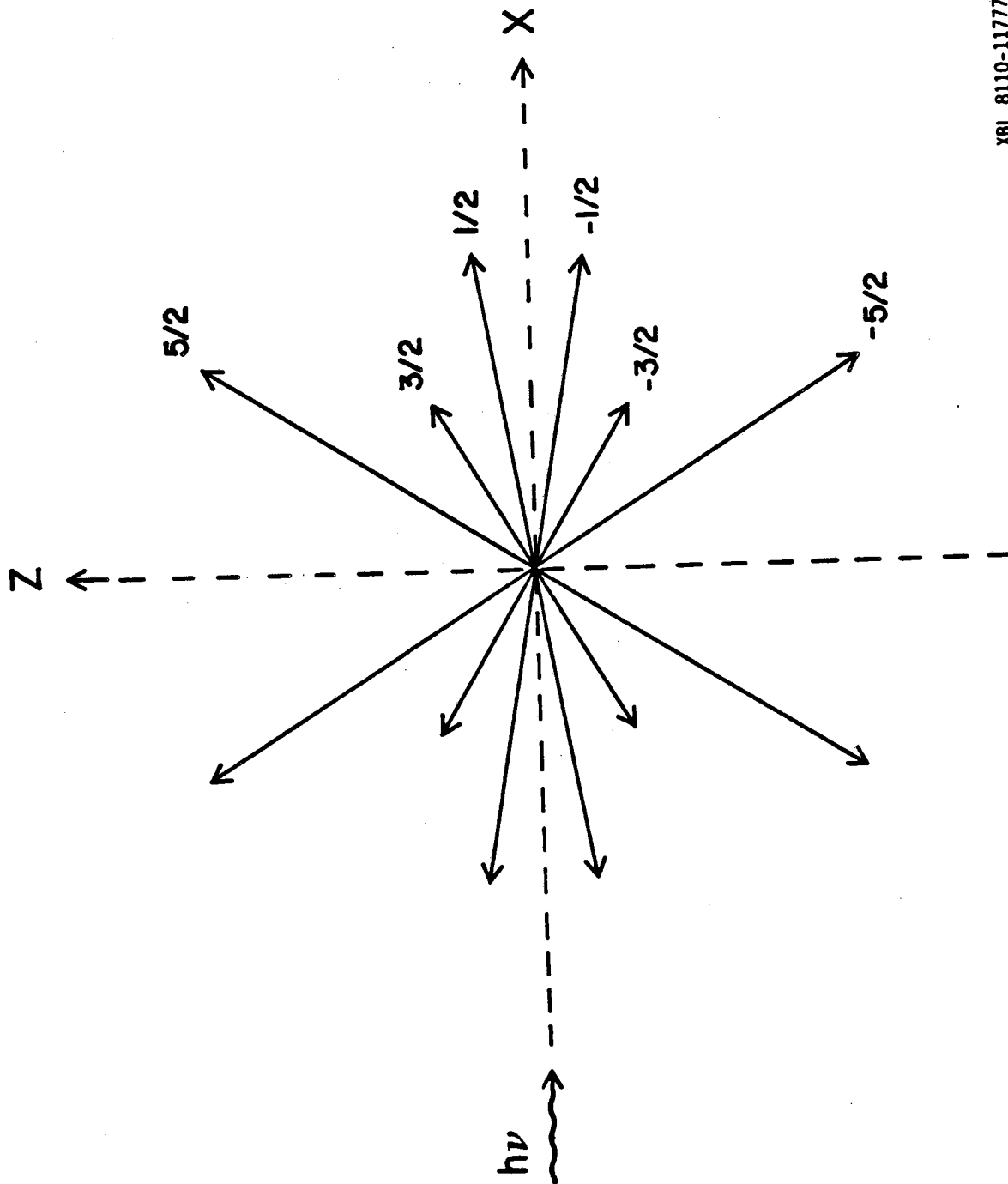
Figure 1

XBL 8110-11777

II. EXPERIMENT

A. Introduction

This thesis describes work done as part of a research program in atomic and molecular photoelectron spectroscopy which was established at the Stanford Synchrotron Radiation Laboratory (SSRL) in 1978. Additional information on this research project, particularly the instrumental aspects, is given in the Ph. D. theses of M. G. White and R. A. Rosenberg and in a publication.[1-3] Here I will describe the major instrumental aspects and discuss in some detail the "double-angle-time-of-flight" method for the measurement of photoelectron and Auger electron angular distributions.

B. Properties of the Synchrotron Radiation Source

A general description of the properties of synchrotron radiation and the instrumentation used in establishing research facilities has been given by Winick.[4] The properties of primary importance in the present experiments are the following:

1. The storage ring emits a smoothly varying continuum of photon energies throughout the vacuum-ultraviolet (VUV) and into the x-ray region. The effective energy range of a particular "beam line" is determined by the angles of deflection of the photon beam from the optical surfaces and by the type of monochromator used. Two beam lines at SSRL were used for the experiments described here. The VUV beam line[5] (8° line) uses a 1 m Seya-Namioka monochromator and has an effective energy range of $h\nu \approx 4{-}36$ eV. With a 1200 ℓ/mm grating

and 2.5Å FWHM bandpass, a flux of about 10^9-10^{10} photons $sec^{-1}cm^{-2}$ is provided with 10 mA electron current in the storage ring.

A grazing incidence "grasshopper" monochromator[6] is used on the soft X-ray beam line (new 4° line) and provides photon energies over the range $h\nu \simeq$ 20-1000 eV. Both 300 ℓ/mm and 600 ℓ/mm gratings were used, and the entrance and exit slits of the monochromator were adjusted to provide a variable bandpass $\Delta\lambda \simeq$ 1-5Å FWHM. Depending on the bandpass used, an estimated photon flux of 10^8-10^{10} $sec^{-1}cm^{-2}$ was obtained.

2. The radiation emitted from the storage ring is highly (~75 percent) linearly polarized. Reflections from the optical surfaces of the VUV beam line enhance the degree of linear polarization. Rehn et al.[5] estimate a lower limit of 97 percent polarization for the monochromatized photon beam. We estimate a similar high degree of linear polarization for the soft X-ray beam line over the energy range of the experiments ($h\nu <$ 350 eV). This result is based on the very high asymmetry (β = 1.94) measured for Ag 4s $\rightarrow \epsilon p$ photoelectrons with a rotatable analyzer.[7] The limiting value for this transition is β = 2. If the observed $\beta <$ 2 results from incomplete polarization of the photon beam, a value of 98 percent linear polarization is indicated.

A high degree of linear polarization is desirable for the measurement of the angular distributions of photoelectrons and Auger electrons. For a linearly polarized photon beam producing electric dipole

excitation of a randomly oriented target, the differential cross section has the form[8]

$$\frac{d\sigma(\theta)}{d\Omega} = \frac{\sigma}{4\pi} [1 + \beta P_2(\cos\theta)] \quad , \tag{1}$$

where β is the asymmetry parameter and θ is the angle between the photoelectron propagation direction and the photon polarization vector. A similar expression applies in the case of unpolarized light, but here[8]

$$\frac{d\sigma(\theta')}{d\Omega} = \frac{\sigma}{4\pi} [1 - (\beta/2) P_2(\cos\theta')] \quad , \tag{2}$$

where θ' is the angle between the propagation directions of the photoelectron and the photon beam. Comparison of Eqs. (1) and (2) shows that the differential cross section is less sensitive to angular variations when unpolarized light is used. The maximum anisotropy is produced using 100 percent linearly polarized light. This greater sensitivity is helpful in measuring the asymmetry parameter.

3. The beam line collects a pulse of radiation for each cycle of an electron bunch in the storage ring. Hence, the photon beam has a characteristic time structure. With a single electron bunch in the storage ring at SSRL, the photon beam has a time structure of 0.3 ns pulse width and 780 ns repetition period. This pulse structure of synchrotron radiation has been used for time-resolved fluorescence studies on the ns time scale.[9,10] In the present experiments the

time structure is used to record time-of-flight spectra of photoelec-
trons and Auger electrons.

4. There are certain disadvantages in the use of synchrotron rad-
iation which should be mentioned here. Some of these are particular
to SSRL, where the storage ring was constructed for high-energy phys-
ics experiments. The synchrotron radiation spectroscopist desires
that the storage ring be operated with maximum current and stability,
since the photon beam intensity is proportional to the electron cur-
rent. High current and stability are attained when the ring is oper-
ated by the SSRL staff under "dedicated" running. However the present
measurements were made under the "parasitic" mode, where the storage
ring is operated with colliding electron and positron beams at a cur-
rent and energy required for the high energy physics experiment. As a
result, the beam currents were relatively low (10-25 mA), and the ring
had to be re-injected more frequently than under dedicated running.
The synchrotron ring and the two mile linear accelerator (LINAC) used
to inject electrons and positrons into the ring are large, complex ma-
chines. Equipment failures are frequent, resulting in a loss of about
50 percent of the beam time.

There are strict requirements at SSRL to maintain ultrahigh vacuum
and prevent contamination in the storage ring and beam lines. For
gas-phase experiments, a window must be placed between the monochrom-
ator and experimental chamber. The transmission of the window further
limits the useful photon energy range of a beam line.

The great demand for beam time at SSRL limits the running time on a particular beam line to about a two week period. All of the equipment involved, LINAC, storage ring, beam line, and the electron spectrometer, must work during that time period in order to successfully complete an experiment. Considerable work is required to set up the electron spectrometer on a beam line, and time is required each time to "debug" equipment and to calibrate the instrument before new information is obtained on an atomic or molecular system.

I want to remember here the feeling of amazement I always experienced when everything actually worked! We then had that exciting opportunity in science to observe properties of atoms and molecules that had never been recorded.

C. The Electron Spectrometer

A diagram of the electron spectrometer is shown in Fig. 1. The sample gas is released from a probe at the center of the main chamber, where it is intersected by the photon beam. A gas density of about 10^{13} cm^{-3} is established in the interaction region, while turbomolecular pumps maintain the chamber pressure in the range 10^{-4}-10^{-5} torr. A sodium salicylate scintillator and photomultiplier tube positioned at the rear of the chamber are used to monitor the photon beam intensity. An ultrathin (~1500Å) Al window separates the main chamber from the ultrahigh vacuum (10^{-9}-10^{-10} torr) of the monochromator and beam line. An ion pump collects the small gas load which seeps through the window. The front gate valve is interlocked to isolate the monochromator and beam line in case of vacuum failure in the main chamber.

The polarization vector of the photon beam is normal to the plane of Fig. 1. The photoelectron detector is shown in a position to accept electrons ejected at 54.7° (the "magic angle") with respect to the polarization vector. Not shown in Fig. 1 is a second detector positioned parallel to the polarization vector to accept electrons ejected at 0°. Figure 2 shows a diagram of the double-detector geometry. The photoelectrons traverse a ~28 cm flight path before striking a microchannel plate detector (see Fig. 1). Electrons enter the drift tube through a 2.4 mm hole in the conical tip at a position ~2 cm from the interaction region. An acceptance angle of ±3° is defined by the diameter (2.8 cm) of the microchannel plate detector. The drift tube serves both as an electrostatic shield and to isolate the detector from the main chamber for differential pumping. Cylinders of mu-metal provide magnetic shielding of the interaction region and detectors. Additional details on the instrumental components, particularly the time-of-flight detector, are given in Refs. 1-3.

D. Time-of-Flight Photoelectron Analysis

Photoelectron spectra are usually recorded by use of an electrostatic deflection-type analyzer.[11] The photoelectrons are dispersed by deflective fields so that only electrons over a narrow kinetic energy range reach the detector and are recorded at a given time. A high resolution can thereby be attained, but to record a spectrum over a wide kinetic energy range requires that the analyzer be stepped by many small energy increments. This technique has a low collection efficiency, since most of the photoelectrons are discarded at any given time.

Beam time at SSRL is limited, and the photon beam is two orders of magnitude less intense than that from a typical He(I) line discharge lamp. So, in designing a spectrometer for angle-resolved photoelectron studies of gases at SSRL, it was realized that the collection efficiency of the analyzer was a critical factor.[1-3] The use of the time structure of the synchrotron radiation for time-of-flight (TOF) photoelectron kinetic energy analysis is a favorable alternative. This technique is illustrated schematically in Fig. 2. Every 780 ns, the period of the electron bunch in the storage ring, a pulse of light of ~0.3 ns width passes through the interaction region. For each pulse of light, an electronic "beam signal" pulse is sent to a fast-timing circuit. If a photoelectron is ejected from the interaction region at the appropriate angle to enter the TOF analyzer, an "electron signal" will be sent to the timing circuit when the photoelectron strikes the detector at the back of the analyzer. The time difference between the beam signal and electron signal is measured by the timing circuit. In this way we measure the times-of-flight of photoelectrons over the ~28 cm distance from the interaction region to the detector. For each detected photoelectron, the timing circuit records a count in the appropriate channel of a multichannel time scale. A TOF photo-electron spectrum is obtained, since slower photoelectrons require longer TOFs. For example, a 1 eV electron has a 470 ns TOF over 28 cm, and a 20 eV electron has a 110 ns TOF. The primary advantage of the TOF method is that photoelectrons of all kinetic energies are collected simultaneously, which greatly increases the collection efficiency in comparison with typical deflection-type analyzers.

Two TOF analyzers are operated simultaneously, at the positions shown in Fig. 2. The timing circuit used to record TOF spectra at two angles is shown schematically in Fig. 3. Photoelectron signals from the detectors are amplified, discriminated, and sent to a multi-input fan-in and a router. Signals from both detectors are sent to the same time-to-amplitude converter (TAC) via the fan-in. Separate quadrants of memory are established in the multichannel analyzer (MCA) for the two detectors. The router communicates with the TAC and MCA so that a photoelectron observed by a particular detector is recorded in the appropriate quadrant, and two separate TOF spectra are generated.

The observed count rates are on the order of 10^2 sec^{-1} or less. This is much less than the excitation frequency (1.28 MHz). Thus, there is negligible probability of producing more than one detectable photoelectron per photon pulse, so there is no discrimination against slower photoelectrons. Note that the electron signal is used to start the TAC and the beam signal stops it. This avoids a loss of counts due to the reset time of the TAC.

The energy resolution in a TOF spectrum is given by

$$\frac{\Delta \epsilon}{\epsilon} = \left[\left(\frac{2\Delta t}{t} \right)^2 + \left(\frac{2\Delta \ell}{\ell} \right)^2 + \left(\frac{\Delta \lambda}{\lambda} \right)^2 \right]^{1/2} \quad , \tag{3}$$

where t is the time-of-flight, ℓ is the path length, and λ is the photon wavelength. The uncertainty Δt arises from the width of the light pulse (~0.3 ns) and a smaller time spread (~0.1 ns) from the

microchannel plate detector and the electronic timing circuit. A small spread in path length ($\Delta \ell \approx 0.3$ mm) results from the $\pm 3°$ angular acceptance of the analyzer. A much larger contribution is due to variation of ℓ over the interaction region observed by each detector. In these experiments, the sample gas density was approximately uniform over the interaction region, and the effective interaction volume was determined by the size of the photon beam and the collection solid angles of the detectors. For both beam lines used in these experiments, the photon beam had a height and width of about 2 mm x 3 mm in the interaction region. At low photon energies, where $\Delta \lambda / \lambda$ was small, the variation of ℓ over the interaction volume gave the dominant contribution to $\Delta \epsilon$. This gave the 0° detector, which is perpendicular to the photon beam, a 2 percent energy resolution. The 54.7° detector is at an oblique position with respect to the photon beam, which gives a larger variation in path length; the energy resolution was 3-4 percent. At the smaller wavelengths used on the soft X-ray beam line, the $\Delta \lambda / \lambda$ term in Eq. (3) became significant.

The photoelectrons can be slowed down by simple retarding-grid units located inside the analyzer flight tubes. The retarding section extends over ~60 percent of the total flight path, the remainder being field-free. Retarding can be used to achieve the desired resolution in favorable cases, but there is a loss of signal which can become severe as the retarding voltage is increased.

E. Measurement of Angular Distributions and Partial Cross Sections

For any particular channel (final ionic state plus photoelectron), the photoionization process can be characterized by an energy-dependent cross section and a product angular distribution. As discussed in Chapter I, photoemission from randomly oriented target atoms (or molecules) by electric dipole interaction with a linearly polarized photon beam is described by a differential cross section of the form[8]

$$\frac{d\sigma(\theta,\epsilon)}{d\Omega} = \frac{\sigma(\epsilon)}{4\pi} [1 + \beta(\epsilon) \, P_2(\cos\theta)] \quad . \tag{4}$$

Here $\sigma(\epsilon)$ is the angle-integrated partial cross section, and $\beta(\epsilon)$ is the photoelectron asymmetry parameter.

The asymmetry parameter $\beta(\epsilon)$ is usually determined by measuring photoelectron intensities at several ejection angles and fitting the results to the form of Eq. (4) (for example, as in Ref. 12). From this equation, however, it is clear that $\beta(\epsilon)$ can be determined by measuring photoelectron intensities at only two angles. As shown schematically in Fig. 2 and described above, two TOF detectors are operated simultaneously. One detector is positioned to accept electrons ejected at $0°$ with respect to the polarization vector, for which $P_2(\cos\theta)$ is unity, and the other at $54.7°$, the "magic angle," where $P_2(\cos\theta)$ vanishes. In the TOF method, ejected electrons of all energies are recorded simultaneously, which greatly increases the collection efficiency and signal-to-noise ratio in comparison with single-channel electrostatic analyzers. More fundamentally, by

recording all of the photoelectron peaks simultaneously at both angles, we avoid the need to correct peak areas for variations in sample gas density or photon beam intensity, thereby reducing systematic error.

Because the two TOF detectors have different collection efficiencies and detect electrons from somewhat different portions of the interaction volume, it is necessary to calibrate the apparatus as a function of electron kinetic energy by recording photoelectron lines having known $\beta(\epsilon)$ values. For this purpose we record spectra of the rare gases at photon energies where accurate $\beta(\epsilon)$ values have been measured using resonance lines[13] or synchrotron radiation.[14] From Eq. (4), the differential cross sections observed by the two detectors are

$$\frac{d\sigma(0°,\epsilon)}{d\Omega} = \frac{\sigma(\epsilon)}{4\pi} [1 + \beta(\epsilon)] \tag{5}$$

$$\frac{d\sigma(54°,\epsilon)}{d\Omega} = \frac{\sigma(\epsilon)}{4\pi} . \tag{6}$$

Assuming, initially, the ideal conditions of a point source of photoelectrons, point detectors, 100 percent linearly polarized light, and perfect geometrical alignment of detectors and photon beam, the two detectors would record photoelectron signals $N(\theta,\epsilon)$ whose relative strengths depend only on the detector collection efficiencies $T(\theta,\epsilon)$ and differential cross sections:

$$N(\theta,\epsilon) \propto T(\theta,\epsilon)\frac{d\sigma(\theta,\epsilon)}{d\Omega} \ . \tag{7}$$

Calibration with a known $\beta(\epsilon)$ yields the relative collection efficiency $f_0(\epsilon)$ at a particular kinetic energy,

$$f_0(\epsilon) \equiv T(0^\circ,\epsilon)/T(54^\circ,\epsilon)$$

$$= \frac{N_c(0^\circ,\epsilon)/N_c(54^\circ,\epsilon)}{1 + \beta_c(\epsilon)} \ . \tag{8}$$

The subscript c in Eq. (8) represents the calibration photoelectron line. Unknown $\beta(\epsilon)$ values are then determined from the observed ratio of photoelectron intensities upon inversion of Eq. (8):

$$\beta_0(\epsilon) = -1 + \frac{N(0^\circ,\epsilon)/N(54^\circ,\epsilon)}{f_0(\epsilon)} \ . \tag{9}$$

Plotted in Fig. 4 is the calibration curve $f_0(\epsilon)$ determined in the experiments on the VUV beam line. Photoelectron lines of Ar, Kr, and Xe were used to obtain the calibration data points. The asymmetry parameter $\beta(\epsilon)$ for Ne 2p photoelectrons has been tabulated over a wide energy range.[14] The Ne 2p line was used to determine calibration curves for the soft X-ray beam line experiments. An example is plotted in Fig. 5 along with the Ne 2p $\beta(\epsilon)$ parameter curve. We found that the $f_0(\epsilon)$ function varies from run to run, and in the same run $f_0(\epsilon)$ can shift by about 20 percent with changes in the bandpass and/or the retarding voltage used in the TOF detectors. Therefore,

the $f_0(\epsilon)$ function was generally determined for each set of experimental conditions.

The subscript 0 is given to $f_0(\epsilon)$ and $\beta_0(\epsilon)$, because Eqs. (8) and (9) are zero–order expressions which neglect effects on the measured signal ratios due to having less than 100 percent linearly polarized light and to having a finite source region and finite collection solid angles. To account for these effects we have numerically computed the angular distribution produced by partially polarized light[15] and integrated over the solid angles of the detectors observing a photoelectron source region of finite volume.[16] This calculation requires knowledge of both the geometrical parameters of the spectrometer and the degree of linear polarization of the photon beam. The $\beta(\epsilon)$ values reported are those of Eq. (9) after correction for these effects. Table I shows the corrected β values that would be obtained from various uncorrected β_0 values for the typical case of a calibration value $\beta_c = 1.5$ and 97 percent linearly polarized light. The very small corrections needed indicate that the experimental system closely approaches the ideal case of point source, point detectors, and 100 percent polarization.

We estimate residual systematic error as ± 0.10 or less β unit due to uncertainty in the light polarization, geometrical parameters, and alignment of the detectors and photon beam. Deviations from the idealized experimental conditions are largely accounted for by being folded into the calibration function $f_0(\epsilon)$, Eq. (8). The magnitude of the β correction generally increases with increasing difference between

the β_c value used for calibration and the β value being determined.
In the limit that the unknown β value is identical to the calibration
β_c value, there is no correction to Eq. (9). This result is obtained
no matter how great the deviation of the actual experimental conditions
from the idealized experiment. This is illustrated in Table II where
deviations from the corrected β values of Table I are listed for a
large range of partially polarized photon beams. The deviations are
small except for β values in the range $\beta_0 = -0.5$ to -1.0, which are
far removed from the calibration value $\beta_c = 1.5$. Thus, if the polar-
ization were uncertain by 20-30 percent it would be necessary to use
calibration β_c values near to those being measured. The calibration
procedure also accounts for the loss of experimental photoelectron
asymmetry due to elastic scattering, an effect discussed by Kibel
et al.[12] Thus, even if such experimental systematic errors occur,
the observed asymmetries are scaled to the accurately known $\beta(\epsilon)$
values of the calibration lines.

As stated in Eqs. (6) and (7), the photoelectron signals observed
by the TOF detector at the magic angle are proportional to the angle-
integrated partial cross sections, independent of $\beta(\epsilon)$. Energy-depen-
dent, relative partial cross sections were determined by

$$\sigma(\epsilon) \propto \frac{N(54°,\epsilon)}{T(54°,\epsilon) \, n \, t \, I} \, , \tag{10}$$

where $N(54°,\epsilon)$ is the number of photoelectron counts recorded at the
magic angle detector, $T(54°,\epsilon)$ is the collection efficiency (relative

transmission) of the detector at electron energy ϵ, n is the sample gas density, t is the spectrum collection time, and I is the intensity of the photon beam. A sodium salicylate scintillator, optical phototube, and picoammeter were used to monitor the photon beam intensity.[17] For each gas, the sample density in the interaction region was assumed proportional to the pressure backing the gas inlet,[1-3] as measured by a capacitance manometer. The picoammeter and manometer signals were integrated over the collection time to account for variations. Collection times were typically 1000 sec. The magic angle detector transmission function was determined from photoelectron spectra of the rare gases, for which reliable cross sections have been tabulated.[14,18]

The partial cross sections of Eq. (10) were corrected slightly for the effects of incomplete linear polarization of the photon beam and angle-averaging over the finite source volume and detector solid angle. As for the β measurements, there is no correction to the measured cross section if the β value of the gas being measured is identical to the β value of the transmission calibration gas. In the present experiments the corrected partial cross sections differed by 3 percent or less from the values given by Eq. (10).

Note that since the normalization parameters n, t, and I in Eq. (10) are the same for all of the photoelectron peaks in a magic angle TOF spectrum, the branching ratios are equal to the peak areas after correction for detector transmission only.

On the VUV beam line, the transmission of the Al window and the high energy cut-off of the beam line optics limited the useful photon energy range to about 16-31 eV. Figure 6 shows a plot of the photon beam intensity of this beam line with use of an Al window. Figure 7 shows the relative photon beam intensity transmitted by the Al window on the soft X-ray beam line (using a 300 ℓ/mm grating). The light intensity drops sharply at the Al $L_{2,3}$-edge near 73 eV but rises again at higher energies. Sufficient intensity remained to record TOF spectra of Xe above the Al edge (see Chapter III).

Note that in Fig. 7 the Al edge structure is repeated at lower photon energy due to the second-order diffracted photon beam, which is thus seen to be strong at low energies. In certain energy regions, the third- and higher-order light intensities are significant. In Fig. 7, a large fraction of the light intensity at 400 eV is apparently due to scattered light. However, the scattered light component decreases at lower energies and appeared to be very small at photon energies $h\nu < 100$ eV where most of the spectra were recorded. As might be expected, the ratio of the intensities of the first- and higher-order beams was determined to vary rapidly at low energies and again above the Al $L_{2,3}$-edge. This result makes it difficult to measure partial photoionization cross sections, because the photoelectron peak areas must be normalized against the relative intensity of the first-order beam only. A careful calibration procedure apparently would be needed to determine the first-order beam intensity in order to measure partial

cross sections over a wide range of photon energies. This is not a problem, though, in the measurement of asymmetry parameters or branching ratios.

References

1. M. G. White, Ph. D. Thesis, University of California, Berkeley (1979); Lawrence Berkeley Laboratory report No. LBL-9527.

2. R. A. Rosenberg, Ph. D. Thesis, University of California, Berkeley (1979); Lawrence Berkeley Laboratory report No. LBL-8948.

3. M. G. White, R. A. Rosenberg, G. Gabor, E. D. Poliakoff, G. Thornton, S. H. Southworth, and D. A. Shirley, Rev. Sci. Instrum. 50, 1268 (1979).

4. H. Winick, in Synchrotron Radiation Research, H. Winick and S. Doniach, eds. (Plenum, New York, 1980).

5. V. Rehn, A. D. Baer, J. L. Stanford, D. S. Kyser, and V. O. Jones, in VUV Radiation Physics, E. Koch, R. Haensel, and C. Kunz, eds. (Pergamon-Vieweg, London/Braunsweig, 1974), p. 780.

6. F. C. Brown, R. Z. Bachrach, and N. Lien, Nucl. Instrum. Meth. 152, 73 (1978).

7. R. F. Davis, S. D. Kevan, B.-C. Lu, J. G. Tobin, and D. A. Shirley, Chem. Phys. Lett. 71, 448 (1980).

8. S. T. Manson and D. Dill, in Electron Spectroscopy: Theory, Techniques, and Applications, vol. 2, C. R. Brundle and A. D. Baker, eds. (Academic, New York, 1978), p. 157.

9. E. D. Poliakoff, Ph. D. Thesis, University of California, Berkeley (1979); Lawrence Berkeley Laboratory report No. LBL-9475.

10. I. H. Munro and A. P. Sabersky, in Ref. 4.

11. J. Berkowitz, Photoabsorption, Photoionization, and Photoelectron Spectroscopy (Academic, New York, 1979), p. 431.

12. M. H. Kibel, F. J. Leng, and G. L. Nyberg, J. Electron Spectrosc. 15, 281 (1979).

13. J. L. Dehmer, W. A. Chupka, J. Berkowitz, and W. T. Jivery, Phys. Rev. A 12, 1966 (1975); A. Niehaus and M. W. Ruf, Z. Phys. 252, 84 (1972); W. H. Hancock and J. A. R. Samson, J. Electron Spectrosc. 9, 211 (1976); J. Kreile and A. Schweig, J. Electron Spectrosc. 20, 191 (1980).

14. F. Wuilleumier and M. O. Krause, J. Electron Spectrosc. 15, 15 (1979).

15. J. A. R. Samson and A. F. Starace, J. Phys. B 8, 1806 (1975).

16. W. D. Brewer formulated this problem and wrote the computer program which solves it numerically.

17. J. A. R. Samson, Techniques of Vacuum Ultraviolet Spectroscopy (Wiley, New York, 1967).

18. G. V. Marr and J. B. West, At. Data Nucl. Data Tables 18, 497 (1976); J. B. West and J. Morton, ibid. 22, 103 (1978).

Table I. Corrected β values vs β_0 values given by Eq. (9).[a]

β_0	β (corrected)
2.00	1.97
1.50	1.50
1.00	1.02
0.50	0.53
0.00	0.03
−0.50	−0.49
−1.00	−1.02

[a]The corrections assume 97 percent linearly polarized light and a calibration $\beta_C = 1.50$.

Table II. Deviations of corrected β values from those of Table I
for a range of partially (%) linearly polarized photon beams.[a]

| β_0 | $\Delta\beta$ (corrected) | | | |
	100%	90%	80%	70%
2.00	0	−0.02	−0.04	−0.06
1.50	0	0	0	0
1.00	0	0.01	0.02	0.03
0.50	0	0.01	0.01	0.02
0.00	0	−0.01	−0.02	−0.03
−0.50	0.01	−0.03	−0.07	−0.12
−1.00	0.02	−0.06	−0.16	−0.27

[a]A calibration $\beta_C = 1.50$ is assumed.

Figure Captions

Fig. 1. Diagram of the electron spectrometer. A description is given in the text. PMT - photomultiplier tube; TMP - turbomolecular pump; MCP - microchannel plate detector.

Fig. 2. Diagram of the double-angle-TOF experiment. The time structure of the synchrotron radiation is used to record time-of-flight (TOF) photoelectron spectra. Two TOF detectors are operated simultaneously, one positioned at $0°$ and the other at $54.7°$ with respect to the polarization vector of the photon beam.

Fig. 3. Schematic diagram of the circuit used to record TOF spectra with two detectors. A description is given in the text. x9 amplifier; CFD - constant fraction discriminator; FI - multi-input fan-in; R - router; TAC - time-to-amplitude converter; PHA/MCA - pulse height analyzer/multichannel analyzer.

Fig. 4. Relative collection efficiency (Eq. (8)) of the two TOF detectors vs electron kinetic energy for the experiments on the VUV beam line. The line is a least-squares polynomial fit to the calibration data points.

Fig. 5. Calibration function $f_0(\epsilon)$ (Eq. (8)) for experiments on the soft X-ray beam line. Also shown is the asymmetry parameter $\beta(\epsilon)$ for Ne 2p photoelectrons, which was used to measure the calibration data points.

Fig. 6. Intensity of the photon beam which is transmitted through an
Al window on the VUV beam line (1200 ℓ/mm grating).

Fig. 7. Relative intensity of the photon beam of the soft X-ray beam
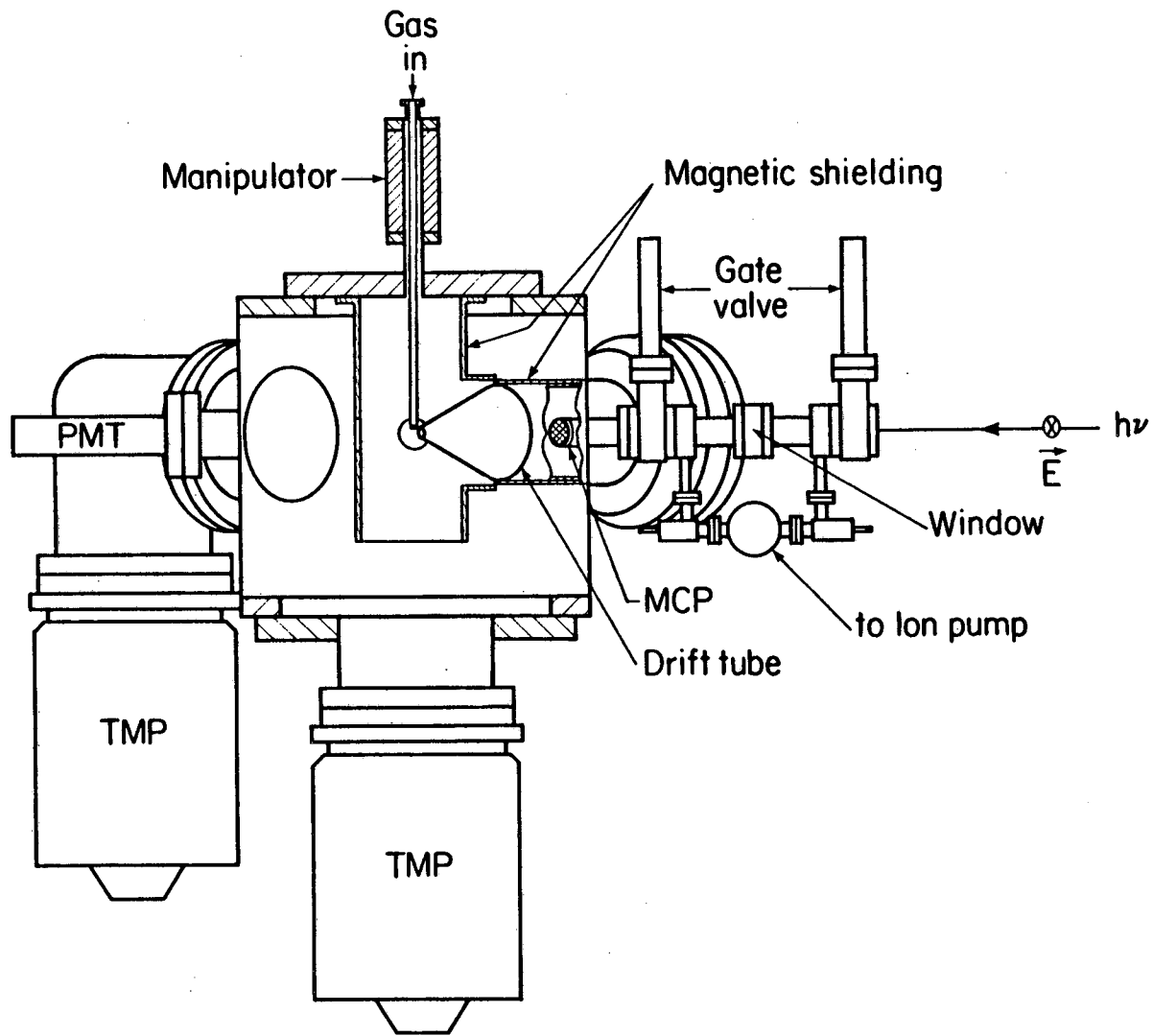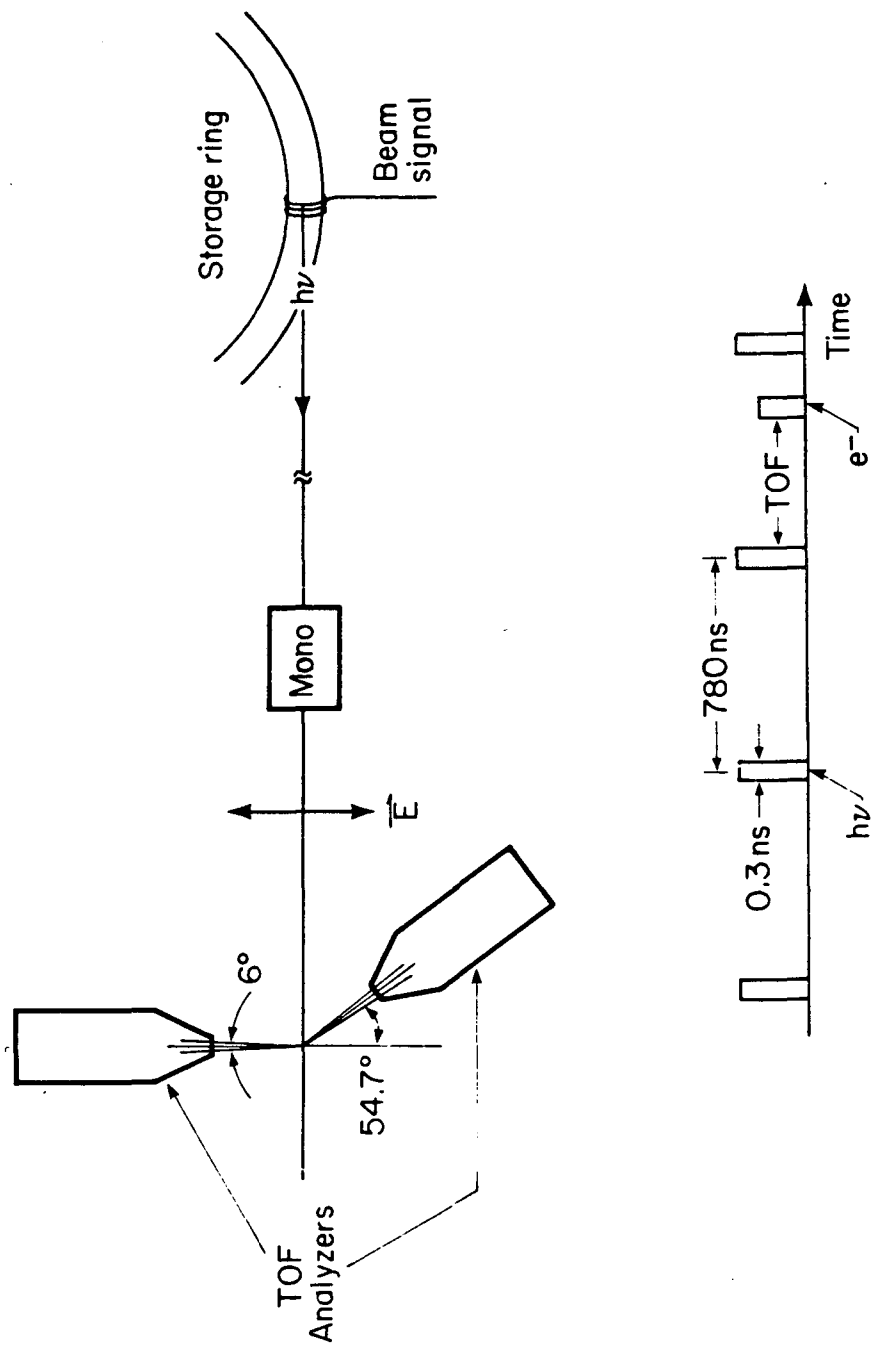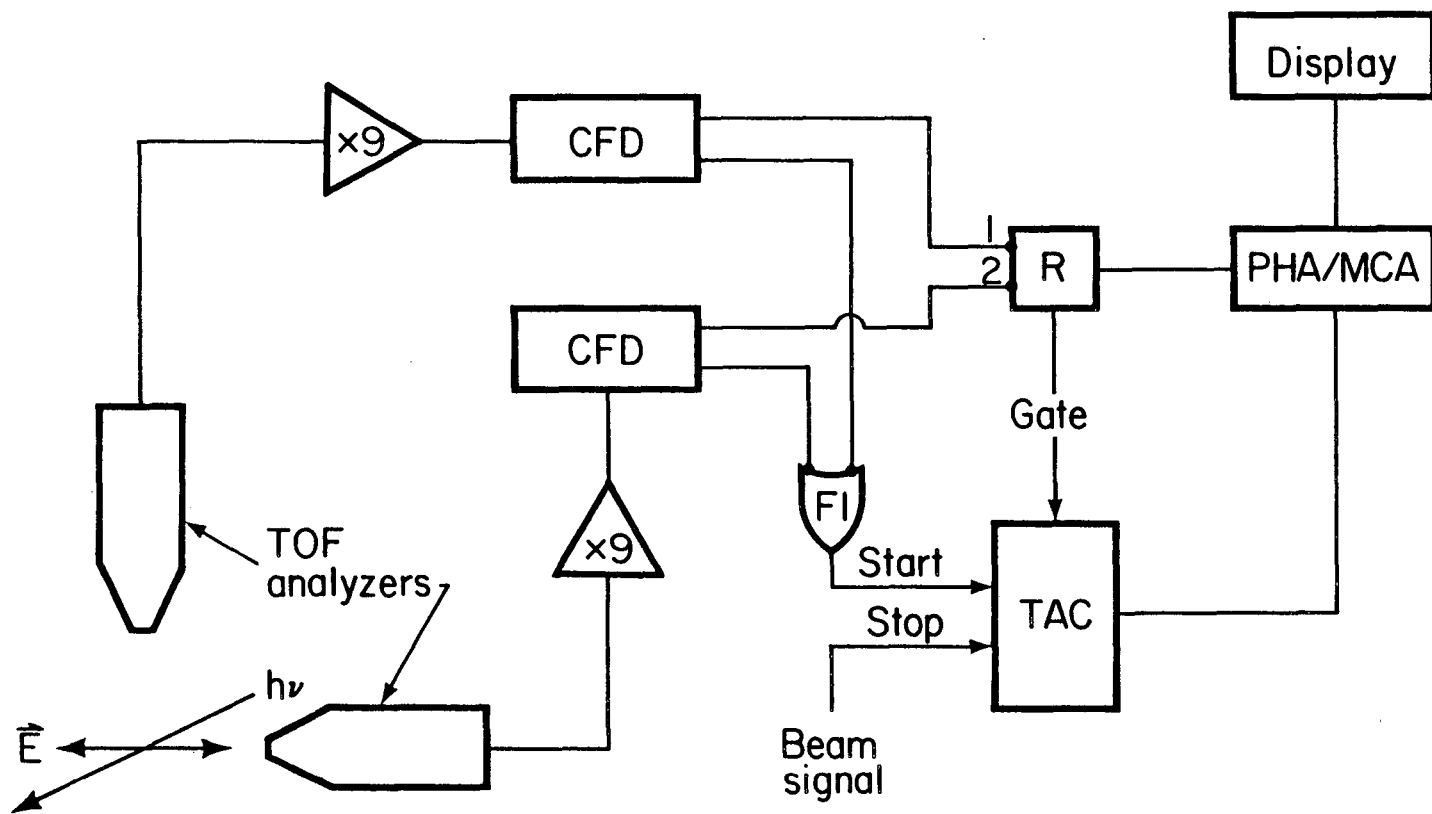line (300 ℓ/mm grating) when using an Al window.

Figure 1

Figure 2

XBL 7910-4225

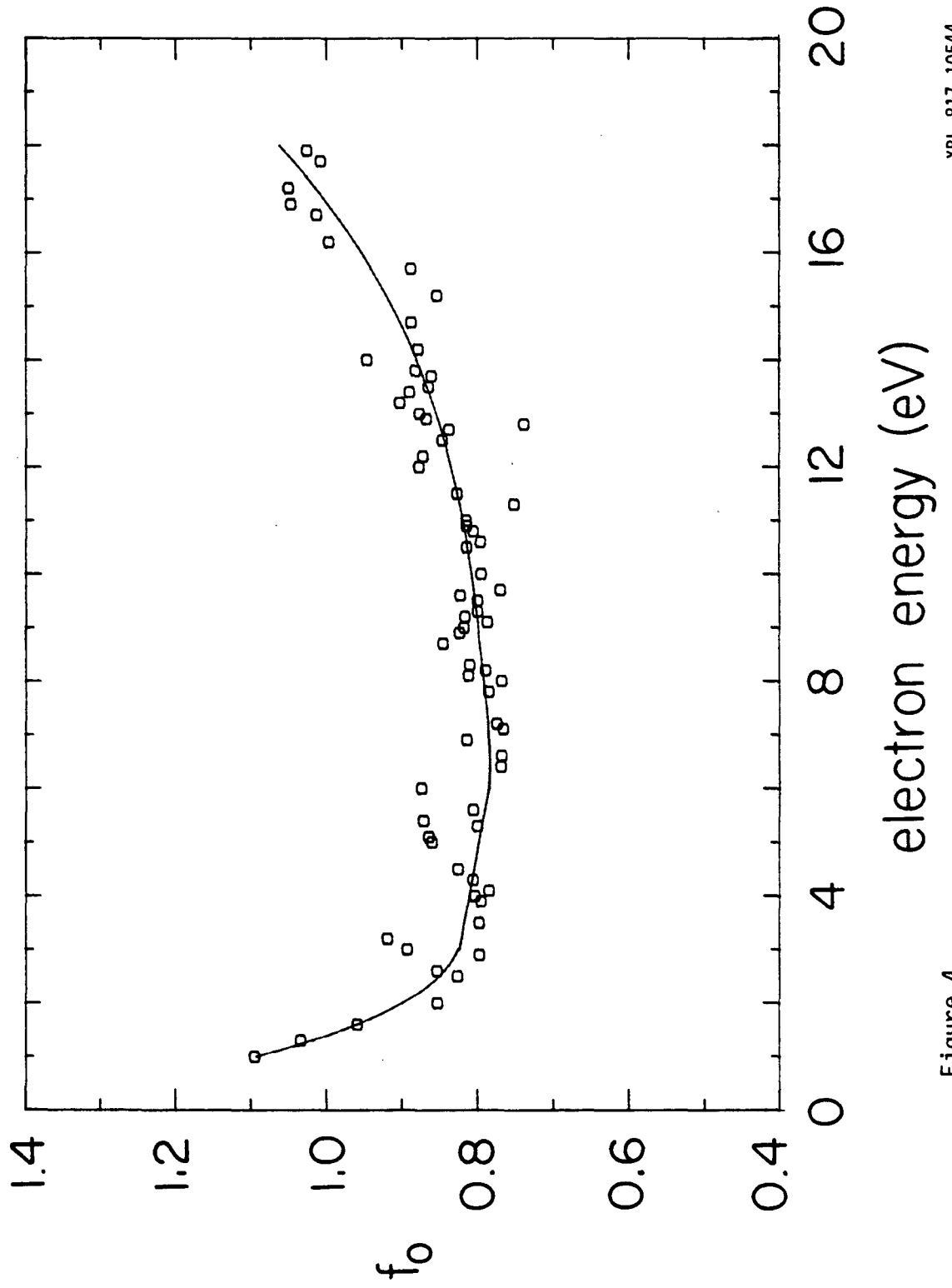XBL 792-618

Figure 3

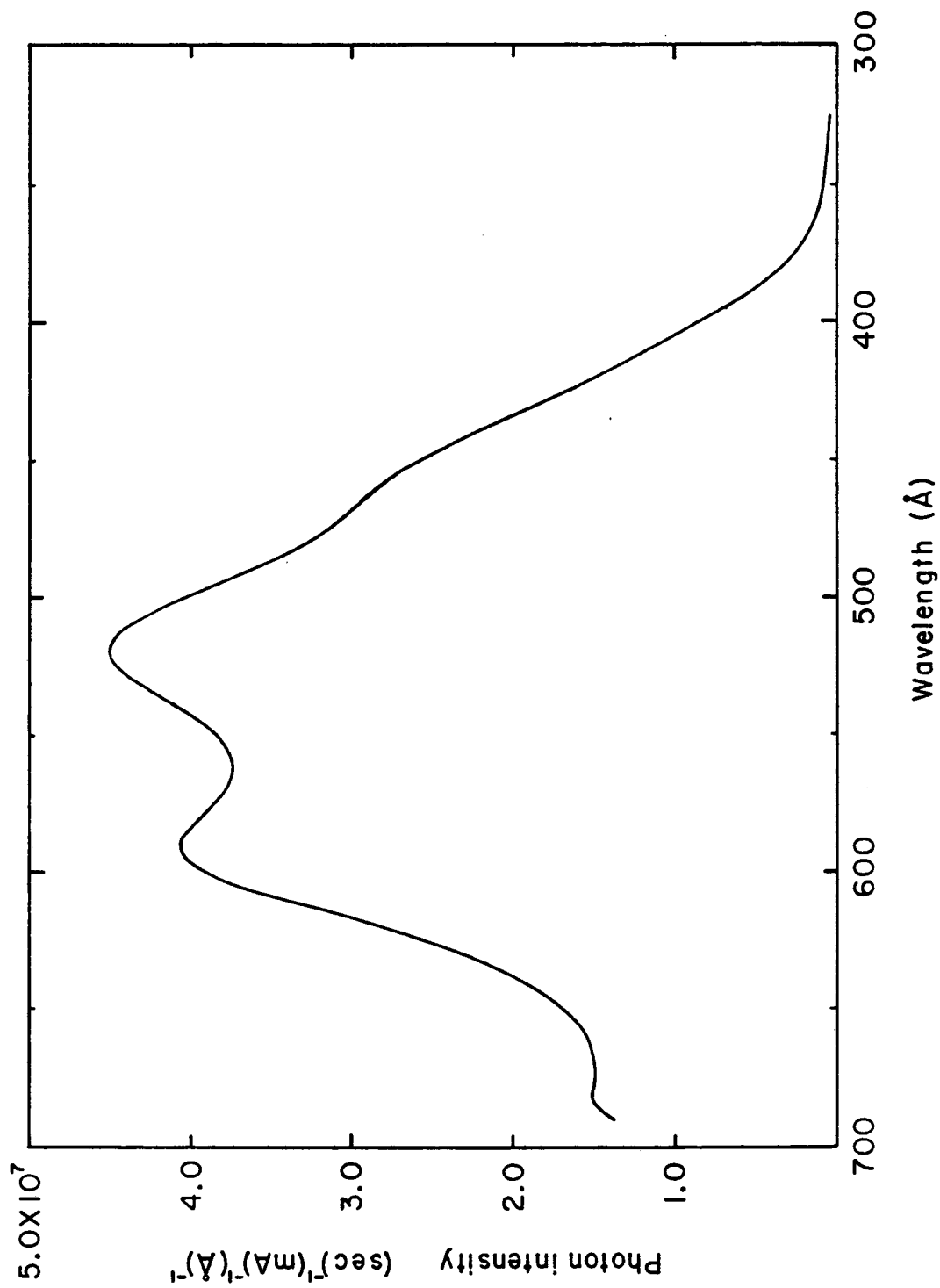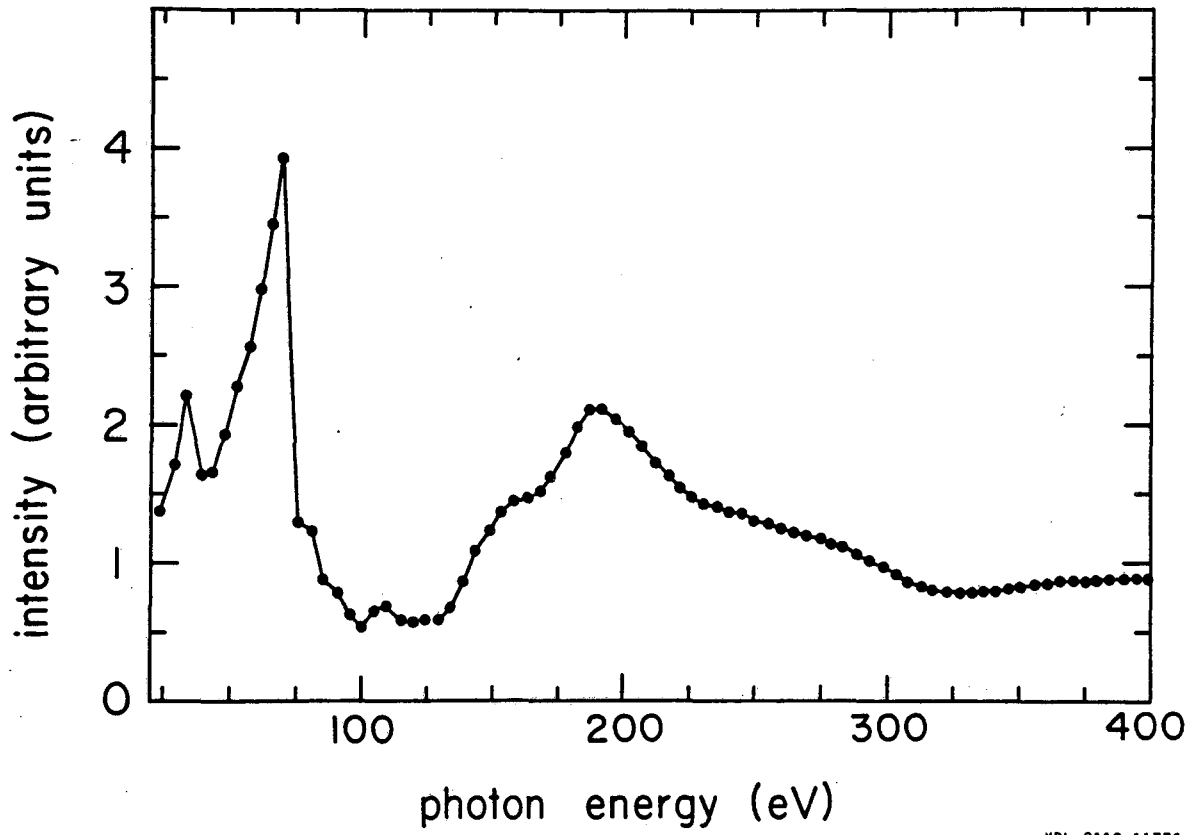Figure 4

XBL 817-10544
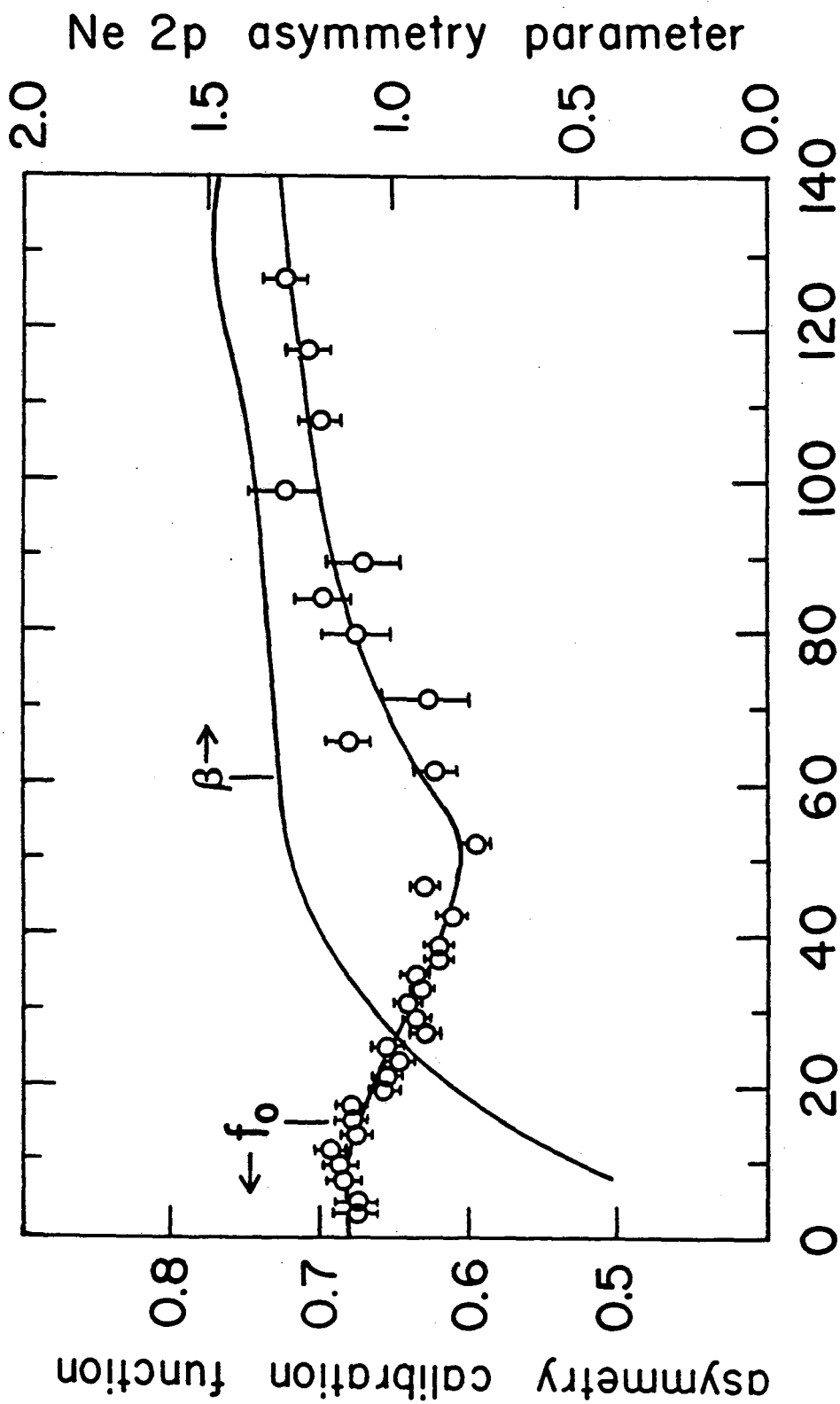
Figure 5

XBL 8110-11767

Figure 6

XBL 809-11808

Figure 7

XBL 8110-11776

III. ELECTRON SPECTROSCOPY STUDY OF INNER-SHELL PHOTOEXCITATION AND IONIZATION OF XE

A. Introduction

Among the initial studies of inner-shell photoionization processes were measurements and calculations on atomic Xe. The photoabsorption cross section of Xe displays a strong, broad maximum centered near 100 eV and a weaker, very broad maximum between 200-500 eV.[1-3] These features have been attributed to a shape resonance (centrifugal barrier effect) and a Cooper minimum in the 4d subshell photoionization cross section.[4-6] The central-field[5] and Hartree-Fock[6] calculations indicate that 4d photoemission dominates the total photoabsorption cross section over the energy range from the 4d ionization threshold ($h\nu \simeq 68$ eV) to the 3d threshold ($h\nu \simeq 680$ eV). Subsequently, many-electron photoionization calculations[7-10] and photoelectron spectroscopic measurements[11-14] demonstrated that the outer-shell 5p and 5s photoemission processes are strongly affected by electron-correlation interactions with the 4d subshell (see Refs. 7, 9, and 15 for reviews).

Photoemission from the 4d subshell produces an excited ionic state which can decay by ejection of Auger electrons. $N_{4,5}OO$ Auger spectra recorded near the 4d ionization threshold have demonstrated a type of final-state correlation called the post-collision interaction (PCI).[16] Also, theoretical studies have predicted that Xe $N_{4,5}OO$ Auger electrons will be produced with photon-energy-dependent, anisotropic angular distributions, due to alignment of Xe$^+$ by photoionization.[17,18]

A prominent series of 4d → np Rydberg excitations has been recorded in photoabsorption spectra in the energy range $h\nu \cong 65-70$ eV.[3,19,20] Because of the centrifugal barrier for $\ell=3$ angular momentum, the 4d → nf Rydberg series is not observed. Several continuum channels are available for the decay of these 4d-excited resonant states.[21] Electron spectroscopy can be used to characterize the resonant photoionization process by measurement of the partial cross sections and branching ratios[22] and the angular distributions[23] of the ejected electrons. Electron spectra of Xe recorded at the 4d → np resonances have been reported in Refs. 16, 21, and 24.

The above cited work introduces the types of inner-shell photoexcitation and ionization processes which were studied experimentally in the present work. Synchrotron radiation from the soft X-ray beam line at SSRL was used to record time-of-flight (TOF) electron spectra of Xe at 0° and 54.7° with respect to the photon polarization vector over the energy range $h\nu \cong 60-190$ eV. (Experimental details are given in Chapter II.) From the spectra were determined the angular distribution asymmetry parameters β of Xe 5p, 5s, and 4d photoelectrons and of $N_{4,5}OO$ Auger electrons. In certain cases, the partial cross sections and/or branching ratios for photoionization or Auger ionization channels were also determined.

Two sets of spectra of Xe were recorded, obtained about a year apart. Fig. 1 shows an example from the first set of TOF spectra, which were recorded with a 5.3 Å (FWHM) monochromator bandpass. The 5p, 5s, and 4d photoelectron lines and the $N_{4,5}OO$ Auger spectrum

were recorded in this set of spectra over the photon energy range

$h\nu \simeq$ 70-190 eV, i.e., from just above the 4d ionization threshold to

near the 4d Cooper minimum. In the second set of spectra, two smaller

ranges of photon energy were studied. The $N_{4,5}OO$ Auger spectrum was

recorded with smaller monochromator bandpass and improved counting

statistics over the photon energy range $h\nu \simeq$ 68-82 eV. This is the

energy region near and just above the 4d ionization threshold, where

PCI effects occur and relatively large asymmetry parameters β are ex-

pected for the Auger electrons. We also recorded spectra through the

4d $\rightarrow$ np resonances between $h\nu \simeq$ 65-70 eV, where resonant Auger decay

competes with the 5p and 5s autoionization channels.

B. The 4d and 5p photoelectron asymmetries

In the spectra recorded over $h\nu \simeq$ 70-190 eV with 5.3 Å bandpass,

photoelectrons from the individual fine structure levels of the 4d and

5p subshells were not resolved. A peak in Fig. 1 at low TOF (high

kinetic energy) is due to the 4d subshell ionized by second-order pho-

tons. The second-order photolines were used to extend the β(4d) meas-

urements beyond the Cooper minimum. Good agreement was obtained be-

tween β(4d) values given by second-order light with values given by

first-order light at energies $h\nu \simeq$ 130-190 eV where the two sets of

measurements overlapped. The β(4d) and β(5p) results are listed in

Table I.

Figure 2 shows the measured β(4d) values along with the measure-

ments of Torop et al.[12] and theoretical curves obtained using

Hartree-Fock wave functions,[6] relativistic Dirac-Fock (DF)

calculations,[26] and the many-electron relativistic random-phase
approximation (RRPA).[27] The measurements confirm the predicted os-
cillatory energy variation of β(4d), which is primarily a nonrelativis-
tic, one-electron effect.[6] The sharp drop near threshold is due to
rapid variation of the Coulomb phase shifts, while the oscillation be-
tween $\epsilon \simeq$ 10-100 eV photoelectron energy is produced by variation of
the non-Coulombic phase of the f wave resulting from the centrifugal
barrier in the scattering potential. The final oscillation in β(4d)
occurs about the Cooper minimum where the f-wave radial matrix element
changes sign. Note, however, that the DF and RRPA theories predict
the position of the Cooper minimum more accurately.

In Fig. 3 are plotted the measured β(5p) values along with previ-
ous measurements[12,14,28] (see Ref. 29) and two theoretical curves based
on the random-phase approximation with exchange (RPAE).[8,9] The RPAE
is nonrelativistic but can include electron correlations.[7] The dashed
theoretical curve includes the 5p intrashell correlations only, while
the solid curve also accounts for intershell correlation with the 4d
subshell. The data clearly support the theoretical interpretation of
a strong intershell correlation (or interchannel coupling) effect on
β(5p). In this correlation process the 4d subshell undergoes virtual
photoexcitation, with the excitation passing to the 5p subshell via
Coulomb interaction.[7,9,15] The interchannel coupling produces a
prominent oscillation in β(5p) in the energy region of the delayed
maximum in the 4d photoionization cross section. The full oscillation
is observed experimentally in the present measurements. Other

theoretical calculations which, respectively, do[10,27] and do not[6,30] include interchannel coupling with the 4d subshell give $\beta(5p)$ results similar to the full and dashed curves in Fig. 3.

C. The $N_{4,5}OO$ Auger transitions

Based on the general theoretical analysis given by Flügge et al.,[17] it is expected that the Xe $N_{4,5}OO$ Auger electrons will be produced with anisotropic angular distributions, due to alignment of $Xe^+ {}^2D_{5/2}$ and $Xe^+ {}^2D_{3/2}$ by photoionization. As discussed in Chapter I, the asymmetry parameter β for an Auger transition is proportional to the alignment tensor A_{20}:

$$\beta(h\nu) = \alpha A_{20}(h\nu), \tag{1}$$

where α is determined by the Auger decay process and is independent of photon energy. The alignment tensor is nonzero when the magnetic sublevels of $Xe^+ {}^2D_{5/2}$ or ${}^2D_{3/2}$ are unequally populated. The analysis of Flügge et al. shows that A_{20} should always be nonzero for the case of photoemission from an atomic subshell with $j > 1/2$ and where the ionic state formed has total angular momentum $J > 1/2$.

The strength of the alignment, i.e., the value of A_{20}, is determined by the photoionization matrix elements. In a nonrelativistic model, a 4d electron is photoemitted into two dipole-allowed continuum waves: ϵp and ϵf. Theoretical analysis[17,18] shows that A_{20} is determined by the ratio

$$\gamma(\epsilon) = \sigma(4d \rightarrow \epsilon p)/\sigma(4d \rightarrow \epsilon f) \tag{2}$$

of the partial photoionization cross sections for the two channels. In

Eq. (2), ϵ represents the photoelectron kinetic energy. Specifically, Berezhko et al.[18] showed that the alignment tensor can be expressed as

$$A_{20} = C\left[\frac{1 + a\gamma}{1 + \gamma}\right] \quad , \tag{3}$$

where γ is the energy-dependent ratio defined in Eq. (2), and C and a are constants determined by angular momentum coupling coefficients (see Ref. 18). For $Xe^{+} {}^{2}D_{5/2}$, a = 7/2 and C = $(1/5)(2/7)^{1/2}$; for $Xe^{+} {}^{2}D_{3/2}$, a = 7/2 and C = 1/10.

In an independent-electron model, the photoionization cross sections are determined by the radial dipole matrix elements $R_{n\ell,\epsilon\ell\pm1}$ (Ref. 6). Thus, in the present example, the partial-wave branching ratio can be expressed as

$$\gamma(\epsilon) = (2/3)R_{4d,\epsilon p}^{2}/R_{4d,\epsilon f}^{2} \quad . \tag{4}$$

Berezhko et al.[18] have calculated $A_{20}(\epsilon)$ for Xe^{+} $(4d^{-1})$ using both Herman-Skillman and Hartree-Fock wave functions. A strong, energy-dependent alignment is predicted, arising from the centrifugal barrier and Cooper minimum in the 4d $\rightarrow$ ϵf channel. These are the same factors that produce oscillations in the 4d photoelectron asymmetry (Fig. 2).

Manson has provided us with a tabulation of Hartree-Fock photoionization calculations for the Xe 4d subshell, which were reported in Ref. 6. These calculations provide the partial-wave branching ratio $\gamma(\epsilon)$. This parameter is listed in Table II along with the resulting

value of $A_{20}(\epsilon)$ for $Xe^{+}\ ^{2}D_{5/2}$ calculated using Eq. (3). Results are given for both the length and velocity forms of the dipole operator. The values of $A_{20}(\epsilon)$ listed in Table II are similar to the Hartree-Fock results given in a graph in Ref. 18. Also listed in Table II are the resulting theoretical values for the Auger electron asymmetry parameter β for the case of a transition of the type

$$Xe^{+}(4d^{9}5s^{2}5p^{6}\ ^{2}D_{5/2}) \rightarrow Xe^{2+}(^{1}S_{0}) + e^{-}(\epsilon d_{5/2}) \quad . \tag{5}$$
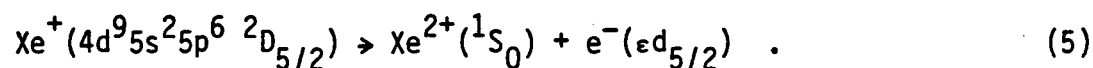
As discussed in Chapter I, the Auger decay coefficient α in Eq. (1) is determined only by angular momentum coupling coefficients when the Xe^{2+} final state has total angular momentum $J_{f} = 0$. For the $N_{5}00\ ^{1}S_{0}$ transition in Eq. (5), $\alpha = 4(2/7)^{1/2}$. A corresponding table of $A_{20}(\epsilon)$ for $Xe^{+}\ ^{2}D_{3/2}$ can be obtained using Eq. (3) and the values of $\gamma(\epsilon)$ listed in Table II. The decay coefficient $\alpha = 2$ for an Auger transition of the type $N_{4}00\ ^{1}S_{0}$:

$$Xe^{+}(4d^{9}5s^{2}5p^{6}\ ^{2}D_{3/2}) \rightarrow Xe^{2+}(^{1}S_{0}) + e^{-}(\epsilon d_{3/2}) \quad . \tag{6}$$
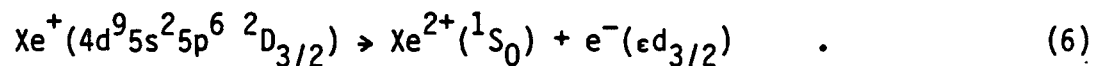
From the first set of Xe spectra recorded over $h\nu \simeq 70\text{--}190$ eV, asymmetry parameters β were determined for the Auger electron peaks numbered 1–4 in Fig. 1. The Auger spectrum was identified by comparison with the spectrum recorded and analyzed by Werme et al.[31] The Auger lines numbered 1 and 3 in Fig. 1 are produced, respectively, by the transitions of Eqs. (7) and (8):

$$Xe^+(4d^9 5s^2 5p^6 \, ^2D_{5/2}) \rightarrow Xe^{2+}(4d^{10} 5s^0 5p^6 \, ^1S_0) + e^- \tag{7}$$

$$\rightarrow Xe^{2+}(4d^{10} 5s 5p^5 \, ^1P_1) + e^- \quad . \tag{8}$$
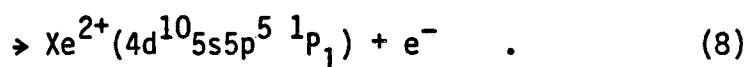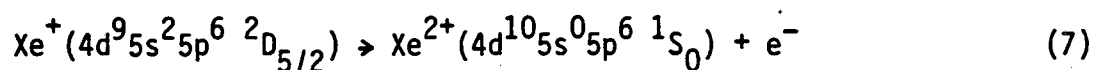
(This assignment of line number 1 (Eq. (7)) differs from that given in Ref. 31; assignments will be discussed below where the new Auger spectra are presented.) The measured β values for the Auger transitions $N_5 O_1 O_1 \, ^1S_0$ (Eq. (7)) and $N_5 O_1 O_{2,3} \, ^1P_1$ (Eq. (8)) are listed in Table III. To reduce scatter in the data, particularly at high photon energies, some of the results represent an average over two or three measurements obtained at nearby photon energies. The results are plotted in Fig. 4 along with theoretical curves for an Auger transition of the general type $N_5 OO \, ^1S_0$ (Eq. (5)). Thus, the measured β values for the $N_5 O_1 O_1 \, ^1S_0$ transition can be directly compared with the theoretical curves. The same alignment tensor $A_{20}(h\nu)$ is appropriate for describing the $N_5 O_1 O_{2,3} \, ^1P_1$ transition, but the Auger decay coefficient α might differ from that of Eq. (5). The coefficient α is determined by the matrix elements of the Coulomb operator and by the phases of the allowed continuum waves, which are $\epsilon P_{3/2}$, $\epsilon f_{5/2}$, $\epsilon f_{7/2}$ for the transition of Eq. (8).[33,34] Since the α parameters are independent of photon energy, however, the β values for the $N_5 O_1 O_{2,3} \, ^1P_1$ transition should differ only by a constant scale factor from the measured and theoretical β values for the $N_5 O_1 O_1 \, ^1S_0$ transition.

In Fig. 4, the data qualitatively follow the predicted energy variation of the Auger electron asymmetry parameter. Eqs. (1)-(3) show that the alignment is relatively strong, so that the Auger asymmetry is relatively large, where the 4d $\to$ ϵf photoemission transition strength is small relative to that of 4d $\to$ ϵp. Thus, the relatively large Auger asymmetry observed near the 4d ionization threshold is due to suppression of the f-wave channel at photoelectron energies below the centrifugal barrier, while the large Auger asymmetry at high photon energy occurs near the f-wave Cooper minimum. Similar energy dependences of β were observed for the four $N_{4,5}OO$ Auger peaks indicated in Fig. 1, as expected. Berezhko and co-workers extended their theoretical studies of alignment by using RPAE calculations to include the effects of many-electron correlations and electron shell rearrangement.[35] In the case of Xe^+ $(4d^{-1})$, the inclusion of these interactions produced a moderate shift in the energy position of the Cooper minimum feature, in comparison with the Hartree-Fock calculation, but did not alter the general form of $A_{20}(\epsilon)$.

Fig. 4 shows that the measured β values of the $N_5O_1O_1$ $^1S_0$ transition are in reasonably good agreement with theory, and that, at lower energies, $\beta(N_5O_1O_{2,3}$ $^1P_1) < \beta(N_5O_1O_1$ $^1S_0)$. The latter observation could be due to the difference in the α coefficients as discussed above. However, it will be seen that the new β(Auger) measurements recorded just above the 4d ionization threshold are somewhat higher than the first results plotted in Fig. 4, and that no variations are observed among different Auger transitions. The new results are to

be preferred, primarily for the following reasons. Though the signal-to-background was not greatly improved, the new spectra were obtained with superior counting statistics, particularly near the 4d ionization threshold. For both sets of spectra, background subtraction was an important factor in determining the relative areas of the $0°$ and $54.7°$ peaks (and hence in determining β). Thus, errors in background subtraction could create discrepancies. The new set of TOF spectra were recorded with a smaller time window which covered only the kinetic energy range of the Auger electrons (compare Figs. 1 and 6). This gave more collection channels per nsec and an effectively better resolution of the $N_{4,5}O_1O_{2,3}$ $^1P_1$ Auger peaks (numbered 3 and 4 in Fig. 1; numbered 1 and 2 in Fig. 6). Also, the first spectra were recorded with a much larger photon bandpass (5.3 Å FWHM; 2 eV at $h\nu = 70$ eV) than the new spectra (2.6 Å FWHM; 1 eV at $h\nu = 70$ eV). Some other factors which could in principle create a discrepancy, such as second-order light and uncertainty in the calibration of the energy scale of the monochromator, appear not to be significant. In short, we regard the first results (Fig. 4) to be qualitatively correct but prefer the new results for a quantitative comparison with theory. Additional discussion of the theoretical interpretation of β(Auger) will be given below where the new results are presented.

Before discussing the new Auger spectra and results, I give an additional result obtained from the first set of spectra. Listed in Table IV and plotted in Fig. 5 are values of the branching ratio $N_5OO:N_4OO$ between Auger lines produced by transitions of N_5 and N_4 core holes to the same Xe^{2+} final state. This branching ratio was

determined for the two pairs of lines 1,2 and 3,4 in Fig. 1, which are identified as $N_5O_1O_1, N_4O_1O_1$ ($^1S_0$) and $N_5O_1O_{2,3}, N_4O_1O_{2,3}$ ($^1P_1$), respectively. No strong variations were observed between the two sets of branching ratios, so the average values are given in order to reduce the scatter in the measurements. Also plotted in Fig. 5 are a theoretical curve[36] and experimental data[37-39] for the $4d_{5/2}:4d_{3/2}$ photoelectron branching ratio itself. The Auger electron branching ratio closely follows the corresponding photoelectron branching ratio. This is the result expected if no variation occurs between the decay patterns for the two fine structure levels, i.e., a variation in the branching ratios for decay to the various Xe^{2+} final states.

Figure 6 shows an example from the new set of $0°$ and $54.7°$ TOF spectra of the Xe $N_{4,5}OO$ Auger electrons. Spectra were recorded over the energy range $h\nu = 67.7-81.9$ eV with a monochromator bandpass of 2.6 Å FWHM. Since the Auger electron energies are independent of $h\nu$, there are contributions to the Auger peaks by second- and higher-order diffracted light and by scattered light in the photon beam. These contributions could interfere with the measurements of the Auger electron asymmetry parameters and branching ratios. The contributions to the Auger electron peaks depend on the relative intensities of the components of the photon beam and on the relative photoionization cross section of the 4d subshell at the component photon energies. We determined the order-composition of the photon beam over the energy region of the Auger spectra by recording $54.7°$ TOF spectra of Ne. Dividing the intensities of the first- and higher-order photolines of

Ne by the corresponding photoionization cross section[40] yields the relative intensities of the order-components of the photon beam. Scattered light appeared to be insignificant in this energy range. From the order-composition of the photon beam and the relative photoionization cross section of the Xe 4d subshell,[41] we determined that the first-order light contributed about 95% of the Auger electron signal in our spectra. Therefore, higher-order light contributions to the results appear negligible.

Not shown in Fig. 6 are the $N_{4,5}O_{2,3}O_{2,3}$ Auger lines which were not resolved in our spectra due to their higher kinetic energies and closer spacings. Only the lower energy, intense lines numbered 1-7 in Fig. 6 were analyzed for asymmetry parameters and branching ratios. A disadvantage to this situation is that some of these lower energy Auger lines, which result from transitions to higher energy levels of Xe III, are presently not well assigned. Good correspondence was obtained between the present spectra and the high-resolution spectrum recorded by Werme et al.[31] using electron impact excitation. The $N_{4,5}-O_{2,3}O_{2,3}$ and $-O_1O_{2,3}$ series of lines were assigned by Werme et al. by comparison with the spectroscopically observed[42] levels of Xe III. Thus, lines 1 and 2 in Fig. 6 are the $N_{4,5}$-pair identified with the final state $5s5p^5 \, {}^1P_1$. Lines 3,5 and 6,7 are also $N_{4,5}$-pairs. Werme et al. used the Moore tables[42] to identify line 4 as the N_5 line produced by transition to the final state $5s^2 5p^3({}^2P)6s \, {}^1P_1$. Hence, this line was termed a satellite, thought of as originating from shake-up in the Auger process. However, the $N_{4,5}$-pairs 3,5 and

6,7 could not be assigned using Ref. 42, since they are produced by final states at higher energies than has been reported in the spectroscopic tables. One of these two pairs of lines should be the $N_{4,5}O_1O_1$ lines and the other, presumably, satellites. Thus, since the $5s^0 5p^6$ level had not been observed spectroscopically, and intense satellite lines are also present in the Auger spectrum, the $N_{4,5}O_1O_1$ lines could not be identified with certainty by Werme et al. A similar situation occurred in the analogous case of the $M_{4,5}NN$ spectrum of Kr, which was also reported in Ref. 31. By comparison with assignments of the corresponding $ns^0 np^6$ final states in Kr and the other rare gases,[43] Werme et al. assigned lines 3 and 5 in Fig. 6 as $N_{4,5}O_1O_1\ {}^1S_0$. By comparison also with the Kr $M_{4,5}NN$ spectrum, the lowest energy lines 6 and 7 were attributed to the satellite final state $5s^2 5p^3 (^2P) 7s\ {}^1P_1$.

Subsequently, the theoretical studies of Larkins and of McGuire[44] indicated that the $M_{4,5}N_1N_1$ transitions in Kr be reassigned as the lowest energy intense lines, which previously were identified as satellites. Similarly, the Xe $N_{4,5}OO$ Auger-electron energies calculated semiempirically,[45] i.e., using experimental binding energies and Hartree-Fock values for Slater integrals, indicate that lines 6 and 7 in Fig. 6 be identified as $N_{4,5}O_1O_1\ {}^1S_0$, and this is the assignment that we adopt. This revised assignment appears also to have been adopted in Ref. 21 for the corresponding resonant-Auger spectrum.

This leaves lines 3 and 5 still to be reassigned. We propose that they be identified as satellites associated with the $5s5p^5\ {}^1P_1$ primary configuration, i.e., they are satellites of the $N_{4,5}O_1O_{2,3}\ {}^1P_1$ lines

(1 and 2). It seems likely that all of the lines in between the $N_{4,5}$-pairs 1,2 and 6,7 are of this origin. This proposed identification is based on the corresponding case of the Xe^+ $5s5p^6$ $^2S_{1/2}$ photoline with its associated set of intense satellites observed in photoelectron spectra (see, for example, Refs. 46 and 47). The $5s5p^6$ satellites occur in the energy region of the $5s^2 5p^4(SL)n\ell$ levels[42] (note that Hansen and Persson[48] have given revised identifications of these levels). Theoretical studies[47-49] indicate that the $5s5p^6$ satellites arise primarily through correlation processes which can be described as final ionic state configuration interaction (FISCI).[50] The FISCI mechanism requires that the satellite lines arise from states that have the same total angular momentum and parity as the primary ionic configuration $5s5p^6$ $^2S_{1/2}$. Hence, Hansen and Persson[48] have assigned the satellites to even parity states of the type $5s^2 5p^4(SL)nd$ and $5s^2 5p^4(SL)ns$ which have total angular momentum $J = 1/2$. The primary and satellite LSJ configurations become strongly mixed by electron correlation, so it is not entirely accurate to label the observed levels with a particular configuration.[48] A detailed description of the origin of these satellites might involve a combination of types of many-electron interactions;[47,49] however, the FISCI mechanism appears to be the dominant process.

We propose that the satellite lines in the Xe $N_{4,5}$OO Auger spectrum result correspondingly from interaction among the Xe^{2+} configurations $5s5p^5$, $5s^2 5p^3(SL)nd$, and $5s^2 5p^3(SL)ns$ with total angular momentum $J = 1$. The most intense satellites of Xe^+ $5s5p^6$ are due to the $5s^2 5p^4 5d$

and $5s^2 5p^4 6d$ configurations, and the $5s^2 5p^4 ns$ contributions appear to be less important.[47-49] Hansen and Persson[48] identify the strongest satellite with the level $5s^2 5p^4 (^1D) 5d\ ^2S_{1/2}$, which lies at 5.48 eV higher binding energy than the primary line $5s5p^6\ ^2S_{1/2}$. The strongest $N_{4,5}$-pair of satellites in the Auger spectrum (lines 3 and 5) also lie at 5.5 eV from the primary lines 1 and 2. Therefore, we tentatively identify lines 3 and 5 with the final state $5s^2 5p^3 (^2P) 5d\ ^1P_1$. As mentioned above, line 4 was originally identified with the final state $5s^2 5p^3 (^2P) 6s\ ^1P_1$, by comparison with the spectroscopic data.[42] However the table of the corresponding $5s^2 5p^4 n\ell$ levels of Xe II have been reassigned,[48] and similar reassignments may apply to the table of Xe III levels. We consider line 4 also to be a satellite and originating from the N_5 core hole, but leave the final state unassigned. The present assignments of lines 1–3 and 5–7 are listed in Table V.

We have proposed that the satellite lines in the Auger spectrum arise from final state configuration mixing, in analogy with the FISCI satellites of the 5s photoline. However, note that the Auger satellites are very intense. The $N_{4,5}$-pair of satellite lines 3,5 are slightly stronger than the primary lines 1,2, and the total satellite intensity is 2–3 times as great as that of the primary lines. Other types of electron correlation mechanisms may be important, such as those described by initial state configuration interaction (ISCI).[50] In the ISCI mechanism, pair–excited configurations of the type $4d^9 5s^2 5p^4 nd^2\ ^2D$ could contribute to the initial state of the Auger process. These $5p^2 \rightarrow nd^2$ configurations in the initial state provide

an additional mechanism for populating satellites in the final state.[51] In short, theoretical studies are needed both to confirm and to quantify the proposed identification of the Auger satellite lines. It appears that this would provide an interesting system for theoretical study of electron correlation.

The 54.7° TOF Auger spectrum recorded at $h\nu = 67.7$ eV is shown in Fig. 7. This photon energy lies just above the $4d_{5/2}$ ionization threshold (67.55 eV), but below the $4d_{3/2}$ threshold (69.52 eV); actually, $h\nu$ lies in between the $n = 6$ and 7 members of the $4d_{3/2} \rightarrow np$ Rydberg series.[19,20] Since the N_4 vacancy is not produced at this energy, only the N_5OO Auger lines appear in the spectrum. Comparison with Fig. 6 indicates a slight shifting of the Auger lines to smaller TOF (higher kinetic energy) and a broadening. These effects are attributed to the post-collision interaction (PCI) among the photoelectron, Auger electron, and atomic ion following near-threshold photoionization.[16]

Because of the nonlinear variation of the energy scale in a TOF spectrum (see Fig. 6), the shifting and broadening are most noticeable for the lowest energy line, number 7, which we have assigned as $N_5O_1O_1 \, ^1S_0$. In Fig. 8 are plotted the 54.7° TOF spectra of line 7 recorded just above the $4d_{5/2}$ ionization threshold and at 14.4 eV above threshold. The broadening and shifting of the line are apparent in this comparison.

It should be explained how we obtained the kinetic energy scales given with the TOF spectra in Figs. 6 and 8. The spectra are recorded with a fixed time scale, i.e., a constant number of collection channels per nsec, which is determined using a delay generator to calibrate the timing circuit with known time intervals. To convert the channel numbers to an actual TOF scale, the channel corresponding to TOF = 0 nsec is found. This channel can be taken to be that near the prompt signal (TOF ≃ 1 nsec) which results from Rayleigh scattering of the photon beam from the sample gas.[52] If the prompt signal is not recorded, the TOF = 0 channel is determined as a fitting parameter. Each collection channel in the TOF spectrum can then be converted to the corresponding kinetic energy if the path length between the source region and the detector is known. The path length is always known to within a few percent. The actual value used for energy conversion is adjusted slightly to best fit the peak positions to known kinetic energies. In Table V are listed the kinetic energies of the Auger lines determined by energy conversion of the TOF spectrum in Fig. 6. The energy-converted values agree well with the measurements of Werme et al.

The point to be emphasized here is that the TOF spectra can be used to measure small energy shifts, such as occur due to the PCI effect. Table V shows that a fairly accurate energy conversion was obtained over a range of about 13 eV. Therefore, small energy shifts, amounting to a few percent of this range, are accurately determined. For the set of Auger spectra recorded over $h\nu$ = 67.7–81.9 eV, no adjustments were made to the detector position or the timing circuit, so

the energy-conversion parameters (the path length and the channel at which TOF = 0) were the same. Thus, the correspondence between channel number and energy was fixed. In Fig. 8 are plotted the same set of channel numbers for two spectra recorded at different photon energies; the TOF and kinetic energy scales apply to both spectra.

Niehaus has developed a semiclassical model which describes PCI effects on Auger decay for the case of inner-shell photoionization.[53] Near the ionization threshold, the photoelectron is still close enough to the ionic core, at the time of ejection of the Auger electron, to effectively modify the Coulomb field in which the Auger decay occurs. Energy exchanges occur between the "slow" photoelectron and the "fast" Auger electron. The Auger lines exhibit an asymmetric broadening, with the maxima of their energy distributions shifted to higher energy. The lines in the present TOF spectra generally have asymmetric shapes anyway, due to the asymmetric shape of the source region of ejected electrons which are collected by the detectors.[52] However, the shifting and broadening effects are apparent in Fig. 8.

In the semiclassical model of Niehaus, the shift ϵ of the maximum of the energy distribution of the Auger line, with respect to its position in the absence of PCI, is related to the core-hole lifetime τ and photoelectron energy E by the expression[54] (in atomic units)

$$\tau^{-1}[2(E + \epsilon)]^{1/2} - \epsilon(4E + 5\epsilon) = 0. \tag{9}$$

Here, the "photoelectron energy" is a parameter (the "excess energy"), strictly defined as $E = h\nu - I$, where I is the ionization energy. The

photoelectrons give up some energy to the Auger electrons. Also, Eq. (9) applies for negative values of E. In this model, the shift ϵ is determined only by the energy E and the decay width $\Gamma = \tau^{-1}$. The recent measurements of Schmidt et al.[16] of the shift ϵ for the Xe $N_5 O_{2,3} O_{2,3} {}^1S_0$ line fit well to the theoretical relation of Eq. (9) with a value $\Gamma = 110$ meV for the level width. This value for Γ agrees well with the widths of the 4d $\rightarrow$ np resonances measured in the photo-absorption spectrum,[20] and not quite as well with those determined from electron energy-loss spectroscopy.[55]

From the present set of TOF spectra, we measured the relative shift $\Delta\epsilon$ of the $N_5 O_1 O_1 {}^1S_0$ peak with respect to its position at hν = 81.9 eV (note that with a width $\Gamma = 110$ meV, Eq. (9) predicts an absolute shift $\epsilon = 53$ meV at h$\nu = 81.9$ eV). The peak maxima were found by eye, which could be done to within about ± 2 channels. This uncertainty gave the error bars for the relative shifts, which are listed in Table VI. Similar shifts were observed for the other $N_5 OO$ lines.

Schmidt and co-workers[56] first reported observations of the shifting and asymmetric broadening of Auger lines for the case of near-threshold inner-shell photoionization. They have recently reported a more extensive set of measurements, in which the experimental details were carefully accounted for.[16] The reader is referred to Ref. 16 for a complete discussion of this particular type of PCI phenomenon and a detailed comparison of experiment with theory. The main objective here has been to establish the presence of the PCI factor in our spectra. Nevertheless, Fig. 9 shows that the present measurements

of the Auger line shift ϵ are in excellent agreement with the theoretical relation Eq. (9) for a decay width $\Gamma = 110$ meV, which was found also to predict very well the measurements reported in Ref. 16.

It is important to explain some differences between the present results and those reported by Schmidt et al.[16] Since a residual shift of $\epsilon = 53$ meV is expected (Eq. (9), with $\Gamma = 110$ meV) at our reference energy of $h\nu = 81.9$ eV, the present results plotted in Fig. 9 are values $\epsilon = \Delta\epsilon + 53$ meV, where $\Delta\epsilon$ is the relative shift listed in Table VI. The results reported in Ref. 16 are relative shifts $\Delta\epsilon$ measured with respect to the Auger line position at $h\nu = 110$ eV, where there is a residual shift of 31 meV. However, Schmidt et al. took account of the variation of the theoretical Auger line energy distribution when convoluted with their spectrometer function. With this correction, the theoretical prediction for the relative shift $\Delta\epsilon$ appropriate to their data is essentially identical to the uncorrected theoretical curve for the absolute shift ϵ over the energy range plotted in Fig. 9. Therefore, both sets of measurements may be compared with the theoretical curve in Fig. 9. The excellent agreement of the present results with those of Ref. 16 and theory seems somewhat fortuitous, considering the large photon bandpass used and that no account was taken of the effect of the spectrometer function. However, the PCI effect is clearly demonstrated, at least qualitatively, in the spectra of Fig. 8.

The areas of the Auger peaks in the $0°$ and $54.7°$ TOF spectra were obtained using a least-squares curve fitting routine. The peaks were fitted to the form of asymmetric Gaussian functions with a linear background. The curves drawn through the spectra shown in Fig. 8 are examples of these fits. In the deconvolution of lines 3-5 (see Fig. 6), a weak Auger line (number 26 in Ref. 31) in between lines 4 and 5 was included. The results for the asymmetry parameters β are listed in Table VII. Values are not given for one or two Auger lines at the higher photon energies due to overlapping by the 4d photoelectrons.

The β values for the three pairs of $N_{4,5}OO$ Auger lines are plotted in Fig. 10. The theoretical curve is that for a transition of the general type N_5OO $^1S_0$, and was obtained using the Hartree-Fock (HF) calculations[6] of the partial-wave photoionization cross sections and Eqs. (1)-(3). As can be seen from Table II, the β values based on the HF-length and the HF-velocity calculations differ by only 0.01-0.04 β units over the energy range of the experimental data. Hence, we have used the average of the length and velocity results for the theoretical curve in Fig. 10. In the presently adopted nonrelativistic model of the photoionization process, the same partial-wave branching ratio $\gamma(\epsilon)$ (Eq. (2)) applies to both the N_5 and N_4 hole states at the same photoelectron energy ϵ. Thus, the alignment tensors $A_{20}(\epsilon)$ for the $^2D_{5/2}$ and $^2D_{3/2}$ states differ by a constant factor determined by the two values for the constant C in Eq. (3). Taking account of this factor and another due to the difference in the decay parameters α in Eq. (1), the result is that at a given photoelectron

energy, $\beta(N_4OO\ ^1S_0) = (7/8)\beta(N_5OO\ ^1S_0)$. On a photon energy scale, however, the theoretical curve for an $N_4OO\ ^1S_0$ transition is shifted by 2 eV from that for an $N_5OO\ ^1S_0$ transition due to the N_5-N_4 spin–orbit splitting. As a result, the theoretical curve for $\beta(N_4OO\ ^1S_0)$ essentially overlaps the one plotted in Fig. 10 for $\beta(N_5OO\ ^1S_0)$, i.e., the two transitions should have nearly the same β at a given photon energy.

The results for the $N_{4,5}O_1O_1\ ^1S_0$ lines show that indeed the N_4- and $N_5-OO\ ^1S_0$ lines have about the same β values at the same photon energy, and that the theoretical curve predicts the measured asymmetries very well. The measurements also show that all of the Auger lines, independent of final state, have the same β values. This result shows that the Auger decay parameters α do not greatly differ among the transitions studied here. As predicted, the asymmetry parameters are relatively large near threshold where the 4d $\rightarrow$ εp photoionization channel dominates due to the centrifugal barrier for the f wave. The measurements follow the theoretical curve well from threshold as β steadily decreases, but the data drop somewhat below the curve near 76 eV. Within the precision of the measurements, the overall agreement with theory is good. This conclusion holds even if the original assignment[31] of the $N_{4,5}O_1O_1\ ^1S_0$ lines is correct, since all of the low energy lines studied here have the same β values.

It can be seen from the theoretical expression Eq. (3) that the alignment tensor has a maximum value $A_{20}(\text{max}) = Ca$ for $\lambda \gg 1$ and a minimum value $A_{20}(\text{min}) = C$ for $\lambda \ll 1$. Accordingly, the Auger electron asymmetry parameters also have limited ranges: $\alpha C \leq \beta \leq \alpha Ca$.

For example, $0.229 \leq \beta(N_5OO\ ^1S_0) \leq 0.8$ and $0.2 \leq \beta(N_4OO\ ^1S_0) \leq 0.7$.

Hence, A_{20} and β are not very sensitive to very large or very small values of γ, where asymptotic values are approached. The central 90% of the ranges of A_{20} and of β occur for γ values in the range $1/19 \leq \gamma \leq 19$.

Inverting Eq. (3) and using Eq. (1) gives an expression for γ as a function of β:

$$\gamma = \frac{\beta - \alpha C}{\alpha Ca - \beta} \qquad (10)$$

Thus, β(Auger) measurements can be used to determine the partial-wave branching ratio. The γ values determined using the present set of β measurements for the $N_{4,5}O_1O_1\ ^1S_0$ lines are in qualitative agreement with the Hartree-Fock calculations, which follows considering the good agreement shown in Fig. 10. However, the uncertainties in our β measurements translate into very large uncertainties in γ, particularly for the very large and very small γ values, where β is less sensitive to the precise value of γ. A big improvement in the precision of the β measurements would be required to make a quantitative determination of the large values of γ produced near threshold or near the Cooper minimum.

The $N_5OO:N_4OO$ Auger electron branching ratios, which could be measured for three final states, are listed in Table VIII. A few very weak Auger lines, which were not resolved in our spectra, occur near the $5s5p^5\ ^1P_1$ lines (see Ref. 31). These could cause small errors in the branching ratios for this final state. The measurements for the final states $5s^25p^3(^2P)5d\ ^1P_1$ and $5s^05p^6\ ^1S_0$ are plotted in Fig. 11 along with a theoretical curve[36] and measurements[37,38] for the

$4d_{5/2}:4d_{3/2}$ photoelectron branching ratio. The Auger electron ratios agree well with the corresponding photoelectron ratios. The Auger measurements confirm indirectly that the $4d_{5/2}:4d_{3/2}$ ratio increases from threshold, as predicted, before decreasing at higher energy.

Somewhat larger values of the Auger branching ratio were measured near threshold for the $5s^0 5p^6\ {}^1S_0$ final state than for the other two final states. The first set of TOF Auger spectra also gave a larger ratio near threshold for the $5s^0 5p^6\ {}^1S_0$ lines than for the $5s5p^5\ {}^1P_1$ lines. However, this distinction was not observed at higher energies where the ratios are smaller. This variation with final state of the $N_5 OO:N_4 OO$ ratio may be due simply to the kinetic energy dependence of the Coulomb matrix element. The 2 eV difference in the $N_4 OO$ and $N_5 OO$ energies is comparatively largest for the $5s^0 5p^6\ {}^1S_0$ lines, which occur at the lowest kinetic energies. Thus, the largest variation of the Coulomb transition strength would occur for those lines.

Also of interest are the intensity ratios for Auger decay to the various final states. Those ratios were determined for the four intense $N_5 OO$ transitions which were analyzed in our spectra (line numbers 2, 4, 5, and 7 in Fig. 6). In the spectra recorded at energies $h\nu \geq 69.7$ eV, the intensity ratios were constant to within 5%. Relative to line number 2, the measured intensity ratios for the line numbers 7:5:4:2 were 125:158:99:100. Except for the $5s^0 5p^6\ {}^1S_0$ final state (line number 7), the present results are in fairly good agreement with intensity ratios measured by Werme et al. using electron impact excitation; the ratios reported in Ref. 31 are 166:168:93:100.

In the two spectra recorded nearest the N_5 threshold, there was an indication of a variation of the intensity ratios from the constant values measured at higher energies. However, this result cannot be reported with certainty based on our limited set of data.

In discussing the results of the Auger electron measurements we have adopted the two-step model of the Auger process in which the formation of the inner-shell vacancy state and its decay are considered to be independent processes. This approximation appears to be valid at photon energies far enough above the 4d ionization threshold, but the effects of PCI displayed in Figs. 8 and 9 demonstrate that the two-step model breaks down near threshold. In the near threshold region, the photoionization and Auger decay are more properly treated as a single process.[58] However, the present measurements of Auger electron angular distributions and branching ratios appear to be well described by the two-step model.

D. Autoionization of the 4d → np resonances

Photoabsorption spectra[19,20] of Xe recorded through the energy region $h\nu \approx$ 65-70 eV display two Rydberg series of excitations which are described by the transitions

$$h\nu + Xe(4d^{10}5s^2 5p^6\ {}^1S_0) \rightarrow Xe(4d^9 5s^2 5p^6 ({}^2D_{5/2,3/2})np\ {}^1P_1), \qquad (11)$$

where n = 6, 7, 8, ... These are the series of $4d_{5/2} \rightarrow np$ and $4d_{3/2} \rightarrow np$ resonant excitations which have as series limits the $(4d^{-1})\ {}^2D_{5/2}$ and ${}^2D_{3/2}$ ionic states. Since these "discrete" levels
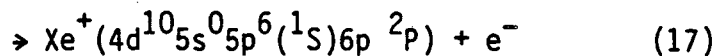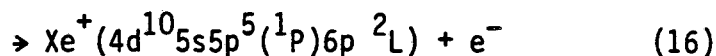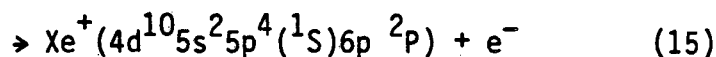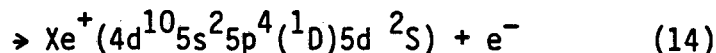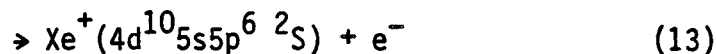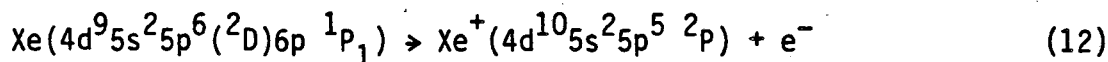
lie energetically above several lower ionization thresholds, they decay by autoionization into the accessible continuum channels. Autoionization is a type of interchannel interaction. Fano has used the configuration-interaction formalism to describe the mixed discrete-continuum nature of an autoionizing state and to parameterize the resonance lineshape of the photoabsorption spectrum.[59] However, much more detailed information on the autoionization process is obtained by using electron spectroscopy to observe resonance effects on the individual final states. The magnitudes and phases of the photoionization amplitudes can vary rapidly through a resonance, resulting in resonance structure in the cross sections, angular distributions, and spin-polarization parameters.[22,23,60] Starace has extended Fano's theory to describe partial photoionization cross sections and photoelectron branching ratios within an isolated resonance.[22] Similarly, Kabachnik and Sazhina have formulated the resonance behavior of the photoelectron angular distribution and spin polarization.[23] In the general case, however, there are several overlapping Rydberg series, which interact. A unified and comprehensive description of autoionization in this general case is obtained using the multichannel quantum-defect theory (MQDT).[61] For the entire resonance region, the MQDT generates resonance profiles for all of the dynamical parameters which can be observed using electron spectroscopy, i.e., partial photoionization cross sections and the photoelectron asymmetry and spin-polarization parameters.[62]

In the present experiment, the Xe 4d → np resonances were located by recording photoelectron excitation spectra such as the one shown in Fig. 12. Photoelectrons from both the $0°$ and $54.7°$ TOF detectors were collected in this spectrum as the monochromator was stepped through the resonance region. The spectrum was recorded at a fixed sample gas density, but is uncorrected for variation of the photon beam intensity, which increased by about 50% from $h\nu = 63$ eV to 72 eV. A "window" was placed on the time-to-amplitude converter of the detector circuit so that only the resonantly produced Auger electrons[21,24] were counted, i.e., the 5p and 5s photoelectrons were excluded. It was found that the resonance structure in the excitation spectrum was much less distinct when the 5p and 5s photoelectrons were included. Since the Auger electrons are only produced as a result of 4d excitation, they are highly sensitive to the resonance structure in the photoabsorption spectrum.

In Fig. 12 and following figures we use the notation $4d^{-1}(^2D_{5/2})$ or $4d^{-1}(^2D_{3/2})$ to represent a vacancy in the 4d subshell. The resonance line positions and ionization thresholds reported by Codling and Madden[19] are indicated in Fig. 12. The shapes and intensities of the resonance features in Fig. 12 are in accordance with the high resolution photoabsorption spectrum.[20] The strongest excitations, $4d_{5/2}$ → 6p and $4d_{3/2}$ → 6p, stand out, and smaller features also appear, due to the 4d → 7p transitions. Excitation spectra served both to calibrate the energy scale of the monochromator and to determine the photon bandpass. The spectrum in Fig. 12 was recorded with the

smallest bandpass used in these experiments, 1.2 Å FWHM (0.4 eV at

$h\nu$ = 65 eV). Our bandpass was considerably larger than the natural

widths ($\Gamma \simeq 0.1$ eV) of the resonances.[20] The energy calibration of

the monochromator appears to be accurate to within ± 0.1 eV in the en-

ergy region of the resonances, based on the reproducibility of the ob-

served position of the $4d^{-1}(^2D_{5/2})6p$ peak in several excitation spec-

tra.

Several final states could be populated by the decay of the 4d → np

resonances. Consider the following possible decay channels following

4d → 6p photoexcitation:

$$Xe(4d^9 5s^2 5p^6 (^2D)6p\ ^1P_1) \rightarrow Xe^+(4d^{10}5s^2 5p^5\ ^2P) + e^- \tag{12}$$

$$\rightarrow Xe^+(4d^{10}5s5p^6\ ^2S) + e^- \tag{13}$$

$$\rightarrow Xe^+(4d^{10}5s^2 5p^4 (^1D)5d\ ^2S) + e^- \tag{14}$$

$$\rightarrow Xe^+(4d^{10}5s^2 5p^4 (^1S)6p\ ^2P) + e^- \tag{15}$$

$$\rightarrow Xe^+(4d^{10}5s5p^5 (^1P)6p\ ^2L) + e^- \tag{16}$$

$$\rightarrow Xe^+(4d^{10}5s^0 5p^6 (^1S)6p\ ^2P) + e^- \tag{17}$$

In all of these decay processes at least two electrons change quantum

numbers: one fills the 4d vacancy and another is ejected. Processes

(12) and (13) are the usual "autoionization" transitions: the 6p

Rydberg electron changes quantum numbers, and the final states are the

primary "one-electron" ionic states, which are also produced off res-

onance by direct ionization. Transition (14) represents a (formally)

more complicated combination of autoionization and final ionic state configuration interaction (FISCI), which was discussed earlier. The final state of Eq. (14) represents a FISCI satellite of the 5s photo-line[48] and is also produced off resonance. The transitions of Eqs. (15)-(17) are "Auger" processes and differ qualitatively from those of Eqs. (12)-(14). The 6p electron remains in the final state while one O-shell electron fills the 4d vacancy and another is ejected. The final states are the same as those formed by $N_{4,5}OO$ Auger decay above the ionization threshold, but with a 6p "spectator" electron remaining. These resonant Auger final states occur in the same energy region as the FISCI satellites of the 5s photoline, but are not observed to be produced off resonance by direct ionization.

In Fig. 13 are shown 54.7° TOF spectra of Xe recorded at photon energies both on and off resonance, with a bandpass of 1.7 Å FWHM (0.6 eV at $h\nu$ = 65 eV). The spectra have been scaled in the figure to account for variations in the photon beam intensity, sample gas density, and collection time. The relative transmission of the detector was approximately constant over the range of electron energies recorded in the spectra. Hence, the areas of the peaks as they appear in the figure are proportional to the partial photoionization cross sections. The first spectrum in Fig. 13 was recorded at $h\nu$ = 63.4 eV, which is below the resonance region, so only direct ionization occurs. The photolines produced are the 5p, 5s, and 5s satellites. The 5s satellites[46] have been assigned[48] to configurations of the type $5s^2 5p^4(SL)nd$ and $5s^2 5p^4(SL)ns$. The spectrum recorded at $h\nu$ = 65 eV,

i.e., at the $4d^{-1}(^2D_{5/2})6p$ resonance, is highly modified from the off-resonance spectrum. The series of lines labeled $5s^25p^4n\ell$ are strongly enhanced, and a set of lower energy lines, with considerable intensities, also appear. These results are attributed to the Auger decay of the resonant state. The enhanced intensity of the lines labeled $5s^25p^4n\ell$ is due to the Auger final states $5s^25p^4(SLJ)6p$, rather than the 5s satellites which occur in the same energy region. Higher resolution electron spectra recorded at this resonance by Eberhardt et al.[24] and others[16,21] show that these Auger lines are accompanied by strong shake-up transitions to the levels $5s^25p^4(SLJ)7p$. The spectrum recorded at $h\nu = 65.8$ eV is again off resonance, and only the direct ionization final states are observed. In the 67 eV spectrum, recorded at the $4d^{-1}(^2D_{3/2})6p$ resonance, the Auger final states are again produced.

The resonant Auger spectra in Fig. 13 have the same general appearance as the Auger spectrum recorded above the 4d ionization threshold (compare with Fig. 1 and the spectrum of Werme et al.[31]). However, in the resonant spectra only one line appears for each final state, while two lines per final state are produced above threshold due to decay from both of the N_5 and N_4 vacancies. The lower energy Auger lines numbered 1-4 in Fig. 13 correspond to the lines in Fig. 6 which were studied above threshold. We assign the resonant Auger lines accordingly, by appending a 6p spectator electron. The assignments are listed in Table IX along with binding energies determined by energy conversion of the TOF spectra. Line number 2 in Fig. 13 appears to correspond to line number 4 in Fig. 6, which we have left unassigned.

The spectrum in Fig. 13 recorded at the $4d^{-1}(^2D_{5/2})6p$ resonance ($h\nu = 65$ eV) corresponds well with the spectrum shown in Ref. 21, where the lines $5s5p^56p$ and $5s^05p^66p$ are identified as they are here. The binding energies listed in Table IX agree well with those obtained from the spectrum in Ref. 21. From the spectra of Eberhardt et al.,[24] Hansen and Persson[25] determined that the effect of the 6p spectator electron is to shift the kinetic energies of the resonant Auger lines $5s^25p^4(SLJ)6p$ to about 4.4 eV higher than observed above threshold for the $5s^25p^4(SLJ)$ multiplets. With the assignments given in Table IX, we measure kinetic energy shifts of between 4.1–4.9 eV for the lower energy Auger lines in comparison with their energies in the absence of a 6p spectator electron.

The resonant Auger lines 2 and 3 in Fig. 13 correspond to the satellite Auger lines observed above threshold and discussed earlier. It is interesting to notice that lines 2 and 3 alternate intensities between the two strong resonances $4d^{-1}(^2D_{5/2})6p$ and $4d^{-1}(^2D_{3/2})6p$. This observation was reproduced in another set of spectra.

The asymmetry parameter for the resonant Auger line $5s5p^5(^1P_1)6p$ was $\beta = 0.85 \pm 0.15$ in the two spectra recorded at 65 eV and 67 eV. This value agrees with those measured for the N_5OO Auger lines at the $4d^{-1}(^2D_{5/2})$ threshold (see Table VII and Fig. 10).

If the intensity scales of the resonant Auger spectra are expanded to bring out weak features, peaks are observed over the kinetic energy region $\epsilon \approx 8$–19 eV (energies $\epsilon < 8$ eV were not recorded in the spectra). The energies and intensities of these weak electron lines indicate that they arise from autoionization of the resonant Auger states identified in Table IX to the levels $5s^25p^4(SLJ)$ of Xe III.

It is clear from the spectra in Fig. 13 that the intensities of the 5p and 5s photolines are relatively unaffected by the 4d $\rightarrow$ 6p resonant excitation but that the Auger final states are strongly populated. These qualitative features of the spectra are further displayed in Fig. 14 where relative partial cross sections are plotted. The cross sections for 5p and 5s photoelectrons stay relatively constant through the resonance region, while the transitions to the $5s^2 5p^4 n\ell$ lines are resonantly enhanced. Off resonance, the $5s^2 5p^4 n\ell$ lines are identified to be the 5s satellites. We measured an off-resonance branching ratio of about 1:1 for the sum of the intensities of the 5s satellites to the intensity of the 5s line. This is in agreement with the relative intensities measured using X-ray photoelectron spectroscopy[46] and the FISCI calculation of Hansen and Persson.[48] The higher resolution electron spectra of Refs. 16, 21, and 24 show that the enhanced intensity of the $5s^2 5p^4 n\ell$ transitions at the 4d $\rightarrow$ 6p resonances is due to the Auger final states rather than the 5s satellites. The intensities of the 5s satellites appear to remain relatively unaffected by autoionization, like the 5s main line.

The effects of the Auger process on resonant photoemission have been studied theoretically.[59,63-65] Though it is not the case here with Xe 4d photoexcitation, it would be of considerable interest to observe resonant Auger transitions which are produced simultaneously by a nonresonant ionization process. In such a case, an asymmetric Fano-type intensity profile would, in general, result due to interference between the resonant and nonresonant transition amplitudes. In the absence of an interference effect, the resonant Auger decay results

in a symmetric Lorentzian profile in the partial cross section. In the present case the total photoabsorption cross section would, in general, display asymmetric profiles at the resonances due to interference structure in the 5p, 5s, and 5s-satellite channels. However, the high resolution photoabsorption spectrum of Ederer and Manalis[20] shows essentially symmetrical Lorentzian lineshapes and with nearly constant linewidths (however, see also Ref. 55). These observations indicate that the resonances decay primarily by the Auger process which is free of an interference effect and that the 5p, 5s, and 5s-satellite decay channels are relatively weak. These expectations are confirmed by the electron spectra in Fig. 13 and the partial cross sections in Fig. 14. It is not surprising that the 4d $\rightarrow$ np resonances decay preferentially by the Auger process, since the Coulomb interaction e/r_{ij} between a pair of O-shell electrons is stronger than that between an O-shell electron and the np Rydberg electron.

Although the partial photoionization cross section for the 5p subshell showed little variation upon resonant excitation, the asymmetry parameter β increased at the resonant energies. This effect was observed from spectra such as in Fig. 13 where the spin-orbit split $5p_{3/2}$ and $5p_{1/2}$ photoelectrons were unresolved. The recent measurements of Codling et al.,[66] for example, made in the region of the Xe $5s5p^{6}6p\ ^{1}P_{1}$ resonance have shown variations between the resonance profiles of $\beta(5p_{3/2})$ and $\beta(5p_{1/2})$ and an oscillation in the $5p_{3/2}:5p_{1/2}$ branching ratio. Theoretical work has shown that resonant variations of partial cross sections, branching ratios, and photoelectron asymmetry and spin-polarization parameters are expected as a general phenomenon.[22,23,60]

These observable parameters characterize the interaction of the resonant states with the continuum channels. Hence, we recorded a series of 0° and 54.7° TOF spectra of the resolved 5p doublet through the energy region of the 4d $\Rightarrow$ np resonances.

An example from the TOF spectra of the 5p doublet is shown in Fig. 15. In the resonance region, the 5p photoelectrons are produced with about 50 eV kinetic energy. The TOF detectors are equipped with simple retarding-grid units which comprise about 60% of the total flight path. A 35 V retarding potential was applied to resolve the 5p doublet. A bandpass of 1.2 Å FWHM (0.4 eV at hν = 65 eV) was used in recording spectra in the resonance region. Collection times of about 4000 sec were required to collect 1000–4000 counts in each peak. To obtain peak areas for determining partial cross sections, branching ratios, and asymmetry parameters, the spectra were fitted to the form of asymmetric Gaussian functions with a linear background. The results are listed in Table X.

The results for the relative partial cross sections are plotted in Fig. 16. Since the photon bandpass used (0.4 eV FWHM) is considerably larger than the widths of the resonances (0.1 eV),[20] any structure in the cross sections would be reduced by averaging with the nonresonant background. Still, a small oscillation in the $5p_{3/2}$ cross section was observed at the most intense resonance, $4d^{-1}(^2D_{5/2})6p$. Very little structure is apparent in the $5p_{1/2}$ measurements.

Though the partial cross sections were relatively insensitive to the resonances, pronounced structure was observed in the β parameters, as shown in Fig. 17. Maxima in the β values occur near the strong

$4d \rightarrow 6p$ excitations, and smaller features appear at the 7p resonances. Also, the measurement at $h\nu = 67.7$ eV indicates that β increases in the energy gap just above the $4d_{5/2}$ ionization threshold and below the $4d_{3/2} \rightarrow 7p$ resonance. This feature is similar to the sustained rise of the β parameters above the $4d_{3/2}$ threshold (see Fig. 3 and Ref. 14). Also plotted in Fig. 17 are the branching ratio measurements. A distinct oscillation was observed near the $4d_{5/2} \rightarrow 6p$ resonance. Krause et al.[14] also measured a dip in the branching ratio near this first strong resonance. Additional structure in the branching ratio at the higher energy resonances is not apparent, probably due in part to cancellation of overlapping structures.

The $4d^{-1}(^2D_{5/2})6p$ excitation is the strongest among the members of the two series and is well separated from the other resonances. The Auger spectrum resulting from decay of this resonance has been studied here and previously.[16,21,24] This resonance produced the only distinct structure in the partial cross sections and branching ratio of the 5p doublet and the most pronounced structure in the asymmetry parameters. Hence, the $4d^{-1}(^2D_{5/2})6p$ resonance seems to be a good example for theoretical studies of inner-shell photoexcitation and autoionization. Kabachnik and Sazhina[23] have derived the form of the photoelectron angular distribution profile for the case of auto-ionization of an isolated resonance. The β profile can be expressed as

$$\beta(\epsilon) = \beta_0 \left[\frac{K_1 + K_2\epsilon + \epsilon^2}{\rho^2(q^2 - 1) + 1 + 2\rho^2 q\epsilon + \epsilon^2} \right] , \qquad (18)$$

where the reduced energy ϵ, the profile index q, and the correlation coefficient ρ are the parameters introduced by Fano and Cooper[59] to describe the total photoabsorption line profile; β_0 is the off-resonance asymmetry parameter, and K_1 and K_2 are constants determined by matrix elements which are characteristic of the resonance and the particular final state. The ϵ, q, and ρ parameters can be taken from the photoabsorption data.[20] Ederer and Manalis found that the 4d → np resonances are nearly Lorentzian, with q $\simeq$ 200 and $\rho^2 \simeq$ 0. Assuming, for simplicity, that $\rho^2(q^2 - 1) \simeq 1$, the denominator in Eq. (18) is reduced to obtain

$$\beta(\epsilon) = \beta_0 \left[\frac{K_1 + K_2\epsilon + \epsilon^2}{2 + \epsilon^2} \right] . \tag{19}$$

We have used Eq. (19) to fit our experimental data for $\beta(5p_{3/2})$ and $\beta(5p_{1/2})$ at the $4d^{-1}(^2D_{5/2})6p$ resonance. To account for the monochromator bandpass, Eq. (19) was convoluted with a triangular function having 1.2 Å FWHM. The fitted values obtained for the parameters K_1 and K_2 in Eq. (19) are: for $5p_{3/2}$, K_1 = 209 ± 10 and K_2 = -83.2 ± 0.4; for $5p_{1/2}$, K_1 = 80.1 ± 0.4 and K_2 = -52.8 ± 0.3.

Cheng and Johnson have used the relativistic random-phase approximation (RRPA) to calculate partial photoionization cross sections, photoelectron asymmetry parameters, and spin-polarization parameters for the Xe $5p_{3/2}$, $5p_{1/2}$, and 5s subshells in the energy region of the $4d_{5/2}$ → 6p resonance.[68] The Auger decay channels were not included in their calculations. In Fig. 18 we compare the present measurements of $\beta(5p_{3/2})$ and $\beta(5p_{1/2})$ with the RRPA theory. Since averaging over the

monochromator bandpass reduces the experimental β values produced at the resonance, we also show the fitted curves obtained using Eq. (19) in which the bandpass function has been deconvoluted. The experimental results confirm that $\beta(5p_{1/2}) > \beta(5p_{3/2})$ as predicted, but note that the experimental β profiles show considerably bigger resonance widths than theory, even after deconvolution of the bandpass.

The discrepancy in the widths is apparently due to the absence of the Auger decay channels in the theoretical calculation. Only the $5p_{3/2}$, $5p_{1/2}$, and 5s decay channels were included in the RRPA calculation, and the calculated widths of the resonances in the partial cross sections are on the order of 0.01 eV. These are much smaller than the observed resonance width (~0.1 eV), which is determined primarily by the Auger decay. However, the calculated widths of the resonance features in the β parameters are 0.1 eV, much larger than the calculated widths for the cross sections. Similarly, deconvolution of the bandpass from the experimental results gives a β profile with a larger width (~0.2 eV) than that observed in the photoabsorption spectrum. This probably explains in part why more distinct structure was experimentally observed in the β parameters than in the cross sections. That is, averaging over the monochromator bandpass had a more severe effect in the case of the cross sections than for the β parameters. However, an additional factor here, which is also related to the widths of the resonance features, is that the β parameter depends on the phases of the photoionization amplitudes as well as the magnitudes. Thus, as noted by Dill,[60] the resonance in β can be more pronounced than in the cross section.

The final set of results are measurements of the angular distribution of Xe 5s photoelectrons through the region of the 4d $\to$ np resonances and just above the 4d ionization threshold. The photoionization process is

$$h\nu + Xe(5s^2 5p^6 \, {}^1S_0) \to Xe^+(5s5p^6 \, {}^2S_{1/2}) + e^-(\epsilon p) \qquad . \tag{20}$$
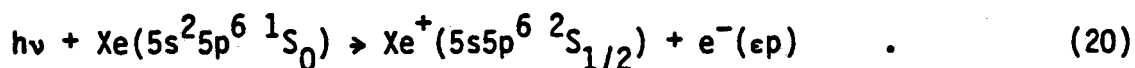
Dehmer and Dill have shown that the analysis of this process is clarified by use of the angular momentum transfer formulation.[69] Angular momentum and parity conservation restrict the photoelectron to a p wave. In a nonrelativistic model the spins of the photoelectron and ionic core remain coupled into a singlet, and an energy-independent asymmetry parameter $\beta = 2$ is predicted. However, the spin-orbit interaction provides a mechanism for reorienting the spins into a triplet. The triplet channel is characterized by an energy-independent asymmetry parameter $\beta = -1$, and the observed asymmetry is a weighted average of the singlet and triplet contributions:

$$\beta_{5s}(\epsilon) = \frac{2\sigma_S(\epsilon) - \sigma_T(\epsilon)}{\sigma_S(\epsilon) + \sigma_T(\epsilon)} \qquad , \tag{21}$$

where $\sigma_S(\epsilon)$ and $\sigma_T(\epsilon)$ are the energy-dependent cross sections for production of singlet and triplet final states, respectively. Thus, values over the entire range $-1 \leq \beta_{5s}(\epsilon) \leq 2$ are possible, and the observed value can be interpreted as a measure of the relative strengths for production of singlet and triplet final states.

Strong deviations of $\beta(5s)$ from the nonrelativistic value 2 have been measured at photon energies near the Cooper minimum.[13,69] A quantitative description of this result is given by the RRPA calculations which include interchannel coupling with the 5p and 4d subshells.[70] The transition strength of the singlet channel passes through a minimum near $h\nu \simeq 35$ eV, so that the triplet contribution becomes relatively stronger. The observable result is that $\beta(5s)$ oscillates through a minimum.

The present measurements of $\beta(5s)$ are listed in Table XI and are plotted in Fig. 19. The measurements were made in an energy region far from the Cooper minimum, and large asymmetries were observed. This result is in good agreement with the RRPA[10,27] and Dirac–Fock (DF)[71] theories, as well as other calculations[72] not plotted in Fig. 19. Torop et al.[12] also measured $1.8 < \beta(5s) \leq 2$ at $h\nu = 83$ eV. Values in the range $\beta(5s) = 1.8-2.0$ indicate a contribution from the triplet channel of less than 7% of the total transition strength.

The RRPA calculation of $\beta(5s)$ plotted in Fig. 19 includes interchannel coupling with the 5p and 4d subshells, but the effects of autoionizing $4d \rightarrow np$ resonances were smoothed over in the results shown. As discussed above, additional RRPA calculations have been made to study the effects of the $4d^{-1}(^2D_{5/2})6p$ excitation on 5p and 5s photoionization.[68] As for the $5p_{3/2}$ and $5p_{1/2}$ subshells, a strong resonant enhancement in the 5s partial cross section is calculated. From an off resonance value of $\beta(5s) \simeq 2$, the calculation obtains a resonant feature $\beta(5s) \rightarrow -1$, indicating that the triplet channel of 5s photoionization couples strongly with the resonant state. However, no

indication of this effect is apparent in the measured $\beta(5s)$ values. The measurements in the resonance region were obtained with a 1.7 Å FWHM bandpass (0.6 eV at $h\nu = 65$ eV), so any resonance structure might be considerably reduced by the nonresonant contribution. It seems, though, that such a strong oscillation, which extends over the entire range of the β parameter, would still have been detected. It is likely that the resonance structure is greatly reduced from that calculated, since the Auger channels dominate the decay of the resonance.

The RRPA calculations, in combination with the multichannel quantum-defect theory, are highly successful in calculating the resonance profiles of photoelectron dynamical parameters for the case of the Beutler-Fano autoionizing resonances of the rare gases.[62] The present case of inner-shell photoexcitation differs from the outer-shell cases in that the resonances decay primarily into the Auger final states.[73] The present measurements of cross sections and β parameters for 5p and 5s photoelectrons indicate that it is important to include the Auger decay channels in theoretical calculations of inner-shell autoionization.

E. Conclusions

Several aspects of inner-shell photoexcitation and ionization of Xe were investigated in these experiments. The oscillatory variation of the $\beta(\epsilon)$ parameter for 4d photoelectrons demonstrates effects of the shape resonance and Cooper minimum in the photoionization process, in good agreement with theory. The present results for the 5p $\beta(\epsilon)$ parameter extend those of previous measurements which confirm that the

(4d,5p) interchannel coupling completely modifies the angular distribution of 5p photoelectrons, particularly above the 4d ionization threshold.

We observed the broadening and shifting of N_5OO Auger electron peaks due to post-collision interaction near the 4d ionization threshold, in good agreement with previous measurements and theory. The $N_{4,5}OO$ Auger electrons are produced with anisotropic angular distributions due to alignment of Xe^+ $(4d^{-1})$ by photoionization. The measured β values of $N_{4,5}OO$ Auger electrons are in good agreement with theoretical calculations. Relatively large Auger electron asymmetries are produced near the 4d ionization threshold as a consequence of the centrifugal barrier in the 4d $\rightarrow \epsilon f$ channel.

As expected, the $4d^{-1}(^2D_{5/2,3/2})np$ resonances were observed to decay primarily by the Auger process. Relatively little structure was observed in the 5p and 5s photoionization cross sections, but pronounced structure was produced in the angular distributions of $5p_{3/2}$ and $5p_{1/2}$ photoelectrons. For the 5s photoelectrons we obtained $\beta \simeq 2$, with no indication of a resonance effect. Comparison of the measurements with theoretical calculations for autoionization of the $4d^{-1}(^2D_{5/2})6p$ resonance indicate the need to include the Auger decay channels in the calculations. However, the measurements were obtained using a monochomator bandpass which is rather large compared with the decay widths of the resonances. In order to compare theory with experiment quantitatively, it is desirable to measure the resonance structure with a smaller bandpass.

94

Acknowledgments

References

1. D. L. Ederer, Phys. Rev. Lett. 13, 760 (1964).

2. A. P. Lukirskii, I. A. Brytov, and T. M. Zimkina, Opt. Spektrosk. 17, 438 (1964) (translation: Opt. Spectrosc. 17, 234 (1964)); A. P. Lukirskii, I. A. Brytov, and S. A. Gribovskii, Opt. Spektrosk. 19, 368 (1965) (translation: Opt. Spectrosc. 20, 203 (1966)).

3. R. Haensel, G. Keitel, P. Schreiber, and C. Kunz, Phys. Rev. 188, 1375 (1969).

4. J. W. Cooper, Phys. Rev. Lett. 13, 762 (1964).

5. S. T. Manson and J. W. Cooper, Phys. Rev. 165, 126 (1968).

6. D. J. Kennedy and S. T. Manson, Phys. Rev. A 5, 227 (1972).

7. M. Ya. Amusia and N. A. Cherepkov, Case Stud. Atom. Phys. 5, 47 (1975).

8. M. Ya. Amusia and V. K. Ivanov, Phys. Lett. A 59, 194 (1976).

9. M. Ya. Amusia, Comments Atom. Mol. Phys. 8, 61 (1979).

10. W. R. Johnson and K. T. Cheng, Phys. Rev. A 20, 978 (1979).

11. J. B. West, P. R. Woodruff, K. Codling, and R. G. Houlgate, J. Phys. B 9, 407 (1976); M. Y. Adam, F. Wuilleumier, N. Sandner, S. Krummacher, V. Schmidt, and W. Mehlhorn, Jap. J. Appl. Phys. 17-2, 170 (1978).

12. L. Torop, J. Morton, and J. B. West, J. Phys. B 9, 2035 (1976).

13. M. G. White, S. H. Southworth, P. Kobrin, E. D. Poliakoff, R. A. Rosenberg, and D. A. Shirley, Phys. Rev. Lett. 43, 1661 (1979) and 44, 620(E) (1980).

14. M. O. Krause, T. A. Carlson, and P. R. Woodruff, Phys. Rev. A 24, 1374 (1981).

15. A. F. Starace, Appl. Opt. 19, 4051 (1980).

16. V. Schmidt, S. Krummacher, F. Wuilleumier, and P. Dhez, Phys. Rev. A 24, 1803 (1981) and references therein.

17. S. Flügge, W. Mehlhorn, and V. Schmidt, Phys. Rev. Lett. 29, 7 (1972).

18. E. G. Berezhko, N. M. Kabachnik, and V. S. Rostovsky, J. Phys. B 11, 1749 (1978).

19. K. Codling and R. P. Madden, Phys. Rev. Lett. 12, 106 (1964).

20. D. L. Ederer and M. Manalis, J. Opt. Soc. Am. 65, 634 (1975).

21. V. Schmidt, Appl. Opt. 19, 4080 (1980). Fig. 10 of this reference shows a photoelectron spectrum of Xe recorded at the $4d^9 5s^2 5p^6 (^2D_{5/2}) 6p$ $^1P_1$ resonance, obtained from N. Sandner, Ph.D. Thesis, Universitat Freiburg (1978) and other unpublished work.

22. A. F. Starace, Phys. Rev. A 16, 231 (1977).

23. N. M. Kabachnik and I. P. Sazhina, J. Phys. B 9, 1681 (1976).

24. W. Eberhardt, G. Kalkoffen, and C. Kunz, Phys. Rev. Lett. 41, 156 (1978). A revised identification of the resonant Auger spectrum of Xe recorded by Eberhardt et al. has been given in Ref. 25.

25. J. E. Hansen and W. Persson, Phys. Rev. A 20, 364 (1979).

26. W. Ong and S. T. Manson, unpublished results.

27. K.-N. Huang, W. R. Johnson, and K. T. Cheng, At. Data Nucl. Data Tables 26, 33 (1981) and unpublished results.

28. J. L. Dehmer, W. A. Chupka, J. Berkowitz, and W. T. Jivery, Phys. Rev. A 12, 1966 (1975).

29. The $\beta(5p)$ values from Refs. 14 and 28 which are plotted in Fig. 3 are weighted averages of $\beta(5p_{3/2})$ and $\beta(5p_{1/2})$, with weights given by the experimental $5p_{3/2}:5p_{1/2}$ branching ratio reported in Ref. 14.

30. W. Ong and S. T. Manson, Phys. Rev. A $\underline{21}$, 842 (1980).

31. L. O. Werme, T. Bergmark, and K. Siegbahn, Phys. Scr. $\underline{6}$, 141 (1972). According to the analysis of Hansen and Persson (Ref. 25), the kinetic energies of the Xe $N_{4,5}OO$ Auger lines reported by Werme et al. should be increased by 0.2 eV to agree with the measurements of Ref. 32.

32. S. Ohtani, H. Nishimura, H. Suzuki, and K. Wakiya, Phys. Rev. Lett. $\underline{36}$, 863 (1976).

33. B. Cleff and W. Mehlhorn, J. Phys. B $\underline{7}$, 593 (1974).

34. E. G. Berezhko and N. M. Kabachnik, J. Phys. B $\underline{10}$, 2467 (1977).

35. E. G. Berezhko, V. K. Ivanov, and N. M. Kabachnik, Phys. Lett. A $\underline{66}$, 474 (1978).

36. W. R. Johnson and V. Radojević, J. Phys. B $\underline{11}$, L773 (1978). We have shifted the theoretical curve to lower photon energy by 4.1 eV to coincide with the experimental ionization threshold rather than the theoretical threshold.

37. S. P. Shannon, K. Codling, and J. B. West, J. Phys. B $\underline{10}$, 825 (1977).

38. M. Y. Adam, F. Wuilleumier, S. Krummacher, N. Sandner, V. Schmidt, and W. Mehlhorn, J. Electron Spectrosc. $\underline{15}$, 211 (1979).

39. M. S. Banna, M. O. Krause, and F. Wuilleumier, J. Phys. B $\underline{12}$, L125 (1979).

40. F. Wuilleumier and M. O. Krause, J. Electron Spectrosc. $\underline{15}$, 15 (1979).

41. J. B. West, P. R. Woodruff, K. Codling, and R. G. Houlgate, J. Phys. B $\underline{9}$, 407 (1976); J. B. West and J. Morton, At. Data Nucl. Data Tables $\underline{22}$, 103 (1978).

42. C. E. Moore, Atomic Energy Levels, Natl. Bur. Stand. (U.S.) Circ. No. 467 (U.S. GPO, Washington, D.C., 1958), Vol. III.

43. W. Mehlhorn, W. Schmitz, and D. Stalherm, Z. Phys. $\underline{252}$, 399 (1972).

44. F. P. Larkins, J. Phys. B $\underline{6}$, 2450 (1973); E. J. McGuire, Phys. Rev. A $\underline{11}$, 17 (1975).

45. F. P. Larkins, At. Data Nucl. Data Tables $\underline{20}$, 311 (1977) and $\underline{23}$, 587(E) (1979).

46. U. Gelius, J. Electron Spectrosc. $\underline{5}$, 985 (1974).

47. M. Y. Adam, F. Wuilleumier, N. Sandner, V. Schmidt, and G. Wendin, J. Phys. (Paris) $\underline{39}$, 129 (1978).

48. J. E. Hansen and W. Persson, Phys. Rev. A $\underline{18}$, 1459 (1978).

49. G. Wendin, Phys. Scr. $\underline{16}$, 296 (1977).

50. S. T. Manson, J. Electron Spectrosc. $\underline{9}$, 21 (1976); D. A. Shirley, J. Phys. (Paris) $\underline{39}$, C4-35 (1978).

51. Excitations of the type $np^2 \rightarrow n'd^2$ have been shown to be significant in describing photoionization of the outer np subshells of the rare gases. See J. R. Swanson and L. Armstrong, Jr., Phys. Rev. A $\underline{15}$, 661 (1977) and $\underline{16}$, 1117 (1977); also, Ref. 15 and references therein.

52. M. G. White, R. A. Rosenberg, G. Gabor, E. D. Poliakoff, G. Thornton, S. H. Southworth, and D. A. Shirley, Rev. Sci. Instrum. $\underline{50}$, 1268 (1979).

53. A. Niehaus, J. Phys. B $\underline{10}$, 1845 (1977).

54. Note that there is a typographical error in Eq. (16) of Ref. 53; a factor of 4 should multiply the δ in the second term.

55. G. C. King, M. Tronc, F. H. Read, and R. C. Bradford, J. Phys. B $\underline{10}$, 2479 (1977).

56. V. Schmidt, N. Sandner, W. Mehlhorn, M. Y. Adam, and F. Wuilleumier, Phys. Rev. Lett. $\underline{38}$, 63 (1977).

57. V. Schmidt, N. Sandner, W. Mehlhorn, F. Wuilleumier, and M. Y. Adam, in Proceedings of the Tenth International Conference on the Physics of Electronic and Atomic Collisions, Paris, 1977 (North-Holland, Amsterdam, 1978), p. 1062.

58. M. Ya. Amusia, Appl. Opt. $\underline{19}$, 4042 (1980) and references therein; T. Åberg, Phys. Scr. $\underline{21}$, 495 (1980).

59. U. Fano, Phys. Rev. $\underline{124}$, 1866 (1961); U. Fano and J. W. Cooper, ibid. $\underline{137}$, A1364 (1965).

60. D. Dill, Phys. Rev. A $\underline{7}$, 1976 (1973).

61. For surveys of the MQDT see U. Fano, J. Opt. Soc. Am. $\underline{65}$, 979 (1975); A. F. Starace, in Photoionization and Other Probes of Many-Electron Interactions, edited by F. J. Wuilleumier (Plenum, New York, 1976), p. 395.

62. For example, W. R. Johnson, K. T. Cheng, K.-N. Huang, and M. Le Dourneuf, Phys. Rev. A $\underline{22}$, 989 (1980).

63. G. Wendin, in Photoionization of Atoms and Molecules, Proceedings of the Daresbury Meeting, edited by B. D. Buckley, Report No. DL/SCI/R11 (1978), p. 1; in Proceedings of the Sixth International Conference on VUV Radiation Physics, Charlottesville, 1980, extended abstracts II-87.

64. Y. Yafet, Phys. Rev. B 21, 5023 (1980) and 23, 3558 (1981).

65. L. C. Davis and L. A. Feldkamp, Phys. Rev. B 23, 6239 (1981).

66. K. Codling, J. B. West, A. C. Parr, J. L. Dehmer, and R. L. Stockbauer, J. Phys. B 13, L693 (1980).

67. F. Wuilleumier, M. Y. Adam, P. Dhez, N. Sandner, V. Schmidt, and W. Mehlhorn, Phys. Rev. A 16, 646 (1977).

68. K. T. Cheng and W. R. Johnson (unpublished).

69. J. L. Dehmer and D. Dill, Phys. Rev. Lett. 37, 1049 (1976).

70. W. R. Johnson and K. T. Cheng, Phys. Rev. Lett. 40, 1167 (1978).

71. W. Ong and S. T. Manson, J. Phys. B 11, L65 (1978); Phys. Rev. A 19, 688 (1979).

72. T. E. H. Walker and J. T. Waber, J. Phys. B 7, 674 (1974); N. A. Cherepkov, Phys. Lett. A 66, 204 (1978); K.-N. Huang and A. F. Starace, Phys. Rev. A 21, 697 (1980).

73. The present measurements indicate that the resonances decay by ∿90% into the Auger channels.

Table I. Photoelectron asymmetry parameters β of the 4d and 5p subshells of Xe.

hν (eV)	β(4d)	β(5p)	hν (eV)	β(4d)	β(5p)
71.8	1.56(4)	. . .	145.	. . .	1.20(19)
72.8	1.28(4)	0.37(4)	147.	1.74(6)	. . .
73.7	1.00(3)	0.47(6)	152.	1.81(9)	. . .
74.7	0.82(4)	0.65(7)	155	. . .	0.78(18)
75.6	0.67(3)	0.69(5)	157.	1.65(10)	. . .
78.0	0.42(3)	0.84(8)	161.	1.48(9)	. . .
80.4	0.26(3)	0.91(8)	164	. . .	0.45(13)
83.2	0.13(2)	0.92(9)	166.	1.13(8)	. . .
85.1	0.15(2)	. . .	171.	0.76(8)	0.39(14)
87.0	0.10(2)	1.27(11)	175.	0.40(5)	0.45(13)
88.9	0.17(3)	1.52(13)	178.	0.09(9)	. . .
94.6	0.11(3)	1.65(19)	180.	−0.15(4)	0.38(12)
99.3	0.38(2)	1.71(18)	185.	−0.35(3)	0.47(13)
104.	0.42(2)	1.55(14)	190.	−0.50(2)	0.43(13)
113.	0.80(3)	1.66(20)	199.	−0.55(10)	. . .
124.	1.07(9)	. . .	208.	−0.58(9)	. . .
126.	. . .	1.66(20)	227.	−0.44(11)	. . .
128.	1.27(6)	. . .	248.	0.09(15)	. . .
133.	1.50(6)	. . .	257.	0.2(2)	. . .
135.	. . .	1.44(17)	271.	0.4(2)	. . .
137.	1.57(7)	. . .	333.	0.8(5)	. . .
142.	1.71(7)	. . .			

Table II. Hartree-Fock calculations of Kennedy and Manson[6] for the partial-wave branching ratio γ for photoionization of the Xe 4d subshell as a function of photoelectron energy ϵ. Also listed are the resulting theoretical values for the alignment tensor A_{20} of Xe^+ $^2D_{5/2}$ and the asymmetry parameter β for an Auger transition of the type N_5OO $^1S_0$. Results are given for both the length and velocity forms of the dipole operator.

$\epsilon(Ry)$	HF-L			HF-V		
	γ	A_{20}	β	γ	A_{20}	β
0.00	1.467+1	0.357	0.764	1.843+1	0.360	0.771
0.05	7.769	0.344	0.735	9.806	0.349	0.747
0.10	4.677	0.327	0.699	5.927	0.336	0.718
0.20	2.083	0.288	0.615	2.665	0.301	0.644
0.40	6.352-1	0.211	0.451	8.241-1	0.228	0.487
0.60	2.665-1	0.163	0.349	3.508-1	0.176	0.377
0.80	1.406-1	0.140	0.299	1.873-1	0.149	0.319
1.00	8.940-2	0.129	0.275	1.203-1	0.136	0.290
1.25	6.128-2	0.122	0.262	8.348-2	0.128	0.273
1.50	4.768-2	0.119	0.255	6.575-2	0.123	0.264
1.75	3.962-2	0.117	0.250	5.525-2	0.121	0.258
2.00	3.412-2	0.116	0.247	4.812-2	0.119	0.255
2.50	2.725-2	0.114	0.244	3.933-2	0.117	0.250
3.00	2.401-2	0.113	0.242	3.556-2	0.116	0.248
3.50	2.359-2	0.113	0.242	3.599-2	0.116	0.248
4.00	2.563-2	0.114	0.243	4.053-2	0.117	0.251
6.00	7.205-2	0.125	0.267	1.454-1	0.141	0.301
8.00	4.312-1	0.187	0.401	2.071	0.287	0.614
10.00	5.081+1	0.369	0.789	3.972	0.320	0.685
15.00	3.331-1	0.174	0.371	2.263-1	0.156	0.334
20.00	1.390-1	0.140	0.298	1.176-1	0.135	0.289
25.00	9.279-2	0.130	0.277	8.406-2	0.128	0.273
30.00	7.241-2	0.125	0.267	6.829-2	0.124	0.265

Table III. Asymmetry parameters β for Xe N_5OO Auger electrons.

hν (eV)	$N_5O_1O_{2,3}$ $^1P_1$	$N_5O_1O_1$ $^1S_0$
68.1	0.49(10)	0.67(9)
69.9	0.31(9)	0.45(8)
71.3	0.26(5)	0.35(6)
72.8	0.15(5)	0.31(5)
74.2	0.09(4)	0.33(7)
75.6	0.11(6)	. . .
78.0	0.13(8)	. . .
80.4	0.09(8)	0.33(10)
83.2	0.08(9)	0.35(8)
88.0	. . .	0.36(8)
99.3	0.10(11)	0.25(12)
104.	0.11(8)	0.39(12)
113.	0.15(13)	0.29(10)
124.	0.12(18)	. . .
128.	0.01(15)	0.14(15)
133.	0.04(17)	0.27(16)
143.	−0.10(9)	0.19(12)
155.	0.1(3)	0.5(3)
164.	0.3(4)	. . .
167.	. . .	0.4(2)
174.	0.6(4)	. . .
178.	. . .	0.4(2)
183.	1.0(4)	. . .
187.	. . .	0.5(2)
190.	0.5(4)	. . .

Table IV. Average of the Xe Auger electron branching ratios $N_5O_1O_1:N_4O_1O_1$ ($^1S_0$) and $N_5O_1O_{2,3}:N_4O_1O_{2,3}$ ($^1P_1$).

hν (eV)	$N_5OO:N_4OO$
69.9	2.36(9)
72.8	2.35(6)
74.7	2.22(18)
75.6	1.72(9)
78.0	1.38(9)
80.4	1.30(9)
83.2	1.30(7)
85.1	1.24(11)
87.0	1.28(11)
88.9	1.15(10)
94.6	1.37(14)
99.3	1.32(10)
104.	1.39(6)
113.	1.16(8)
128.	1.43(16)
133.	1.12(11)
138.	1.39(12)
143.	1.18(13)
147.	1.20(20)
155.	0.96(14)
162.	1.09(18)

Table V. Identification of the Xe $N_{4,5}OO$ Auger lines indicated in Fig. 6. The kinetic energies are those reported by Werme et al., but increased by 0.2 eV due to a correction in calibration data (see Ref. 31). For comparison, the kinetic energies given by energy-conversion of the present TOF spectrum are also listed.

Line no.	Initial vacancy	Final state	Kinetic energy (eV)	
			Werme et al.	TOF
1	N_4	$5s5p^5\ ^1P_1$	21.64 (5)	21.76 (5)
2	N_5	$5s5p^5\ ^1P_1$	19.65 (3)	19.72 (5)
3	N_4	$5s^25p^3(^2P)5d\ ^1P_1$	16.12 (5)	16.12 (5)
4	N_5	· · ·	15.25 (6)	15.17 (5)
5	N_5	$5s^25p^3(^2P)5d\ ^1P_1$	14.15 (7)	14.09 (5)
6	N_4	$5s^05p^6\ ^1S_0$	10.27 (7)	10.22 (5)
7	N_5	$5s^05p^6\ ^1S_0$	8.28 (7)	8.24 (5)

Table VI. The relative shift $\Delta\epsilon$ of the Xe $N_5O_1O_1$ $^1S_0$ Auger peak with respect to its position at $h\nu = 81.9$ eV, as a function of the energy E of the $4d_{5/2}$ photoelectrons. Uncertainties in E represent one standard deviation which results for a monochromator bandpass of 2.6 Å FWHM.

E (eV)	$\Delta\epsilon$ (meV)
0.1 (4)	240 (30)
1.2 (4)	120 (30)
2.2 (4)	90 (30)
3.2 (4)	50 (30)
4.0 (5)	50 (30)
5.3 (5)	30 (20)
6.3 (5)	20 (20)

Table VII. Asymmetry parameters β for Xe $N_{4,5}OO$ Auger electrons. The Auger lines are identified in Table V.

hν (eV)	Line Number						
	1	2	3	4	5	6	7
67.7	. . .	0.77 (13)	. . .	0.84 (18)	0.92 (14)	. . .	0.84 (12)
68.7	. . .	0.82 (13)	. . .	0.77 (20)	0.78 (13)	. . .	0.92 (13)
69.7	0.69 (14)	0.62 (9)	0.61 (14)	0.67 (11)	0.68 (10)	0.82 (14)	0.69 (10)
70.8	0.63 (13)	0.56 (9)	0.55 (11)	0.48 (9)	0.59 (9)	0.71 (13)	0.49 (8)
71.6	0.69 (15)	0.55 (9)	0.47 (13)	0.59 (11)	0.60 (10)	0.64 (13)	0.58 (9)
72.8	0.45 (13)	0.51 (9)	0.35 (12)	0.53 (10)	0.56 (9)	0.61 (12)	0.51 (9)
73.9	0.50 (13)	0.36 (8)	0.46 (11)	0.38 (9)	0.40 (8)	0.34 (10)	0.48 (8)
75.9	0.16 (8)	0.15 (6)	0.17 (8)	0.14 (7)	0.11 (6)	0.17 (7)	. . .
76.7	0.16 (9)	0.20 (8)	0.11 (8)	0.12 (9)	0.10 (7)	. . .	. . .
81.9	0.13 (7)	0.22 (7)	0.24 (8)	. . .	. . .	0.20 (7)	0.29 (7)

Table VIII. Xe $N_5OO:N_4OO$ Auger electron branching ratios measured for three final states.

$h\nu$ (eV)	$5s5p^5\ ^1P_1$	$5s^2 5p^3 (^2P) 5d\ ^1P_1$	$5s^0 5p^6\ ^1S_0$
69.7	1.99 (11)	1.75 (10)	2.20 (13)
70.8	2.03 (11)	2.10 (11)	2.71 (15)
71.6	2.10 (14)	2.25 (14)	2.84 (18)
72.8	2.31 (15)	2.11 (13)	2.50 (14)
73.9	2.29 (14)	2.42 (13)	2.08 (11)
75.9	1.81 (8)	1.87 (8)	...
76.7	1.53 (9)	1.44 (7)	...
81.9	1.21 (5)	...	1.24 (5)

Table IX.   Identification of the resonant Auger lines of Xe indicated in Fig. 13.

Line number	Final state	Binding energy (eV)
1	$5s5p^5(^1P_1)6p$	40.9 (2)
2	...	45.8 (3)
3	$5s^2 5p^3(^2P)5d(^1P_1)6p$	46.1 (3)
4	$5s^0 5p^6(^1S_0)6p$	52.1 (2)

Table X. The asymmetry parameters β, relative partial photoionization cross sections σ, and branching ratio for Xe $5p_{3/2}$ and $5p_{1/2}$ photoelectrons, measured through the 4d → np resonances. The monochromator bandpass (FWHM) was 2.6 Å at the two lowest photon energies, 1.2 Å in the resonance energy region, and 1.7 Å for the two highest photon energies.

hν (eV)	$\sigma(5p_{3/2})$	$\sigma(5p_{1/2})$	$\sigma(5p_{3/2}):\sigma(5p_{1/2})$	$\beta(5p_{3/2})$	$\beta(5p_{1/2})$
59.3	...	...	1.91 (7)	0.22 (4)	0.33 (5)
61.3	...	...	2.05 (7)	0.12 (3)	0.24 (4)
63.37	...	...	1.98 (8)	0.07 (5)	0.19 (7)
63.88	6.62 (23)	3.39 (14)	1.95 (7)	...	0.18 (6)
64.39	7.47 (24)	3.70 (13)	2.02 (5)	0.11 (4)	0.24 (5)
64.70	7.80 (25)	3.59 (13)	2.17 (6)	0.17 (4)	0.37 (6)
65.11	7.25 (27)	3.89 (16)	1.86 (7)	0.38 (6)	0.53 (8)
65.42	6.92 (22)	3.90 (13)	1.77 (5)	0.13 (3)	0.25 (5)
65.83	7.60 (25)	4.09 (15)	1.86 (6)	0.04 (4)	0.07 (5)
66.14	8.31 (28)	4.42 (16)	1.88 (6)	0.11 (4)	0.13 (5)
66.45	7.92 (25)	4.22 (14)	1.88 (4)	0.11 (3)	0.20 (4)
66.65	...	...	1.84 (4)	0.09 (3)	0.18 (4)
67.06	8.43 (27)	4.48 (16)	1.88 (5)	0.26 (4)	0.33 (5)
67.48	8.59 (27)	4.54 (16)	1.89 (5)	0.09 (3)	0.16 (4)
67.73	8.49 (26)	4.52 (15)	1.88 (4)	0.14 (3)	0.30 (4)
68.30	8.69 (27)	4.55 (16)	1.91 (5)	0.12 (3)	0.25 (5)
69.0	...	...	2.01 (7)	0.03 (3)	0.10 (3)
70.0	...	...	1.96 (6)	0.07 (2)	0.12 (3)

Table XI. Asymmetry parameters β of Xe 5s photoelectrons. The measurements between hν = 62.3–68.5 eV were made with a monochromator bandpass of 1.7 Å FWHM. At higher energies the bandpass was 5.3Å FWHM.

hν (eV)	β(5s)
62.3	1.87 (11)
63.4	1.84 (12)
64.7	1.90 (20)
65.0	1.81 (9)
65.3	1.88 (11)
65.7	1.82 (16)
66.3	2.00 (16)
67.0	1.84 (8)
67.5	1.91 (13)
68.5	1.95 (16)
68.9	1.78 (12)
69.9	1.99 (13)
70.9	1.98 (13)
71.8	2.00 (13)
72.8	1.84 (9)
73.7	1.76 (12)
74.7	2.00 (15)
75.6	1.91 (10)
78.0	1.91 (14)
80.4	1.88 (14)

Figure Captions

Fig. 1. Time-of-flight electron spectra from photoionization of Xe by 70.9 eV photons, at $\theta = 0°$ and $\theta = 54.7°$ relative to the polarization direction. The peak at TOF $\simeq$ 55 nsec is due to 4d photoelectrons produced by second-order light ($h\nu = 141.8$ eV).

Fig. 2. Measured values of the Xe 4d photoelectron asymmetry parameter β, compared with the data (X) of Ref. 12 and with theoretical curves: Hartree-Fock length (HF-L) and velocity (HF-V) calculations, Ref. 6; Dirac-Fock (DF), Ref. 26; relativistic random-phase approximation (RRPA), Ref. 27.

Fig. 3. Experimental and theoretical values of the Xe 5p photoelectron asymmetry parameter. Measurements: $\bullet$, Ref. 28; $\square$, Ref. 14; $\triangle$, Ref. 12; $\bigcirc$, present results (see Ref. 29). Theory (Ref. 8): random-phase approximation with exchange (RPAE) calculations which include (full curve) and do not include (dashed curve) interchannel coupling with the 4d subshell.

Fig. 4. Auger electron asymmetry parameters for the transitions Xe $N_5O_1O_1\ ^1S_0$ (open circles) and $N_5O_1O_{2,3}\ ^1P_1$ (closed circles). The theoretical curves (see text for references) are for a transition of the general type $N_5OO\ ^1S_0$. Dashed curve: Hartree-Fock length; full curve: Hartree-Fock velocity. The energy of the preceding $4d_{5/2}$ photoelectron is also shown.

Fig. 5. Xe $N_5OO:N_4OO$ Auger electron branching ratio compared with the $4d_{5/2}:4d_{3/2}$ photoelectron branching ratio. ●, Average of the Auger electron branching ratios

$N_5O_1O_1:N_4O_1O_1$ ($^1S_0$) and $N_5O_1O_{2,3}:N_4O_1O_{2,3}$ ($^1P_1$).

Experimental data for the $4d_{5/2}:4d_{3/2}$ photoelectron branching ratio: △, Ref. 37; ○, Ref. 38; □, Ref. 39. The theoretical curve is from the RRPA calculation, Ref. 36.

Fig. 6. Time-of-flight spectra of Xe $N_{4,5}OO$ Auger electrons produced by photoionization, at $0°$ and $54.7°$ relative to the polarization direction. A nonlinear energy scale is also given. The numbered lines are identified in Table V.

Fig. 7. The $54.7°$ time-of-flight spectrum of Xe Auger electrons recorded at a photon energy in between the $4d_{5/2}$ and $4d_{3/2}$ ionization thresholds. Only the N_5OO Auger lines were produced. The numbered peaks are identified in Table V.

Fig. 8. The Xe $N_5O_1O_1$ $^1S_0$ Auger line recorded at photon energies which lie 0.1 eV above the $4d_{5/2}$ ionization threshold (top) and at 14.4 eV above threshold (bottom). The shifting and broadening of the Auger line recorded near the ionization threshold are attributed to post-collision interaction.

Fig. 9. The energy shift of the Xe N_5OO Auger lines as a function

of the $4d_{5/2}$ photoelectron energy. The theoretical curve

is that derived in Ref. 53 for an N_5-hole decay width of

110 meV. The curve is appropriate for both the absolute

shifts ϵ plotted using the present measurements and for the

relative shifts $\Delta\epsilon$ of Ref. 16 which are corrected for the

spectrometer function (see discussion in text). ●, Present

measurements for the $N_5O_1O_1$ $^1S_0$ line. Measurements for the

$N_5O_{2,3}O_{2,3}$ $^1S_0$ line: O, Ref. 16; △, Ref. 56; □, Ref. 57.

Fig. 10. Asymmetry parameters for Xe $N_{4,5}OO$ Auger electrons. Each

panel gives measurements for both the N_5- (closed circles)

and N_4- (open circles) transitions which have the given

final state. The same theoretical curve, based on Hartree-

Fock calculations (see text for references), is plotted in

all three panels, but is appropriate for transitions of the

general type $N_{4,5}OO$ $^1S_0$. The two arrows mark the positions

of the N_5 and N_4 ionization thresholds.

Fig. 11. Xe $N_5OO:N_4OO$ Auger electron branching ratios compared with

the $4d_{5/2}:4d_{3/2}$ photoelectron branching ratio. Present

measurements of the Auger electron ratios: ●, $5s^0 5p^6$ $^1S_0$;

▲, $5s^2 5p^3(^2P)5d$ $^1P_1$. Measurements of the photoelectron

ratio: O, Ref. 38; □, Ref. 37. The theoretical curve

(Ref. 36) is the RRPA calculation for the photoelectron

branching ratio. The arrow marks the position of the N_4

ionization threshold.

Fig. 12. Photoelectron excitation spectrum of Xe recorded through the 4d $\rightarrow$ np resonances (see text for discussion). The positions of the resonances and the ionization thresholds are those reported by Codling and Madden.[19]

Fig. 13. Time-of-flight electron spectra of Xe recorded off resonance (at hν = 63.4 eV and 65.8 eV) and at the resonances $4d^{-1}(^2D_{5/2})6p$ (65.0 eV) and $4d^{-1}(^2D_{3/2})6p$ (67.0 eV). The peaks numbered 1-4 are identified in Table IX. A nonlinear kinetic energy scale is also given.

Fig. 14. Relative partial photoionization cross sections for Xe 5p and 5s photoelectrons and for the group of electron peaks in Fig. 13 labeled $5s^2 5p^4 n\ell$. A line is drawn through the open circles to accent the resonant enhancement. The positions of the 4d $\rightarrow$ 6p resonances are indicated.

Fig. 15. 0° and 54.7° time-of-flight photoelectron spectra of the Xe 5p doublet recorded at hν = 65.1 eV.

Fig. 16. Relative partial cross sections for the Xe $5p_{3/2}$ and $5p_{1/2}$ subshells in the energy region of the $4d^{-1}(^2D_{5/2,3/2})np$ resonances.

Fig. 17. Asymmetry parameters for Xe $5p_{3/2}$ and $5p_{1/2}$ photoelectrons and the $5p_{3/2}:5p_{1/2}$ branching ratio measured through the $4d^{-1}(^2D_{5/2,3/2})np$ resonances. Only representative error bars are shown, and lines have been drawn through the data to indicate the resonance variations. Asymmetry parameters for $5p_{1/2}$ and $5p_{3/2}$ are denoted with open and closed symbols, respectively: circles, this work; squares, Ref. 14. Branching ratio: circles, this work; squares, Ref. 14; triangles, Ref. 67.

Fig. 18. Comparison of experiment and theory for the asymmetry parameters of Xe $5p_{3/2}$ and $5p_{1/2}$ photoelectrons produced at the $4d^{-1}(^2D_{5/2})6p$ resonance. The solid curves are the RRPA theoretical calculations (Ref. 68). The dashed curves are fits of the experimental data to the form of Eq. (19) for the resonance profiles, including convolution with the monochromator bandpass (0.4 eV FWHM). The dot-dashed curves are the fitted resonance profiles of Eq. (19) after deconvolution of the bandpass.

Fig. 19. Asymmetry parameter of Xe 5s photoelectrons compared with the DF (Ref. 71) and RRPA (Refs. 10 and 27) theoretical curves. Only a representative error bar is shown. The positions of the $4d^{-1}(^2D_{5/2,3/2})np$ resonances are indicated.

Figure 1

XBL 808-11201

Figure 2

XBL 8012-12852

Xe 5p

asymmetry parameter, β
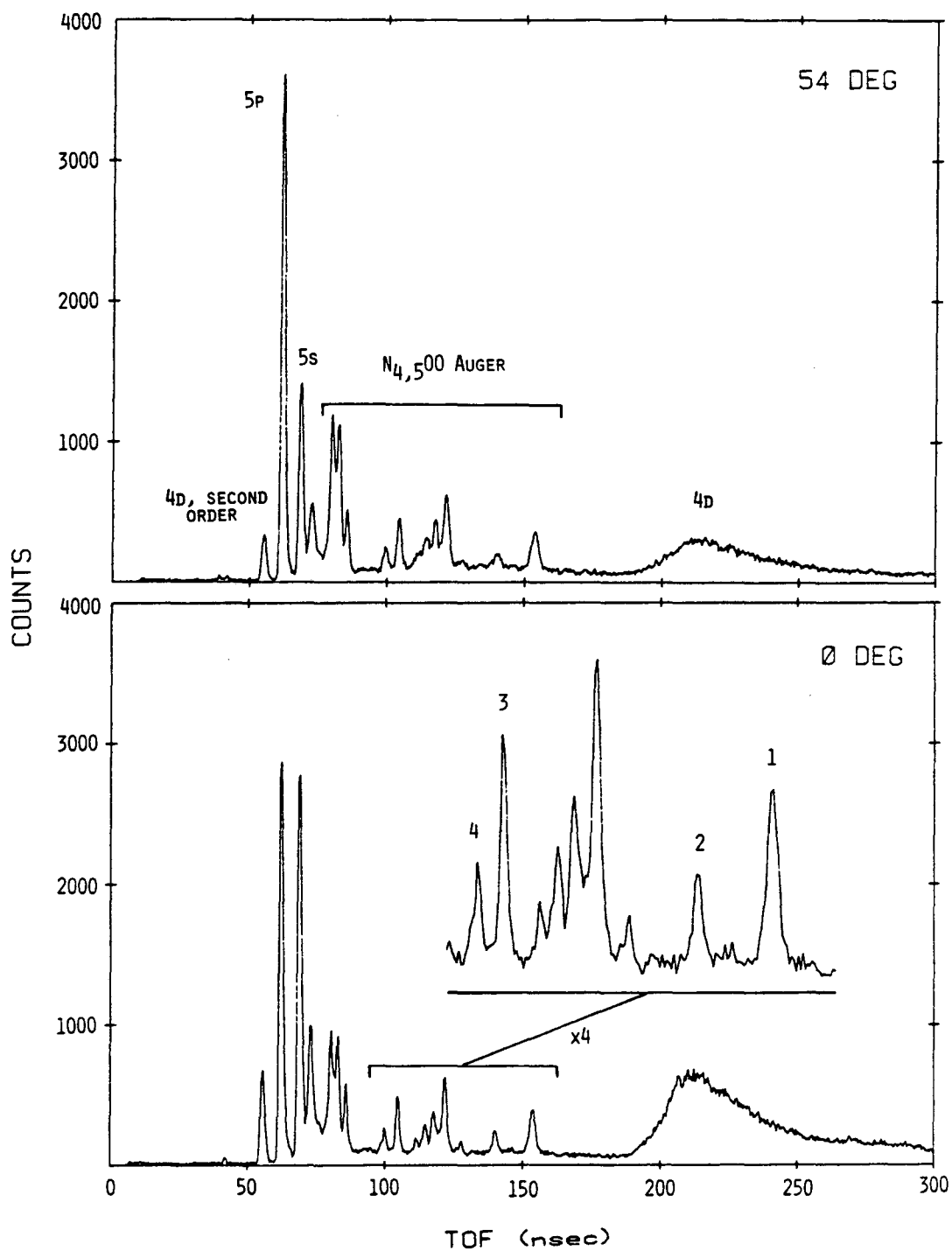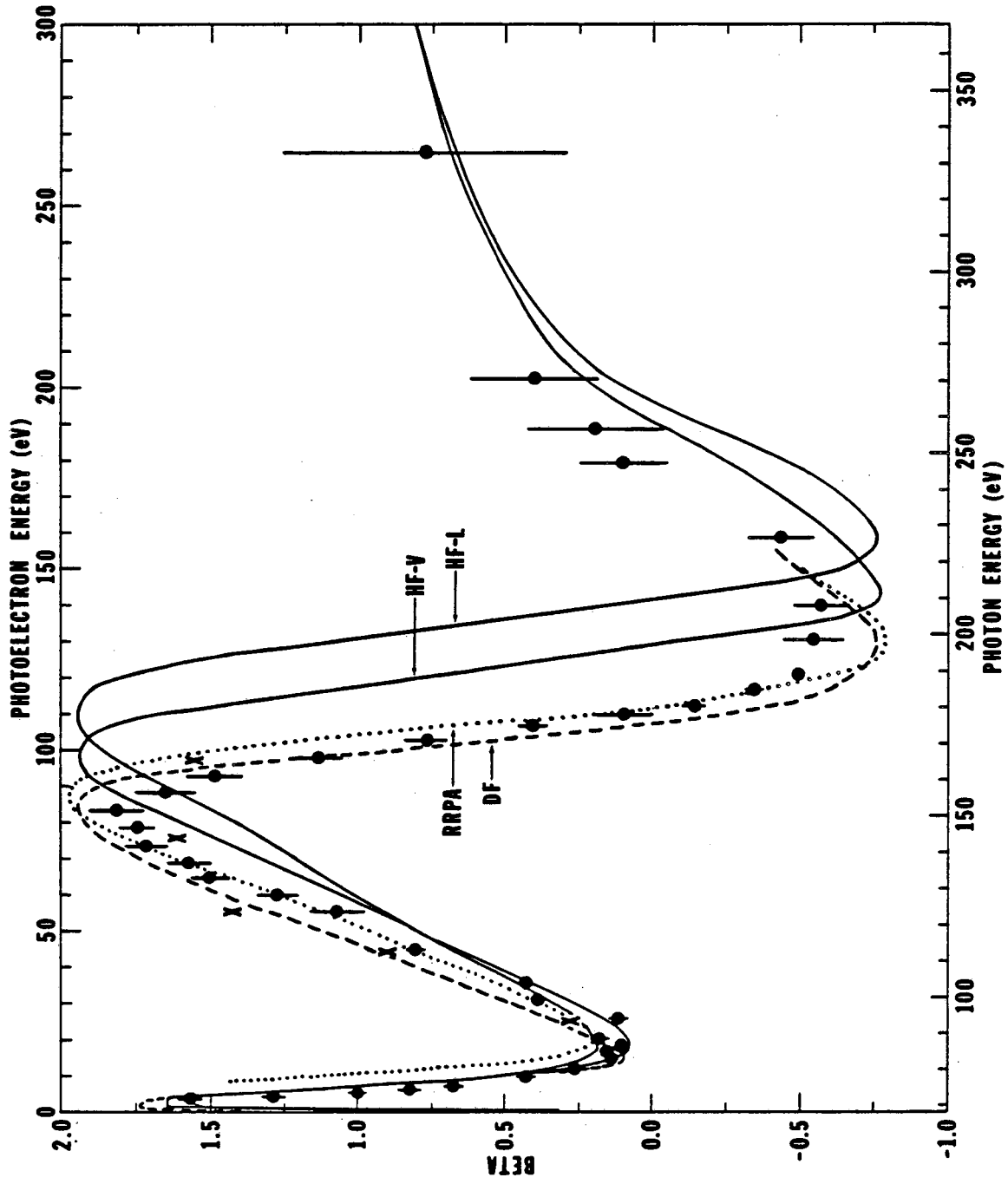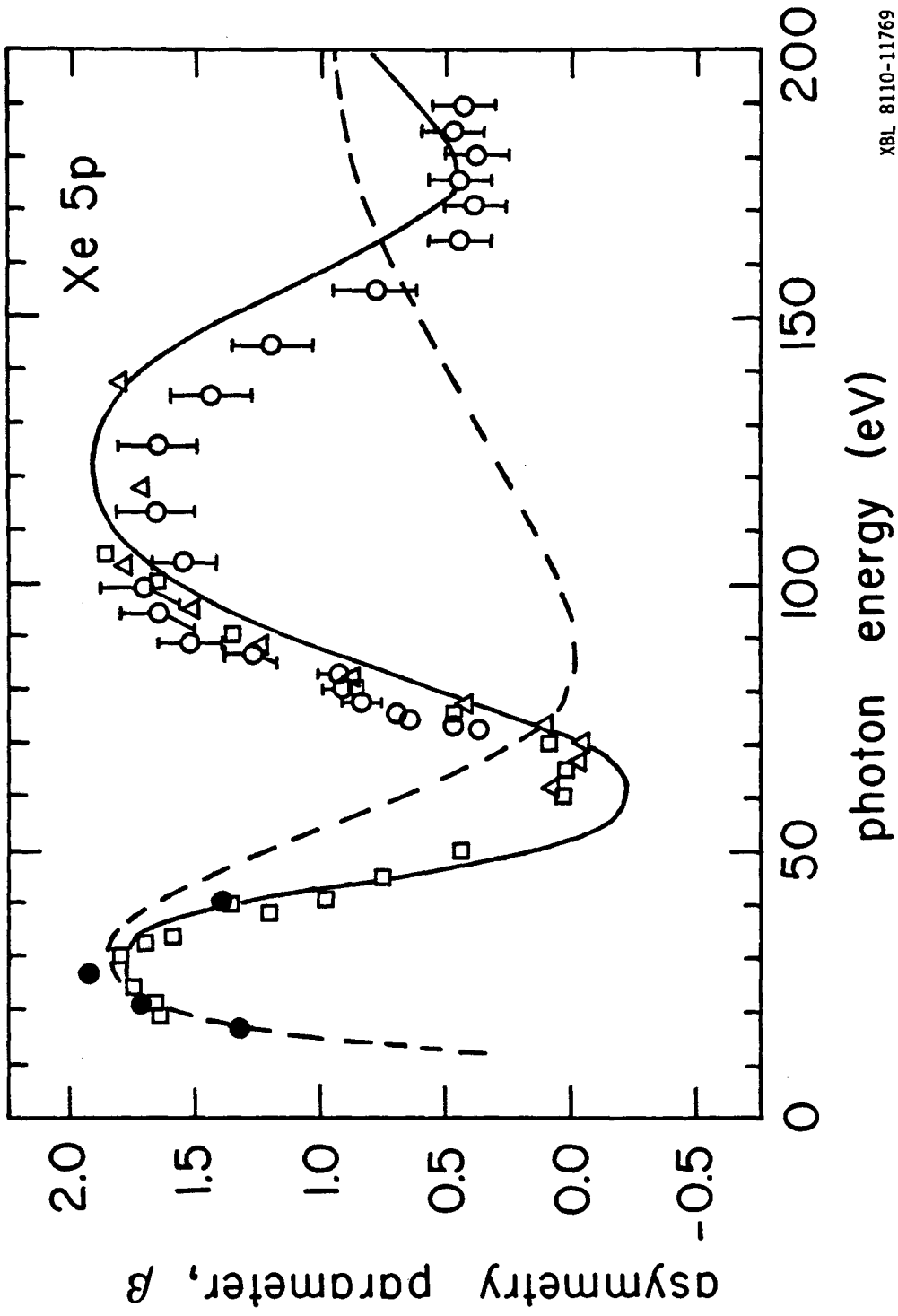
photon energy (eV)

XBL 8110-11769
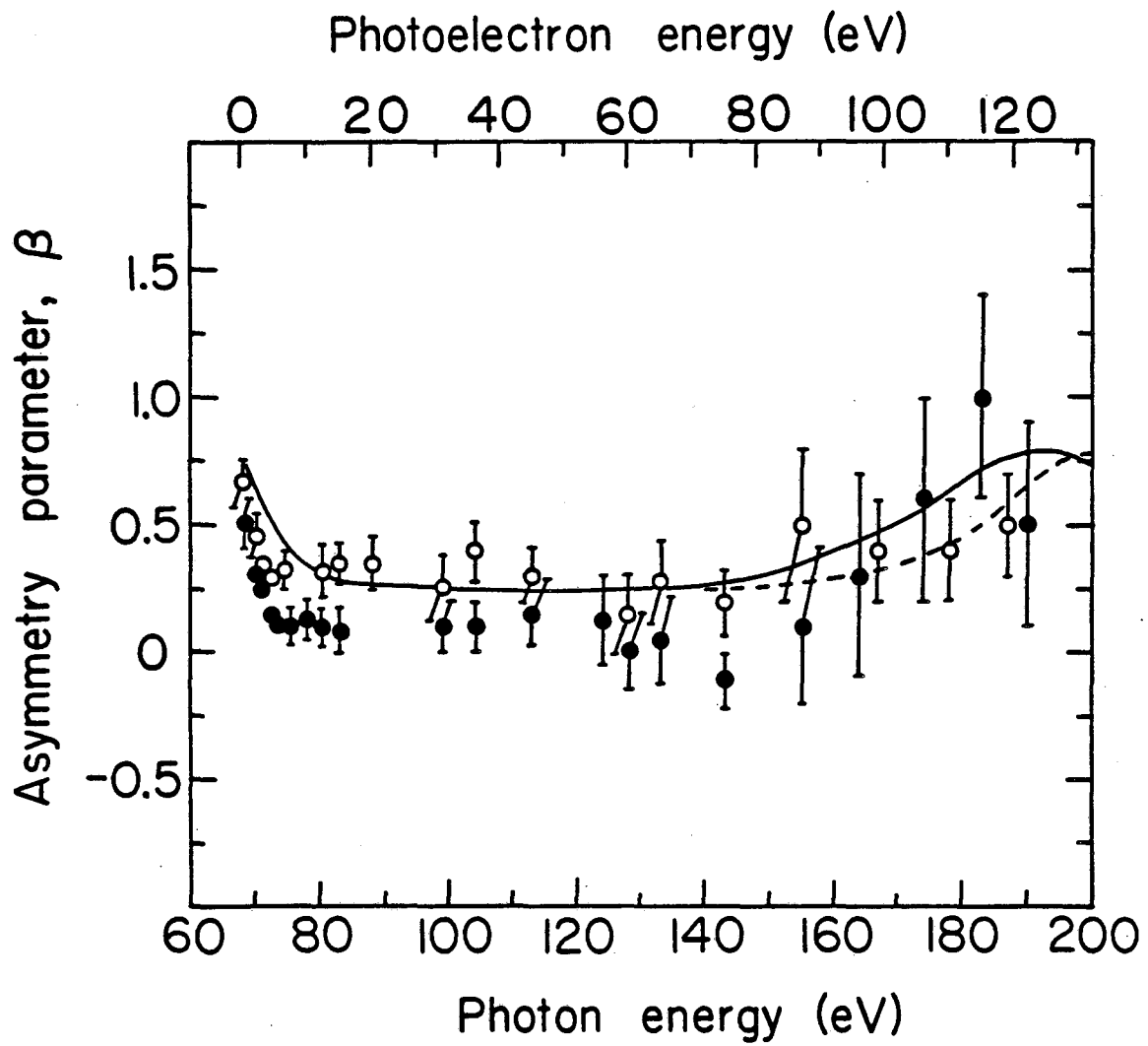
Figure 3

Figure 4

XBL 821-7561
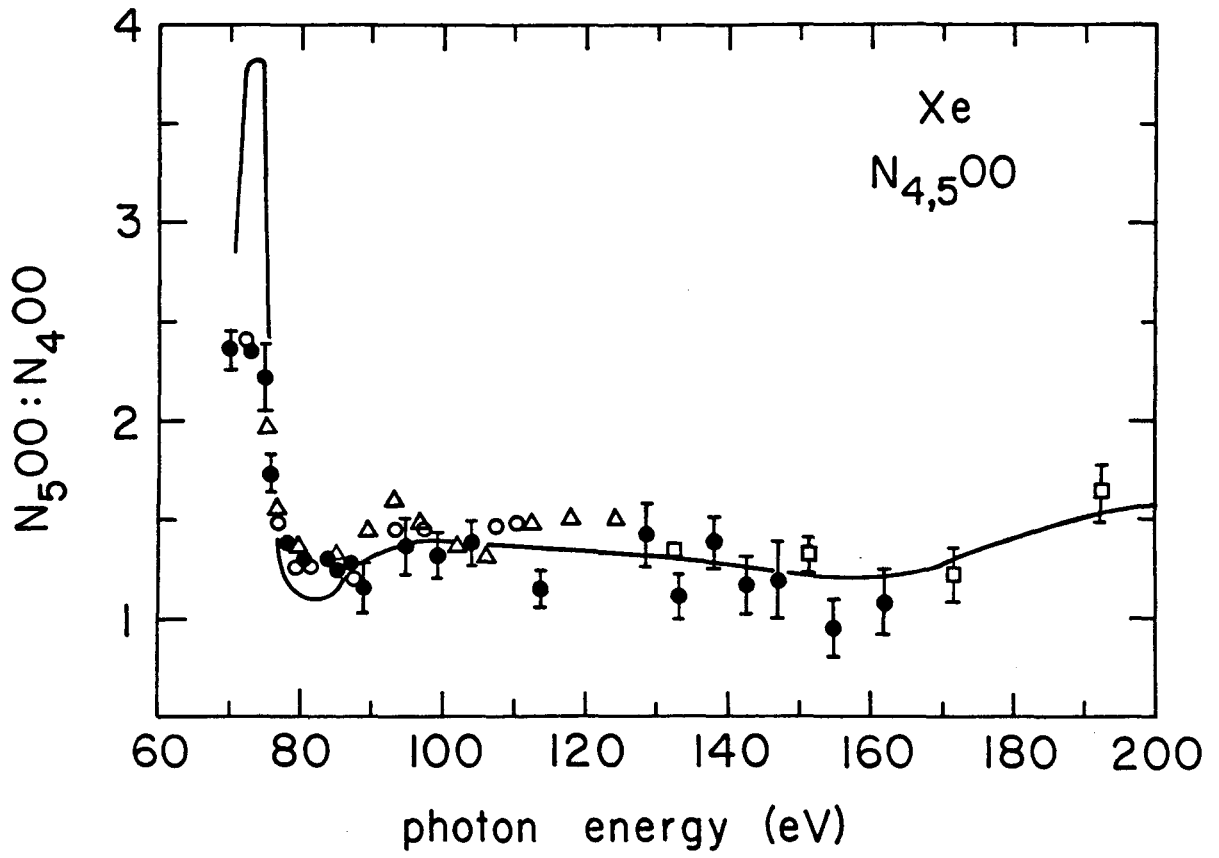
Figure 5

XBL 8110-11772
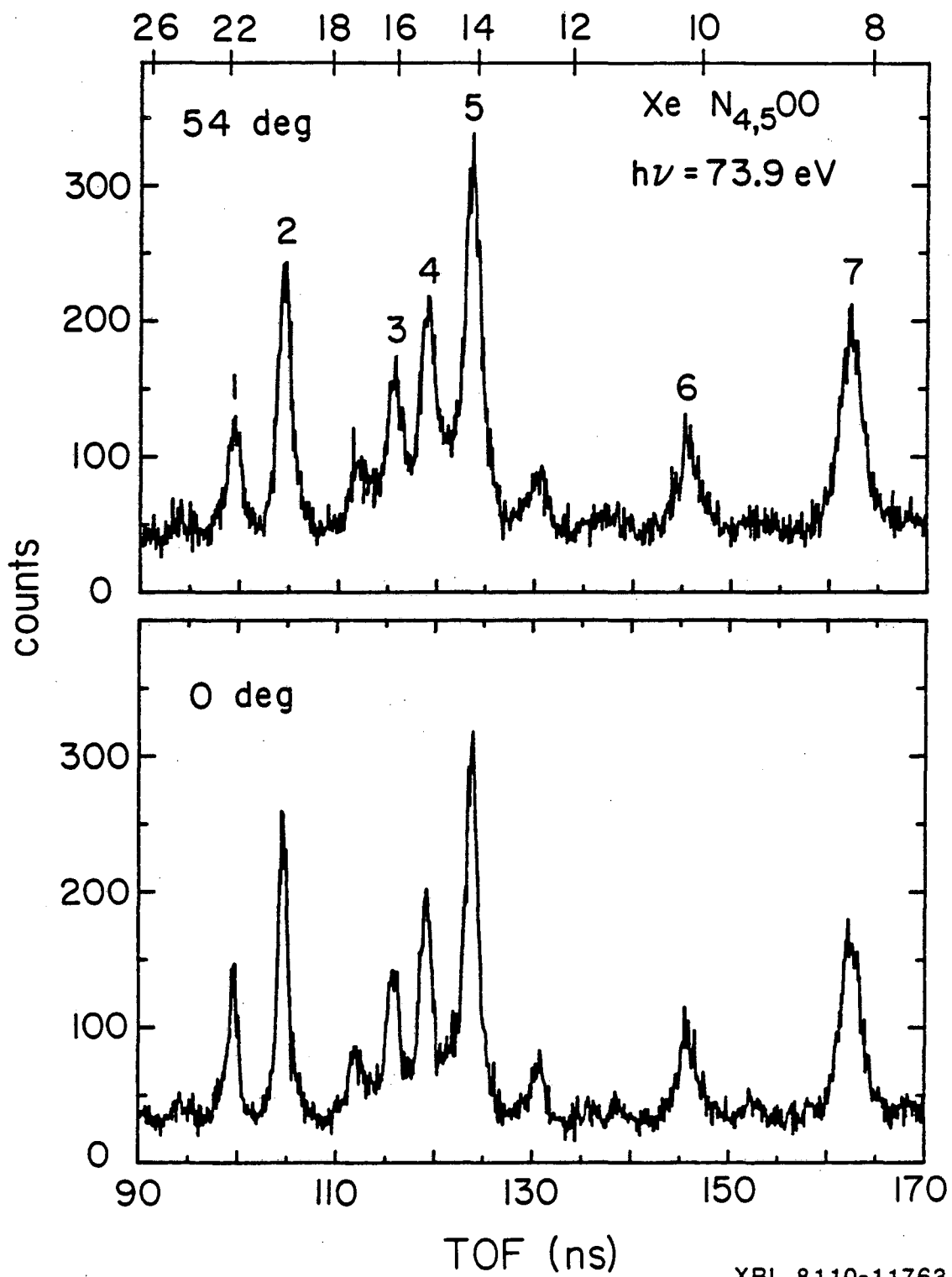
Figure 6

XBL 8110-11763
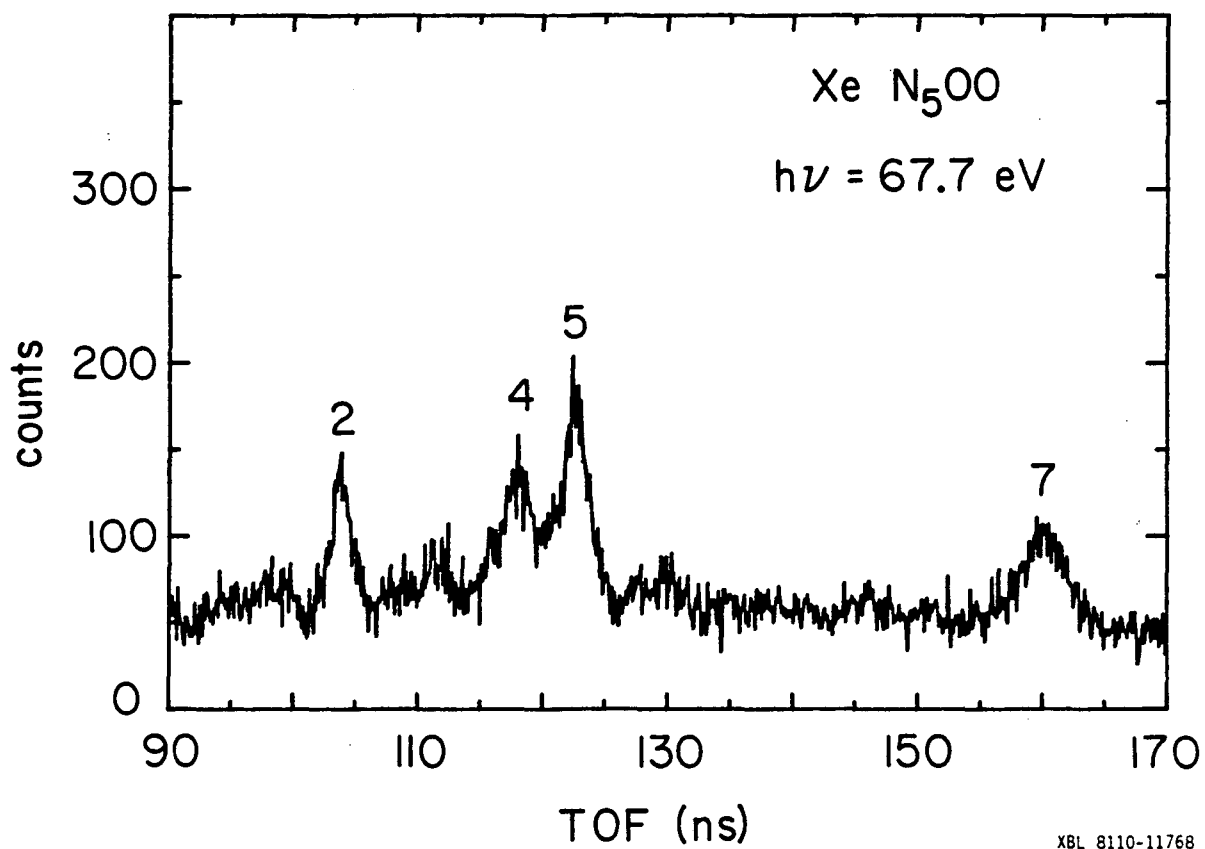
Figure 7

XBL 8110-11768
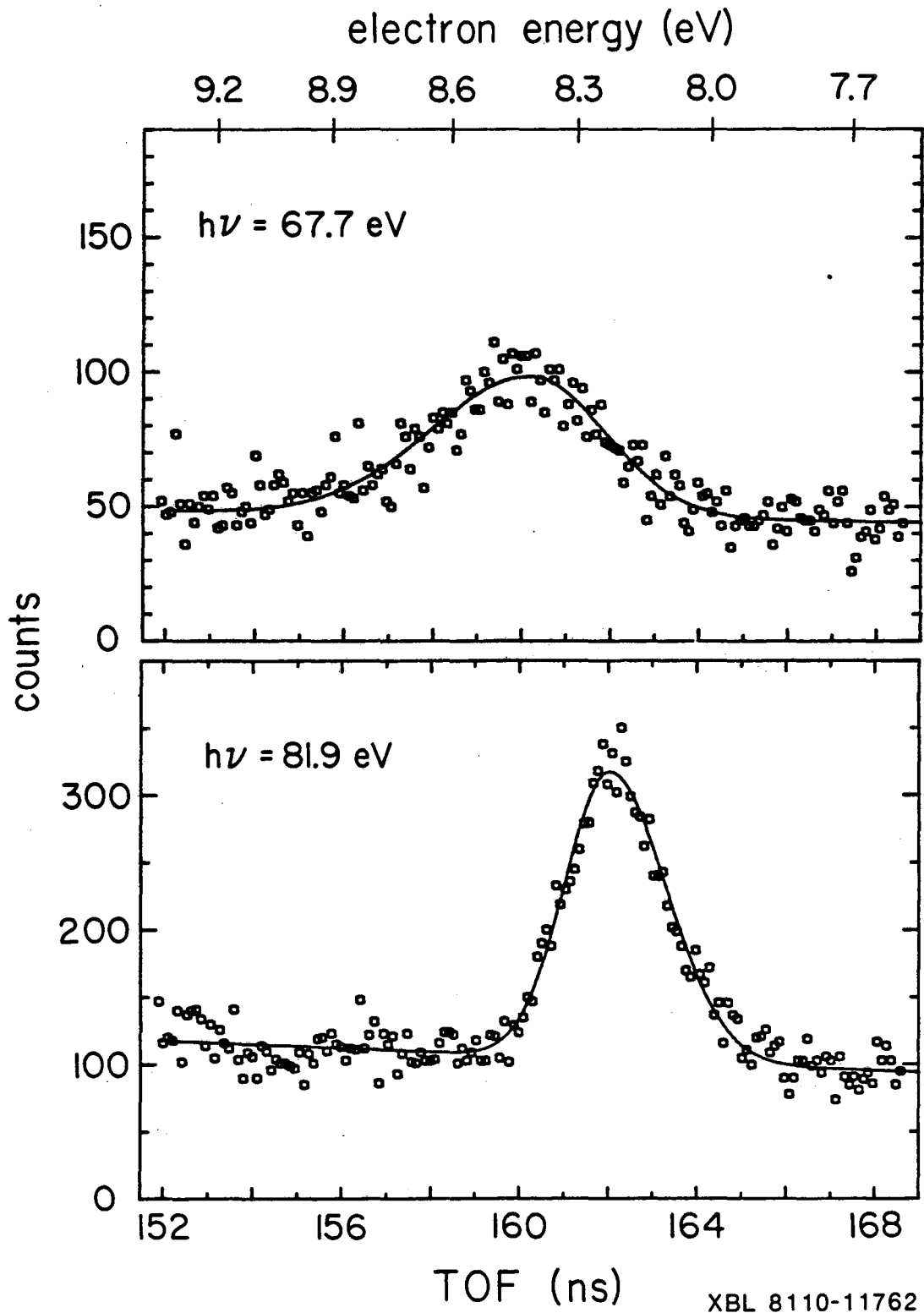
Figure 8

XBL 8110-11762
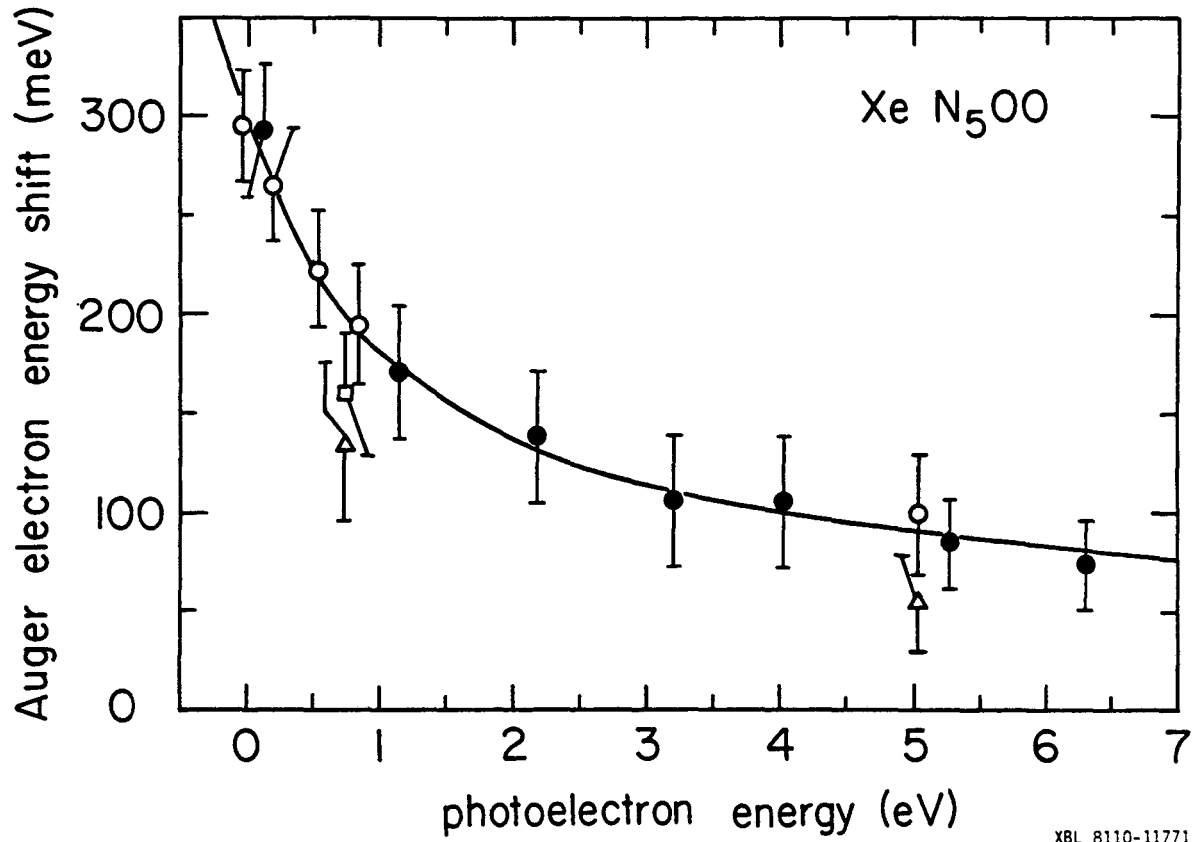
Figure 9

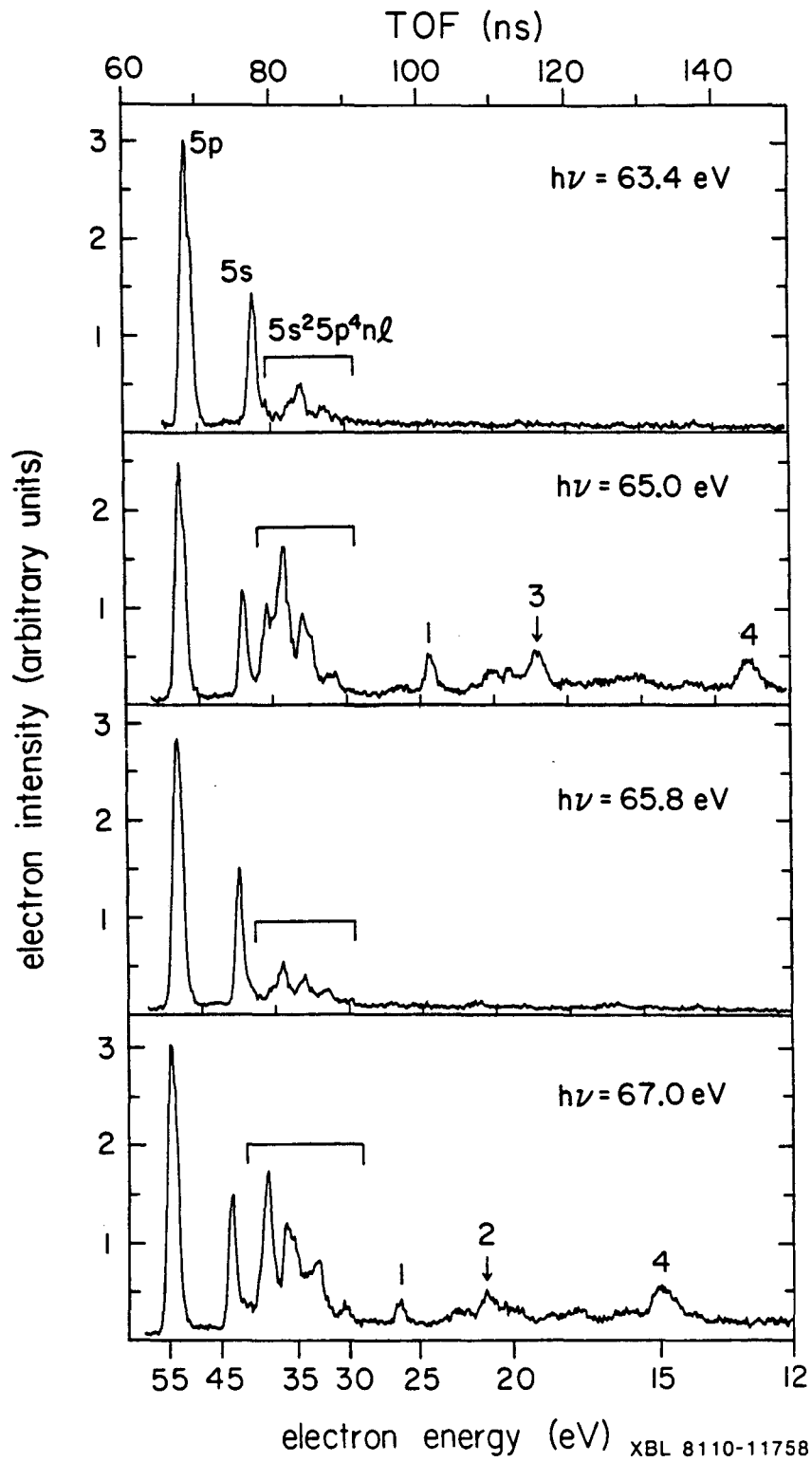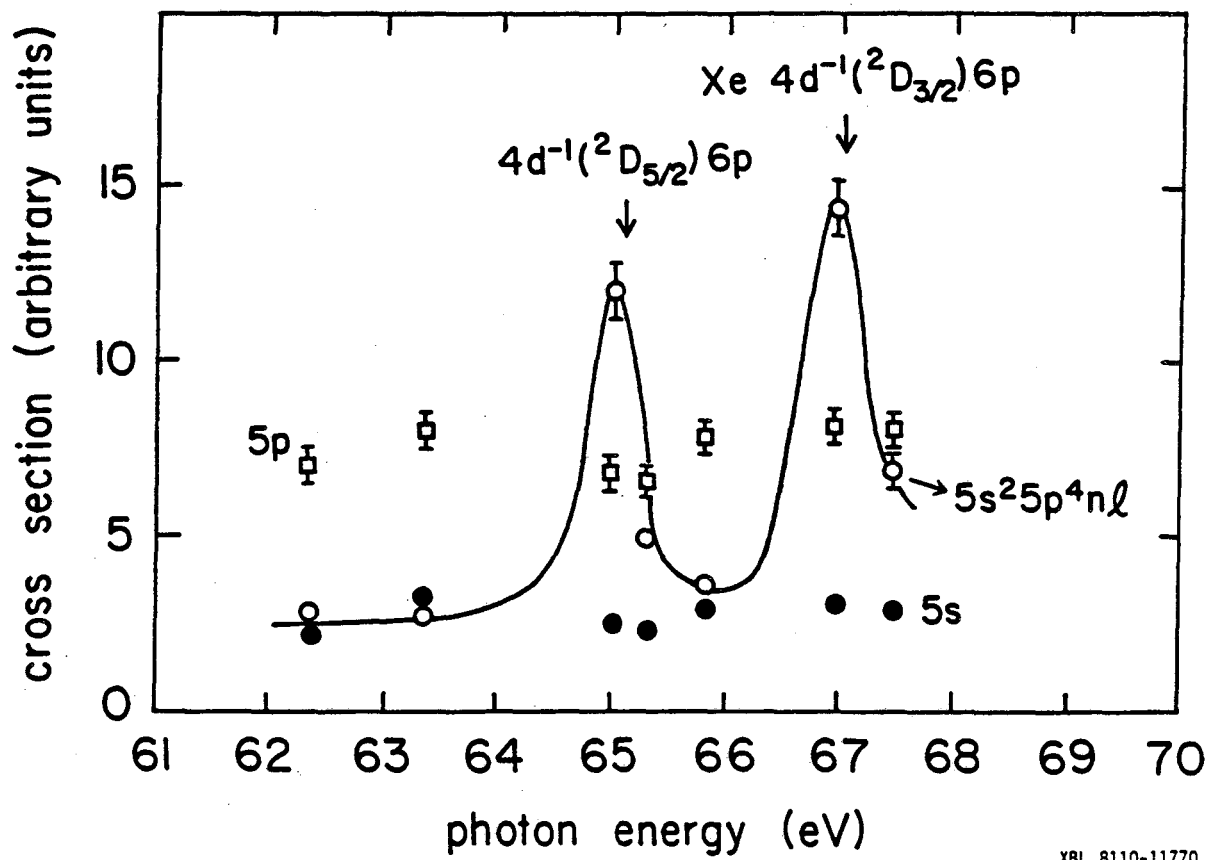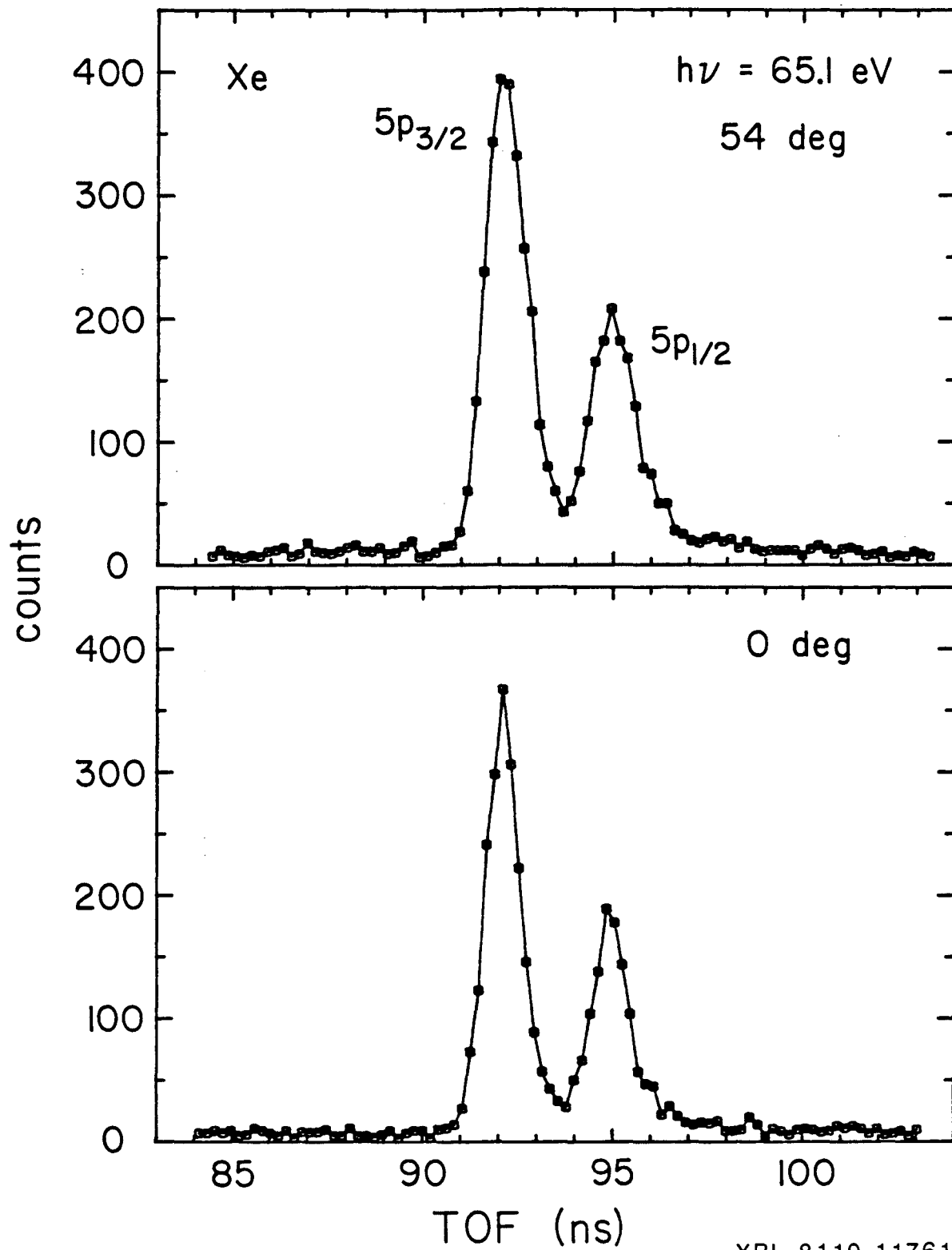XBL 8110-11771
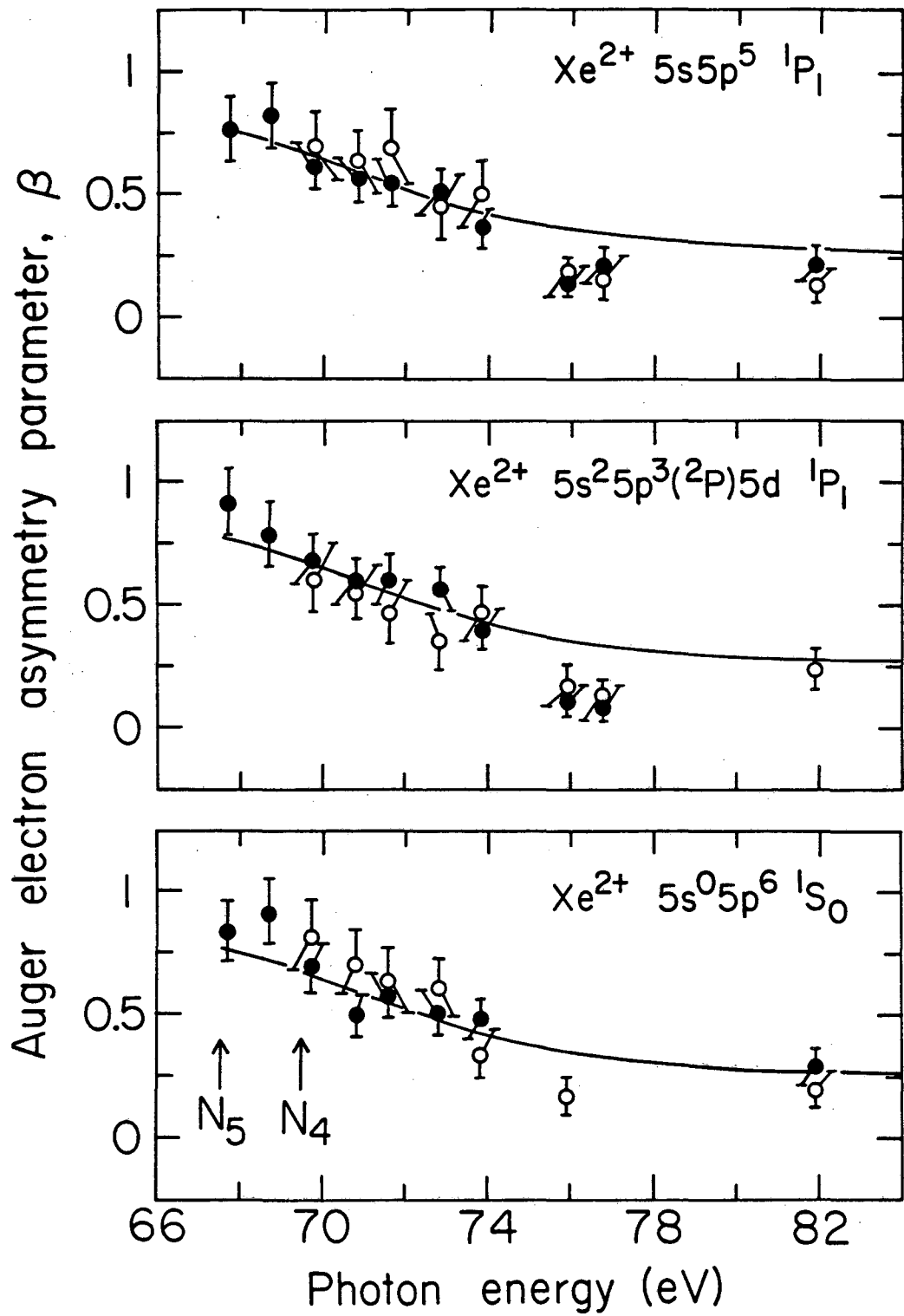
Figure 10

XBL 8112-13001
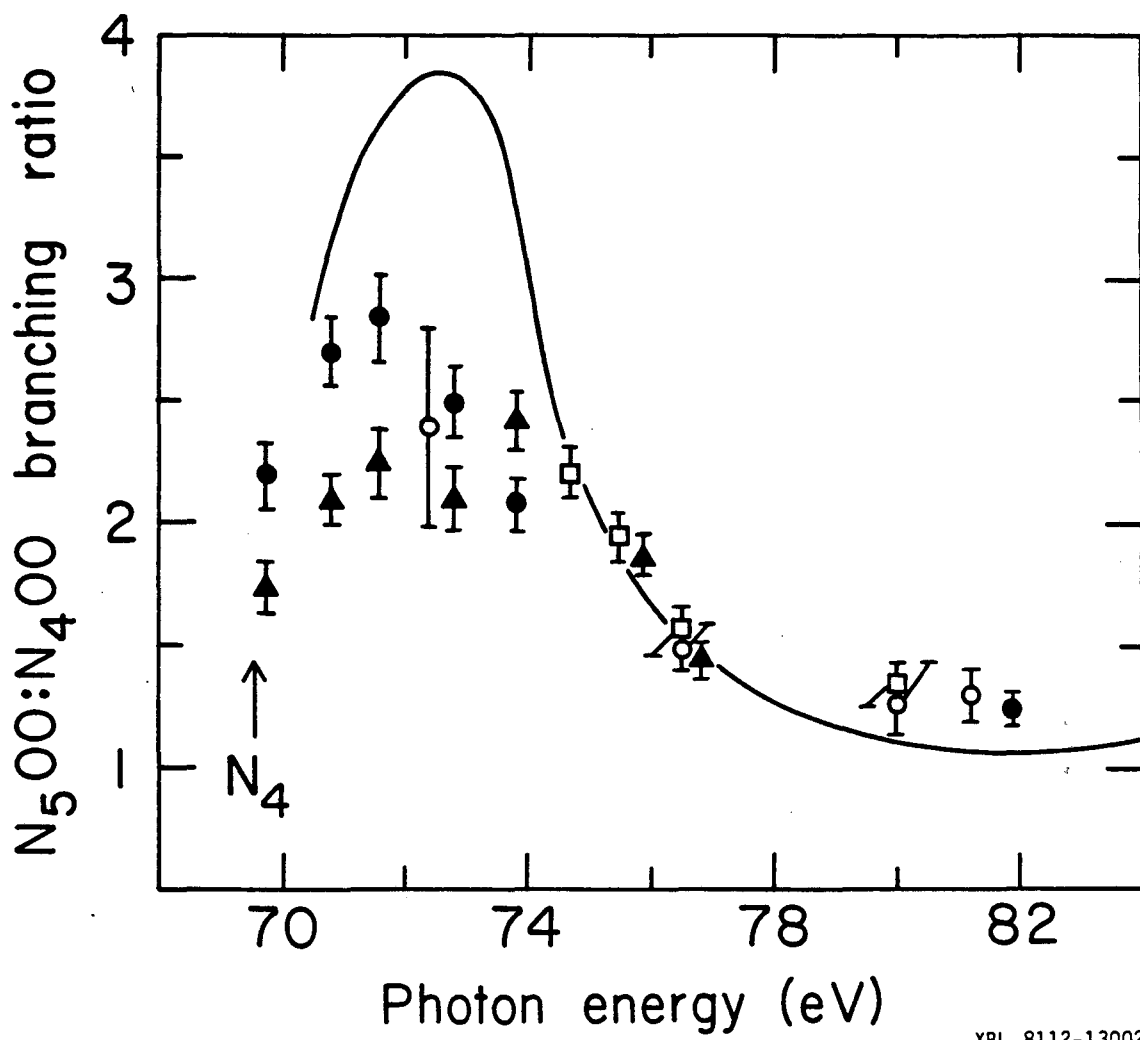
Figure 11

XBL 8112-13002
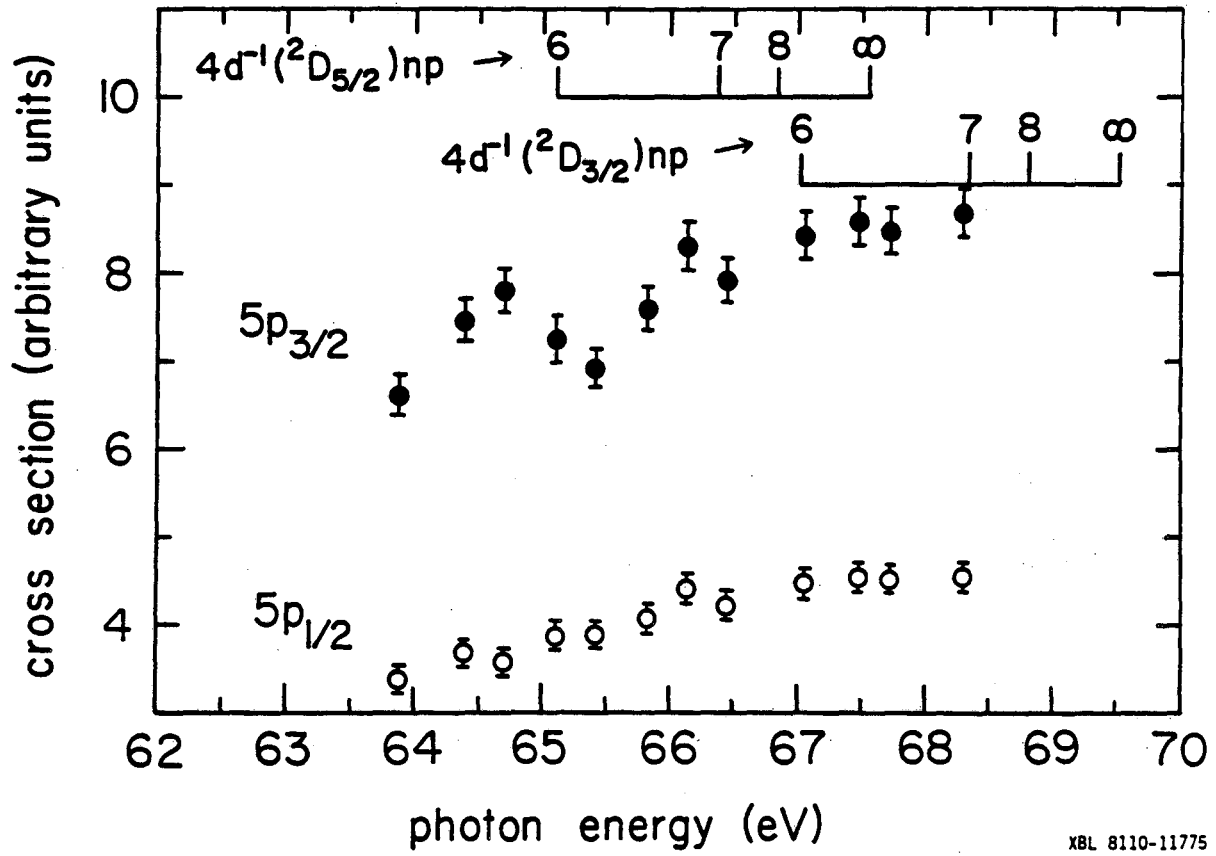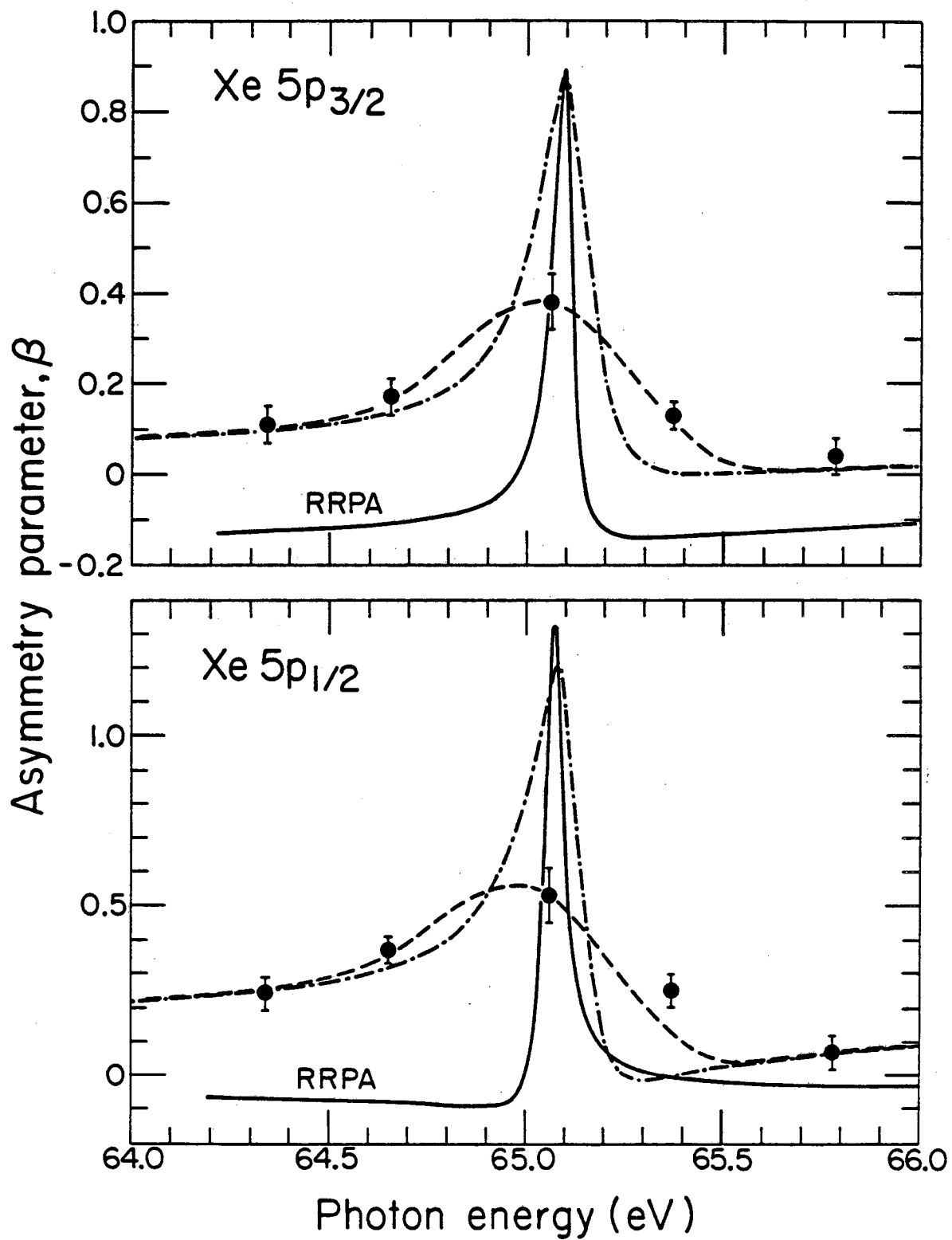
Figure 12
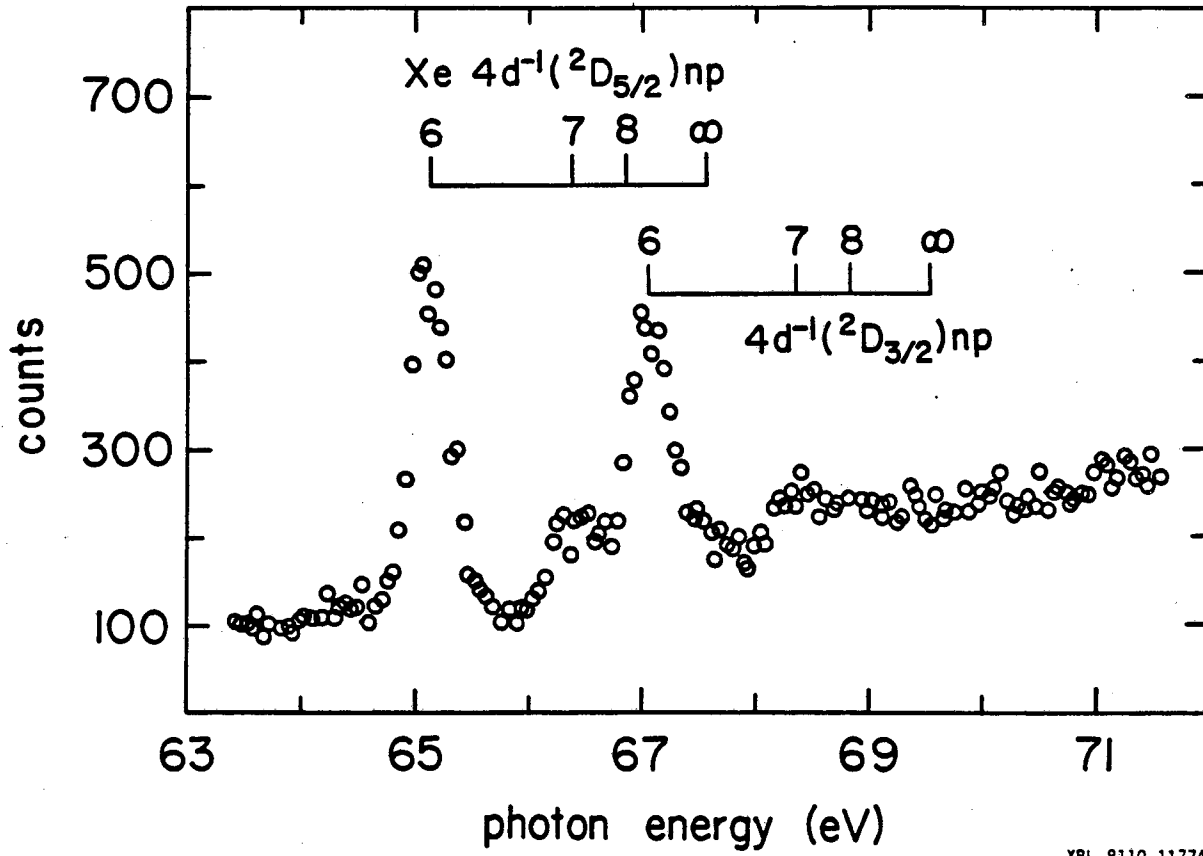
XBL 8110-11774

Figure 13

Figure 14

XBL 8110-11770

Figure 15

XBL 8110-11761
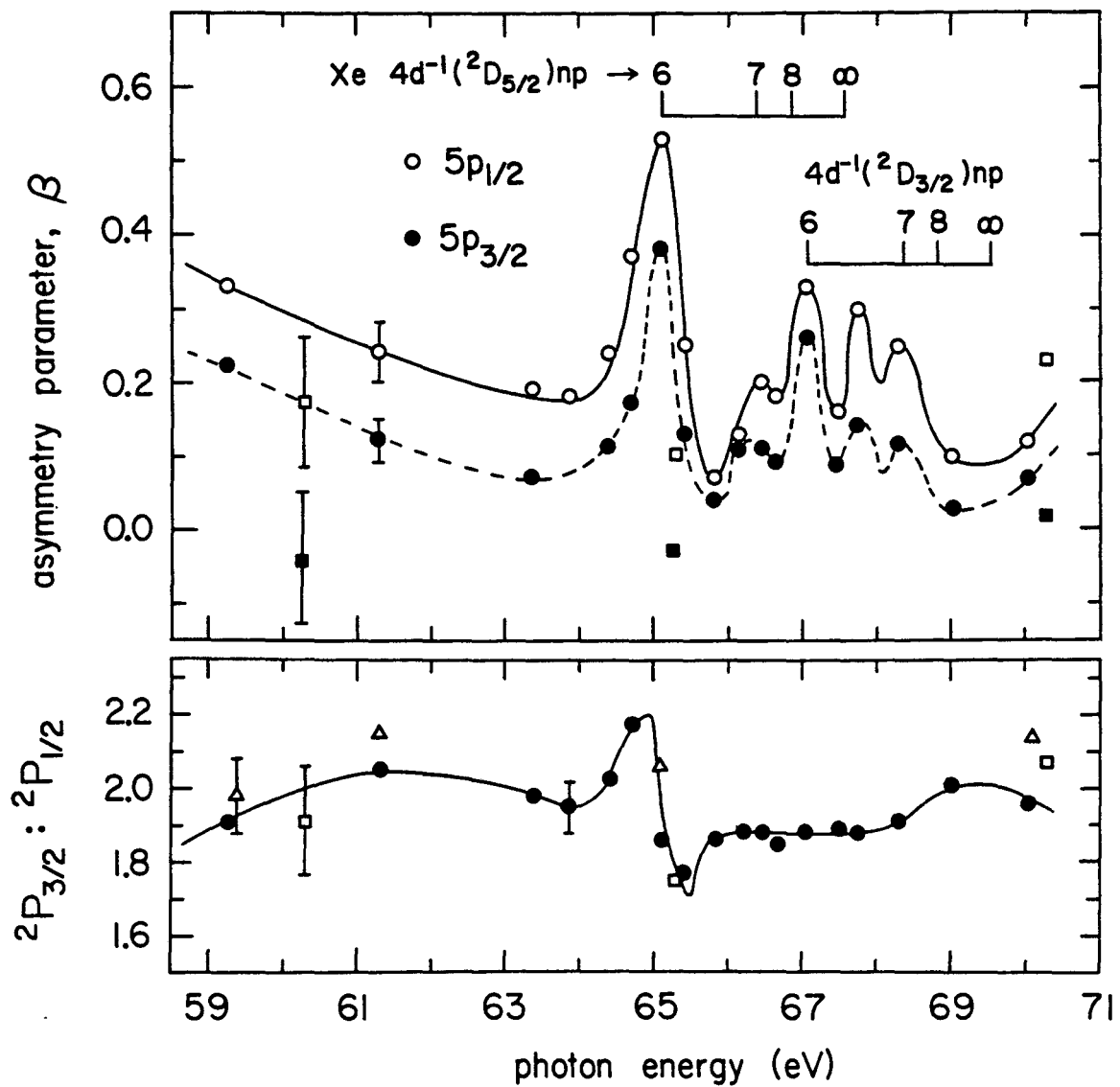
Figure 16

XBL 8110-11759

Figure 17
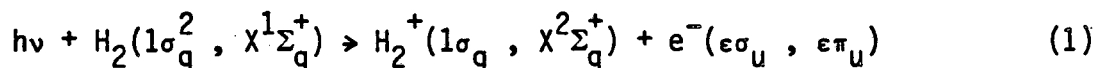
Figure 18

XBL8111-12064
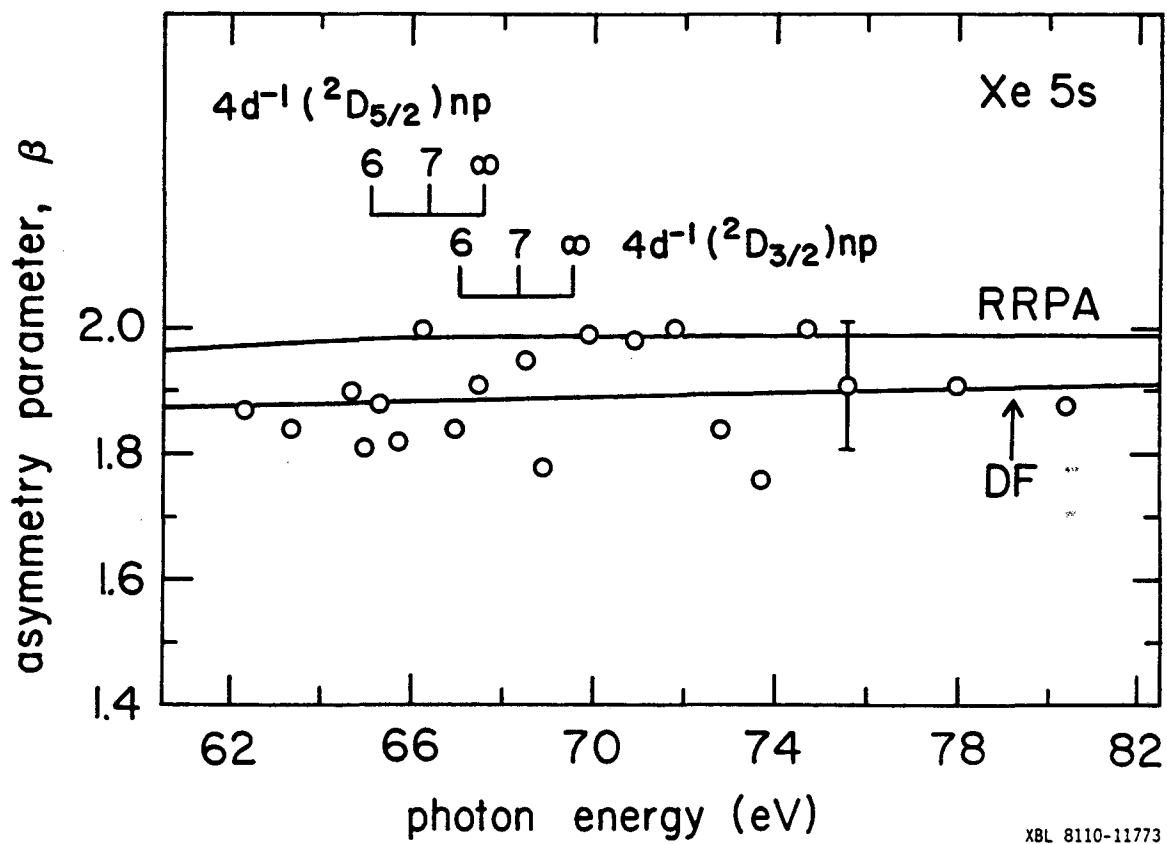
Figure 19

IV. PHOTOELECTRON ANGULAR DISTRIBUTIONS FROM H_2 and D_2

A. Introduction

The relatively simple two-electron structure of H_2 has made it a prototype system for study in the development of theoretical models of molecular photoionization. The photoionization process is described by

$$h\nu + H_2(1\sigma_g^2 , X^1\Sigma_g^+) \rightarrow H_2^+(1\sigma_g , X^2\Sigma_g^+) + e^-(\epsilon\sigma_u , \epsilon\pi_u) \qquad (1)$$

As described in Chapter I, angular momentum and parity conservation restrict the form of the photoelectron angular distribution.[1] For the case of photoejection from randomly oriented target molecules by electric dipole interaction, the photoelectron angular distribution is completely characterized by the asymmetry parameter $\beta(\epsilon)$. It is restricted to values in the range $-1 \leq \beta(\epsilon) \leq 2$.

In the united-atom limit of photoemission for molecular hydrogen, namely He $1s \rightarrow \epsilon p$, an energy-independent asymmetry $\beta = 2$ is required,[2] so that deviations from $\beta = 2$ reflect the non-spherical molecular structure of H_2. This result illustrates the general motivation for the measurement and theoretical calculation of molecular photoelectron asymmetries, i.e., $\beta(\epsilon)$ is sensitive to the anisotropic, molecular electronic structure.[3] Thus, $\beta(\epsilon)$ for the photoionization of H_2 is determined by the dipole matrix elements and relative phases for the two continuum channels $1\sigma_g \rightarrow \epsilon\sigma_u$ and $\epsilon\pi_u$ (see,

for example, Dill[5]). Several theoretical calculations of $\beta(H_2)$ have been published,[4-17] and a number of groups have measured $\beta(H_2)$ using discrete resonance line radiation.[18-24] Recently, Marr et al.[25] reported measurements over the photon energy range 18–30 eV using synchrotron radiation.

There is rough agreement among the theoretical values of $\beta(H_2)$, with a range of 0.2–0.3 β unit, and among the experimental values, with a similar range. However, detailed agreement is absent. In particular, the β values of Marr et al.[25] are consistently lower than those measured using resonance lamps. In light of these residual discrepancies, and because we have an apparatus that is relatively free of the systematic errors usually inherent in β measurements, we have made another synchrotron radiation based set of $\beta(H_2)$ measurements, reported below. Also included are results for D_2, which comprise another motivation for this work.

The measurements were made on the VUV beam line at SSRL, using our double-angle-TOF photoelectron spectrometer. Experimental details are given in Chapter II. For completeness it is noted here that the photon beam was about 97 percent linearly polarized, and the monochromator bandpass was 2.7Å FWHM. As described in Chapter II, the β values reported here were corrected slightly (by <0.03 β unit), to account for incomplete linear polarization of the photon beam and for angle-averaging of the photoelectron source region over the collection solid angles of the detectors.

B. Results and Discussion

An example of the 0° and 54.7° TOF spectra of H_2 is shown in
Fig. 1. A resolution of approximately 3 percent of the kinetic energy
was attained in the TOF spectra, hence vibrational structure was gen-
erally not resolved. The values of $\beta(H_2)$ and $\beta(D_2)$ reported here
represent the total photoelectron bands, i.e., summed over all rota-
tional and vibrational transitions. The results, listed in Table I,
are plotted in Fig. 2 along with theoretical curves, the measurements
of Marr et al.,[25] and the resonance line measurements of Morgenstern
et al.[20] All of the theoretical calculations predict a large asym-
metry and a slow variation of $\beta(H_2)$ with energy, but they differ in
the precise magnitude of $\beta(H_2)$ and the slope of the energy variation.
The present measurements agree well with the earliest published theo-
retical calculations: those of Tully et al.,[4] of Shaw and Berry,[6]
and with the semi-empirical threshold value calculated by Dill.[5] A
least-squares line fit through the present measurements of $\beta(H_2)$ and
$\beta(D_2)$ indicates that β slowly increases with increasing energy.

Accurate measurements of $\beta(H_2)$ are clearly required for a criti-
cal evaluation of the theoretical calculations. The resonance line
measurements[18-24] tend toward larger asymmetries than those measured
using synchrotron radiation. We note that the resonance line radia-
tion is concentrated into a much smaller bandpass ($\Delta h\nu \approx 10$ meV FWHM),
than the synchrotron radiation ($\Delta h\nu \approx 100$ meV FWHM). Hence, photo-
electron measurements using the two radiation sources differ greatly
in their sensitivity to any possible resonance or threshold structure

in the photoabsorption spectrum. In particular, the Ne(I) resonance lines at $h\nu$ = 16.85 eV and 16.67 eV, with which the largest measured asymmetries plotted in Fig. 1 were obtained, lie energetically between vibrational thresholds of H_2^+. A recent theoretical study[17] of vibrational preionization in H_2 would indicate that the Ne(I) line β measurements are almost certainly influenced by autoionization. The measurements reported here were obtained over a photon energy range where only direct ionization apparently occurs.[27]

We should comment also on the analysis of Kibel et al.[23] concerning loss of observed asymmetry due to elastic scattering of the photoelectrons before they reach the detector. In the present technique elastic scattering is accounted for, to a great extent, by the calibration procedure (see the discussion in Chapter II). Even if scattering decreases the experimental photoelectron asymmetry, the observed asymmetries are scaled to the known β values of the calibration lines. The calibration procedure amounts to an "adjustment" of the experimental asymmetries to account for elastic scattering (and other experimental non-idealities) in the spirit of the adjustments adopted by Kibel et al. In particular, we believe the present results are not too low, because we also obtain an observed "β value" of 2.06 ± 0.03 as an average for the He 1s → ϵp asymmetry over $h\nu$ = 27-32 eV; i.e., a value that is slightly too high, because values over 2 are not possible.

Virtually identical β values were observed for H_2 and D_2, within the precision of the measurements. The averages of the measurements listed in Table 1 give $\beta(H_2) = 1.71 \pm 0.02$ and $\beta(D_2) = 1.73 \pm 0.02$ over $h\nu = 19\text{-}27$ eV. It is of interest to inquire whether different β values should be expected for H_2 and D_2, and to determine which factors might produce a variation. If the Born-Oppenheimer separation of nuclear and electronic wavefunctions is adopted for a diatomic molecule, the electronic states are characterized by potential curves,[28] which represent the sum of electronic energy plus nuclear Coulombic repulsion as a function of internuclear distance. Other than a very small difference due to variations in the reduced mass, the potential curves are independent of nuclear mass, so identical curves represent the $X^1\Sigma_g^+$ and $X^2\Sigma_g^+$ states of H_2 and D_2 and of H_2^+ and D_2^+, respectively. Nearly identical wavefunctions therefore describe the motion of the photoelectron in the (fixed-nuclei) field of the molecular ion. The β measurements reported here, in which rotational and vibrational structure was not resolved, essentially represent the vertical overlap of the $X^1\Sigma_g^+$ and $X^2\Sigma_g^+$ potential curves. Since these are identical for the two isotopes, identical β values are expected.

The reduced mass of D_2 is twice that of H_2. Thus, when the fixed-nuclei approximation is lifted, quite different energies result for the rotational and vibrational levels. Considering first the vibrational structure, Itikawa[14,29] has shown theoretically that the

photoionization transition moment varies significantly with the internuclear separation. This effect, along with a dependence of the transition moment on photoelectron energy, leads to non-Franck-Condon vibrational branching ratios and β values which vary appreciably with the vibrational level of the ionic state. These effects have been confirmed by Berkowitz and Spohr[30] in measurements of vibrational branching ratios for H_2^+, D_2^+, and HD^+, and later for H_2^+ by Gardner and Samson.[31] Kreile and Schweig[24] have recently measured β values at 21.22 eV for vibrational levels of H_2^+ which vary in excellent agreement with theory.[14] Thus, for the vibrationally averaged results of the present experiment, we would expect a difference between $\beta(H_2)$ and $\beta(D_2)$ to the extent that the transition moment is weighted differently over the internuclear separation and photoelectron energy. The vibrationally resolved photoelectron spectra of H_2 and D_2 differ qualitatively in the vibrational branching ratios,[30] but this is due primarily to the quite different energy spacing of the vibrational levels in the ionic state. The centers of gravity of the photoelectron bands occur at nearly the same binding energy, which is consistent with the model of a vertical transition between the ground and ionic potential curves. Therefore, considering that the variation of $\beta(H_2)$ with vibrational level is rather small,[24] only a small difference between $\beta(H_2)$ and $\beta(D_2)$ is expected for the vibrationally averaged photoelectron bands, in good agreement with experiment.

A strong variation between $\beta(H_2)$ and $\beta(D_2)$ would be expected if a significant difference were to occur in the rotational structure of the photoelectron spectra. Dill[5] has used the angular momentum transfer formalism to show that strong variations in $\beta(H_2)$ are expected among particular $N \rightarrow N'$ rotational transitions. Rotational structure has been partially resolved in photoelectron spectra of H_2 using resonance line radiation.[21,32,33] About 90 percent of the transitions occur with $\Delta N = 0$, i.e., with no change in the rotational quantum number. The remaining 10 percent of the transition probability occurs with $\Delta N = \pm 2$. Dill[5] has shown that the $\Delta N = 0$ transitions proceed predominantly with zero angular momentum transferred to molecular rotation, with the result that $\beta(\Delta N = 0) \simeq 2$. In contrast, the $\Delta N = \pm 2$ transitions occur with the transfer of two units of angular momentum and have much smaller asymmetries. To good approximation, the photoelectron is produced only in p-waves ($\ell = 1$), and in this limit, $\beta(\Delta N = \pm 2) = 0.20$. The calculations of Itikawa[14] for $\beta(H_2)$, which include the effects of higher partial waves, also predict this strong qualitative difference between $\Delta N = 0$ and $\Delta N = \pm 2$ photoelectron asymmetries. The rotationally resolved measurements of Niehaus and Ruf[21] indeed found $\beta(\Delta N = 0) \simeq 2$, with a much smaller asymmetry observed for $\Delta N = 2$. Thus, if an appreciable difference should occur between H_2 and D_2 in the relative weights of $\Delta N = 0$ and $\Delta N = \pm 2$ transitions, a strong variation between $\beta(H_2)$ and $\beta(D_2)$ would result for the rotationally averaged photoelectron bands.

A variation between H_2 and D_2 in the rotational structure of their photoelectron spectra might occur due to the vibration-rotation interaction[34] or due to the coupling of electronic and nuclear motions. Itikawa[14] has computed transition strengths and asymmetry parameters for specific ro-vibrational transitions in the photoelectron spectrum of H_2. Coupling between electronic and nuclear motions was neglected as well as vibration-rotation interaction. However, the predicted relative intensities of the ro-vibrational transitions are in good agreement with the measurements of Morioka et al.[33] at 21.22 eV. In particular, the theory accurately predicts the variation with final vibrational level of the relative intensity of $\Delta N = 2$ transitions. This indicates that electronic-nuclear and rotation-vibration interactions do not appreciably modify the rotational structure. In the absence of these effects, the rotationally averaged $\beta(H_2)$ and $\beta(D_2)$ are the same, as observed here experimentally.

It is important to clarify a point raised by Marr et al.[25] concerning theoretical calculations of $\beta(H_2)$. Those authors suggest that the discrepancy between their measurements and the much higher asymmetries predicted by fixed-nuclei calculations[9,11] is due to neglect of the $\Delta N = 2$ transitions in the calculations. This appeared to be a reasonable interpretation, since Dill[5] calculated a rotationally averaged $\beta(H_2) = 1.71$, which is in better agreement with the previous[25] and present synchrotron radiation measurements. However, as described by Dill,[5] his expression for the rotationally averaged $\beta(H_2)$ is entirely equivalent to the fixed-nuclei type of

calculation,[4] where rotational transitions are not explicitly considered. In the calculations of $\beta(H_2)$ reported to date[5,12-15] in which values for specific rotational transitions are obtained, the transition dipole matrix elements and continuum wave phase shifts do not depend on the rotational quantum numbers. The dependence of the differential cross section on the quantum numbers N and N' appears through the squares of angular momentum coupling coefficients, which serve as weighting factors for rotationally-independent transition probabilities.[5,35] When summed over the final rotational level N', however, the weighting factors sum to unity and the $\beta(H_2)$ expression is independent of N and N'. The $\Delta N = \pm 2$ transitions, as well as $\Delta N = 0$, are implicitly included in the fixed-nuclei calculations. The theoretical curves plotted in Fig. 2 differ only in the accuracy with which the dipole matrix elements and continuum wave phases are calculated. The rotationally averaged calculations of Refs. 12-15 all predict $\beta(H_2)$ curves higher than was measured, while the fixed-nuclei calculations of Refs. 4 and 6 agree well with experiment. The $\beta(H_2)$ values will, however, depend on rotational quantum numbers if the vibration-rotation or electronic-nuclear interactions are included.

As a note of interest, Pollard et al. have recently used molecular beam techniques to record the He(I) line photoelectron spectrum of H_2 with very high resolution.[36] Among their extensive set of results are β measurements for rotational transitions. They have obtained, tentatively, a value of $\beta = 0.69 \pm 0.14$ for the $\Delta N = 2$ transition at $h\nu = 21.2$ eV.[37]

References

1. C. N. Yang, Phys. Rev. 74 (1948) 764; M. Peshkin, Adv. Chem. Phys. 18 (1970) 1; V. L. Jacobs, J. Phys. B: Atom. Molec. Phys. 5 (1972) 2257; K.-N. Huang, Phys. Rev. A 22 (1980) 223.

2. J. Cooper and R. N. Zare, in Lectures in Theoretical Physics, S. Geltman, K. Mahanthappa, and W. Brittin, eds., Gordon and Breach, New York, 1969, Vol. 11C, p. 317; W. R. Johnson and C. D. Lin, J. Phys. B: Atom. Molec. Phys. 10 (1977) L331.

3. See, for example, D. Dill and J. L. Dehmer, J. Chem. Phys. 61 (1974) 692; Phys. Rev. Lett. 35 (1975) 213; J. Chem. Phys. 65 (1976) 5327; S. D. Druger, J. Chem. Phys. 64 (1976) 987.

4. J. C. Tully, R. S. Berry, and B. J. Dalton, Phys. Rev. 176 (1968) 95.

5. D. Dill, Phys. Rev. A 6 (1972) 160.

6. G. B. Shaw and R. S. Berry, J. Chem. Phys. 56, (1972) 5808.

7. J. J. Huang and F. O. Ellison, Chem. Phys. Lett. 29 (1974) 565.

8. B. Ritchie, J. Chem. Phys. 63 (1975) 1351.

9. F. Hirota, J. Electron Spectrosc. Relat. Phenom. 9 (1976) 149.

10. O. F. Kalman, Molec. Phys. 34 (1977) 397.

11. C. M. Dutta, F. M. Chapman, Jr., and E. F. Hayes, J. Chem. Phys. 67 (1977) 1904.

12. N. Chandra, Abstracts of Papers of the Xth International Conference on the Physics of Electronic and Atomic Collisions, Commissariat A L'Energie Atomique, Paris, 1977, p. 1210.

13. B. Ritchie and B. R. Tambe, J. Chem. Phys. 68 (1978) 755.

14. Y. Itikawa, Chem. Phys. 28 (1978) 461; 30 (1978) 109; 37 (1979) 401; Chem. Phys. Lett. 62 (1979) 261.

15. L.-Y. Chow Chiu and S. R. Samanta, J. Quant. Spectrosc. Radiat. Transfer 25 (1981) 253.

16. W. Thiel, Chem. Phys. 57 (1981) 227.

17. M. Raoult and Ch. Jungen, J. Chem. Phys. 74 (1981) 3388.

18. J. W. McGowan, D. A. Vroom, and A. R. Comeaux, J. Chem. Phys. 51 (1969) 5626.

19. T. A. Carlson and A. E. Jonas, J. Chem. Phys. 55 (1971) 4913.

20. R. Morgenstern, A. Niehaus, and M. W. Ruf, Abstracts of Papers of the VIIth International Conference on the Physics of Electronic and Atomic Collisions, North-Holland, Amsterdam, 1971, p. 167.

21. A. Niehaus and M. W. Ruf, Chem. Phys. Lett. 11 (1971) 55; a re-analysis of the data of Niehaus and Ruf has been given by E. S. Chang, J. Phys. B: Atom. Molec. Phys. 11 (1978) L69.

22. S. Katsumata, Y. Achiba, and K. Kimura, Chem. Phys. Lett. 63 (1979) 281.

23. M. H. Kibel, F. J. Leng, and G. L. Nyberg, J. Electron Spectrosc. Relat. Phenom. 15 (1979) 281.

24. J. Kreile and A. Schweig, J. Electron Spectrosc. Relat. Phenom. 20 (1980) 191.

25. G. V. Marr, R. M. Holmes, and K. Codling, J. Phys. B: Atom. Molec. Phys. 13 (1980) 283.

26. In the line source experiments of Ref. 20, β values were measured for individual vibrational levels v', but no variation of β with v' was observed.

27. L. C. Lee, R. W. Carlson, and D. L. Judge, J. Quant. Spectrosc. Radiat. Transfer 16 (1976) 873.

28. G. Herzberg, Spectra of Diatomic Molecules, 2nd ed., Van Nostrand Reinhold, New York, 1950, p. 146.

29. Y. Itikawa, J. Electron Spectrosc. Relat. Phenom. 2 (1973) 125.

30. J. Berkowitz and R. Spohr, J. Electron Spectrosc. Relat. Phenom. 2 (1973) 143.

31. J. L. Gardner and J. A. R. Samson, J. Electron Spectrosc. Relat. Phenom. 8 (1976) 123.

32. L. Åsbrink, Chem. Phys. Lett. 7 (1970) 549.

33. Y. Morioka, S. Hara, and M. Nakamura, Phys. Rev. A 22 (1980) 177.

34. D. Villarejo, J. Chem. Phys. 49 (1968) 2523.

35. U. Fano and D. Dill, Phys. Rev. A 6 (1972) 185.

36. J. E. Pollard, D. J. Trevor, Y. T. Lee, and D. A. Shirley, Rev. Sci. Instrum. 52, 1837 (1981).

37. J. E. Pollard, private communication.

Table 1. β values measured for the total (rotationally and vibrationally averaged) photoelectron bands of H_2 and D_2.

hν(eV)	H_2	D_2
19.0	1.67(5)	1.69(5)
20.0	1.66(6)	1.72(9)
20.6	1.71(8)	...
21.2	1.75(5)	1.82(5)
21.6	1.72(9)	...
22.0	1.70(7)	1.72(6)
23.0	1.77(6)	1.76(7)
24.0	1.66(9)	1.64(7)
25.0	1.70(6)	1.71(6)
26.0	1.76(9)	...
27.0	...	1.77(8)

Figure Captions

Fig. 1.   The $0°$ and $54.7°$ TOF photoelectron spectra of H_2 recorded at 25.0 eV photon energy.

Fig. 2.   Experimental β values for H_2 and D_2 with theoretical calculations for H_2. All of the experimental and theoretical results shown are for the rotationally and vibrationally averaged photoelectron bands[26]. Experimental: O, present results for H_2; ●, present results for D_2; □, Marr et al.[25] results for H_2; ⊗, Morgenstern et al.[20] results for H_2. The dashed line is a least-squares fitted line through the present results for H_2 and D_2. Theoretical curves: A, Chow Chiu and Samanta[15]; B, Ritchie and Tambe[13]; C, Thiel[16]; D, Dutta et al.[11]; E, Hirota[9]; F, Itikawa[14]; G, Tully et al.[4]; H, Shaw and Berry[6]. Theoretical calculations at one energy: J, Dill [5]; K, Chandra[12].

H_2^+ $X^2\Sigma_g^+$

$h\nu = 25.0$ eV

0 deg

54 deg

TOF (ns)
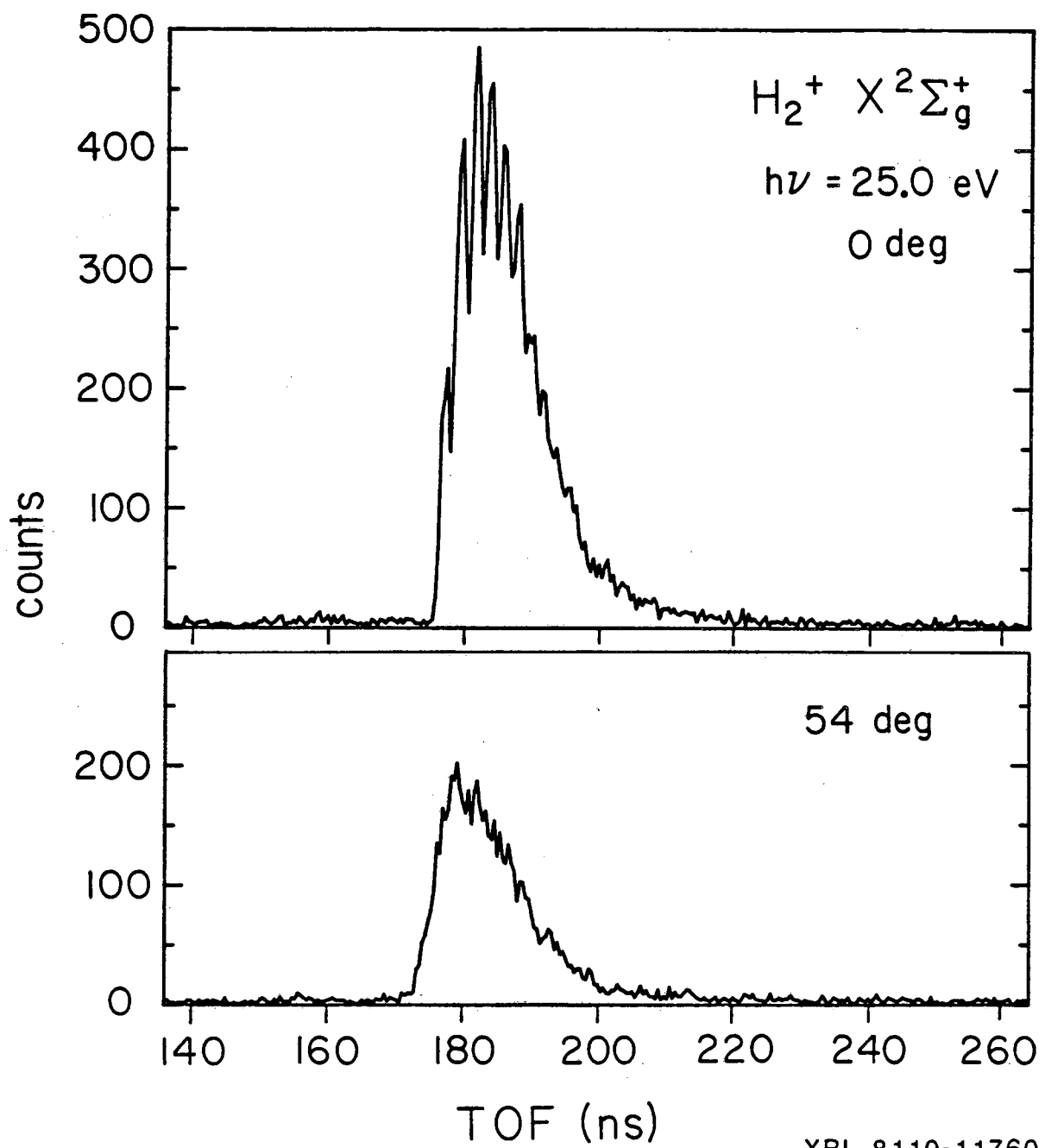
XBL 8110-11760
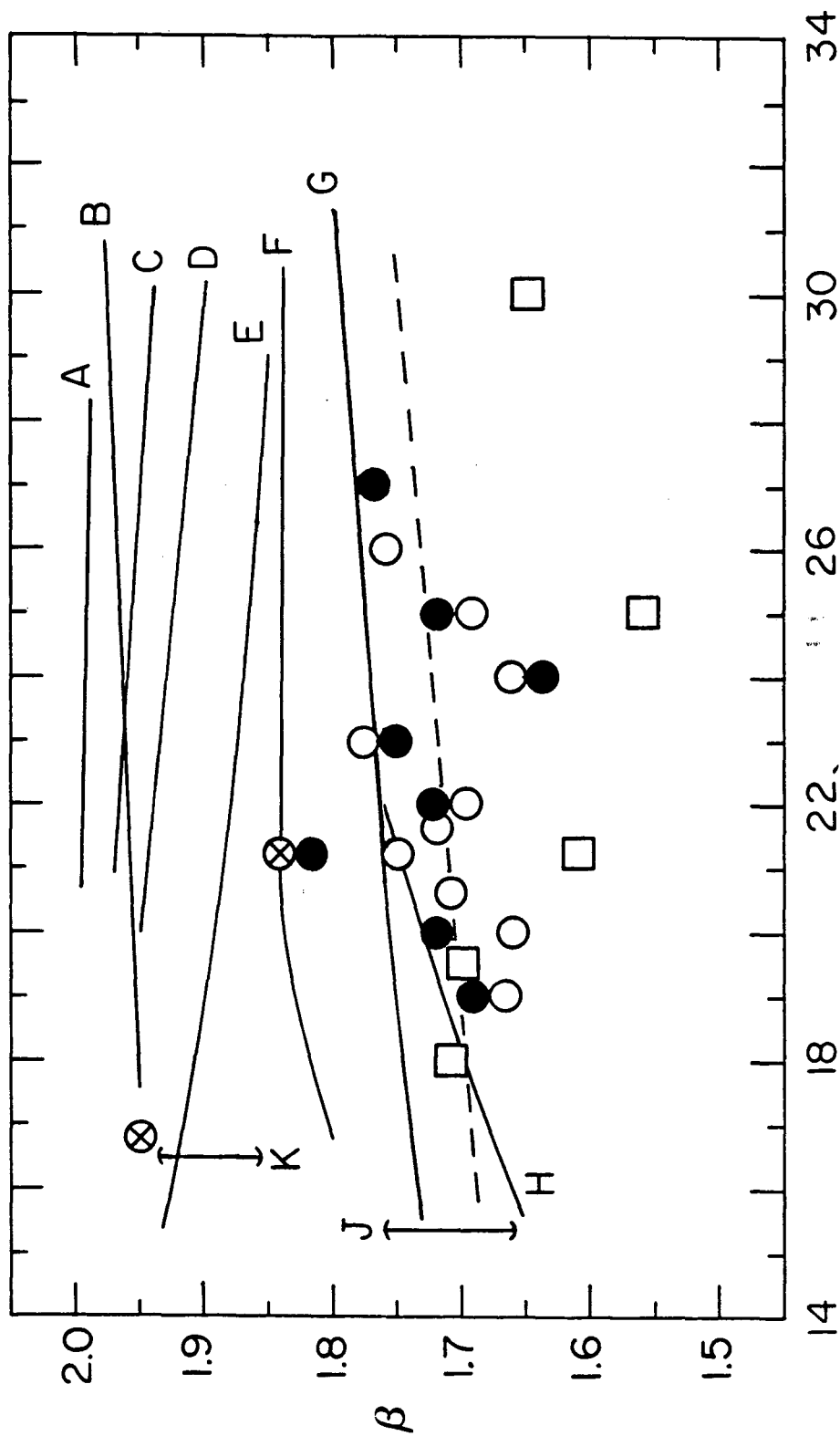
Figure 1

Figure 2

XBL 817-10543

V. PHOTOIONIZATION CROSS SECTIONS AND PHOTOELECTRON ASYMMETRIES
OF THE VALENCE ORBITALS OF NO

A. Introduction

Synchrotron radiation from the VUV beam line at SSRL (see Chapter II) was used to measure partial photoionization cross sections $\sigma(\epsilon)$ and photoelectron asymmetries $\beta(\epsilon)$ for the valence molecular orbitals of NO over the photon energy range $h\nu$ = 16-31 eV. The monochromator bandpass was 2.7Å FWHM. Features were observed which are attributed to a continuum shape resonance, as predicted by the multiple-scattering model (MSM) calculations.[1,2] Analogous shape resonance features have been observed in the related first-row diatomic molecules N_2, CO, and O_2 (see, for example, Refs. 3-10). The MSM[11] shows that this shape resonance occurs in the $\epsilon\sigma$ ionization channel and is produced predominantly by the f-partial wave (ℓ = 3). An alternative characterization of the shape resonance is provided by the method of improved virtual molecular orbitals (IVO).[13] In the IVO calculations, centrifugal barriers in the molecular ionic potential for high ℓ-wave components cause resonant trapping of the photoelectron into σ^* valencelike orbitals. For the 2π orbital of NO, a second, stronger resonance feature was also observed which is attributed to the $\epsilon\pi$ and $\epsilon\delta$ ionization channels. Vibrational structure was not resolved in the present photoelectron spectra of NO, however, we mention here that theoretical[9] and experimental [10] work on N_2 and CO has demonstrated that the vibrational structure can be highly

sensitive to the presence of a shape resonance. Strongly non-Franck-Condon vibrational branching ratios and vibrationally-dependent photo-electron asymmetries have been predicted and observed for N_2 and CO.

B. Results

Synchrotron radiation measurements of $\beta(\epsilon)$ for the valence orbitals of N_2 have been reported previously.[4,5,14] As a check on our experimental method we present $\beta(\epsilon)$ measurements for the $3\sigma_g$ molecular orbital, i.e., for the ground ionic state $N_2^+ X^2\Sigma_g^+$. The results[15] are plotted in Fig. 1 along with the measurements of Marr and co-workers[4,5] and those of Carlson et al.[14] Structure observed in the $\beta(\epsilon)$ measurements between 16–23 eV is due to autoionization.[17] Agreement among the three sets of measurements is good, with an average deviation of about 0.05 β unit.

The relative partial cross section determined for $N_2^+ X^2\Sigma_g^+$ from the magic angle TOF spectra reproduced the previously measured[3] 40 percent rise over $h\nu$ = 20–28 eV due to the $3\sigma_g \rightarrow \epsilon\sigma_u$ shape resonance.[13] Good agreement of the TOF results with previous measurements for $N_2^+ X^2\Sigma_g^+$ serve to confirm the calibration and data analysis procedures applied in these experiments.

The ground configuration of the open-shell molecule NO is

$$1\sigma^2 \, 2\sigma^2 \, 3\sigma^2 \, 4\sigma^2 \, 5\sigma^2 \, 1\pi^4 \, 2\pi^1 \, , \, X^2\Pi \quad .$$
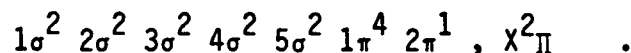
The antibonding 2π electron ($\pi*2p$) is bound by 9.3 eV, giving a $^1\Sigma^+$ ground ionic state in NO^+ that is easily resolved from the second band which starts at 15.7 eV in the photoelectron spectrum (see Fig. 2). However, due to alternative couplings of spin and orbital angular momenta in the final ionic states, ionization from the 1π and 5σ orbitals gives a series of seven overlapping photoelectron bands between 15.7 eV and 20.0 eV binding energy. These final states have been assigned, having been resolved in high resolution photoelectron spectra.[18,19] Unfortunately, the lower resolution ($\Delta\epsilon/\epsilon = 0.03$) attained in the present TOF spectra precludes an accurate deconvolution. However, ionization of a 5σ electron gives a predominantly $v' = 0$, $b^3\Pi$ photoelectron peak at 16.6 eV which is sufficiently strong to allow a reliable deconvolution of its intensity.

The band at 21.7 eV binding energy results from ionization of the 4σ orbital; however, assignment of the final state(s) remains controversial. Edqvist et al.[19] regard this band as the overlapped $c^3\Pi$ and $B^1\Pi$ final states derived from the 4σ orbital. However, Rydberg series recorded in absorption spectra[20] indicate that a single ionic state, the $c^3\Pi$, is formed at 21.7 eV. Theoretical calculations[21] support the assignment of $c^3\Pi$ for the 21.7 eV band. These calculations indicate that the $B^1\Pi$ $(4\sigma)^{-1}$ ionic state is strongly modified by configuration interaction and suggest that this state be assigned to a broad, weak band at 22.7 eV binding energy (not shown in Fig. 2; see Ref. 19). We adopt these assignments; i.e., the $c^3\Pi$ band at 21.7 eV and $B^1\Pi$ at 22.7 eV. Unfortunately, the 22.7 eV band was

recorded in only a few of the present TOF spectra and with low counting statistics, so $\beta(\epsilon)$ measurements are not reported.

The present TOF measurements for NO^+ $X^1\Sigma^+$, $b^3\Pi$, and $c^3\Pi$ were also quoted in Ref. 1, where the relative partial cross sections were scaled to absolute units (Mb) by normalizing the $X^1\Sigma^+$ partial cross section to 3.25 Mb at 21.2 eV photon energy. That normalization was determined from the photoionization yield measurements of Watanabe et al.,[22] the photoelectron branching ratio data of Bahr et al.,[23] and the total photoabsorption cross section tabulated by Berkowitz.[24] However, we prefer to adopt the more self-consistent normalization procedures used by Brion and Tan[25] and by Gustafsson and Levinson[26] for their partial cross section measurements of NO. Thus, the partial photoionization cross sections reported here have been scaled to units of Mb by apportioning the total photoabsorption cross section[24] according to the photoelectron branching ratios measured over $h\nu$ = 29-31 eV by the magic angle TOF detector. It is assumed that the photoionization yield[22] is unity at those energies. This normalization procedure increased the absolute partial cross sections reported here by 13 percent relative to the original normalization reported in Ref. 1. The branching ratios over 29-31 eV photon energies are listed in Table I along with those measured at 28 eV and 30 eV by dipole (e,2e);[25] the agreement is very good.

Present results for the photoionization cross sections and photoelectron asymmetry parameters are listed in Tables II and III, respectively. The results are plotted in Figs. 3-6 along with previous measurements[25,26,28] and theoretical curves from the MSM calculation.[1,2]

Three distinct resonant features are apparent in the partial cross section for NO^+ $X^1\Sigma^+$ in which the antibonding 2π (π^*2p) electron has been photoejected (see Fig. 3(a)). The strong, sharp resonance at 17.00 eV photon energy we attribute to autoionization of the Rydberg excitation $5\sigma \rightarrow 4p\pi$. This is the third member of the $\gamma(0,0)$ Rydberg series,[29] having as series limit the $A^1\Pi$ state of NO^+ at 18.32 eV binding energy. A maximum in the experimental cross section at $h\nu \approx$ 19 eV agrees well with the energy position of the small $2\pi \rightarrow \epsilon\sigma$ shape resonance predicted by the MSM. The strong, broad resonance centered at $h\nu \approx$ 29 eV in the TOF and (e,2e)[25] data is not reproduced by the MSM calculation. However, IVO calculations[30] for the corresponding π^*2p orbital in O_2 (the $1\pi_g$ orbital) predict a weak resonance near threshold in the $1\pi_g \rightarrow \epsilon\sigma_u$ channel and strong resonances in the $\epsilon\pi_u$ and $\epsilon\delta_u$ channels near 16 eV kinetic energy. Experimental cross section measurements[8] are in good agreement with the IVO theory. Therefore we tentatively attribute the strong, broad resonance in NO^+ $X^1\Sigma^+$ to the π and δ ionization channels. However, this interpretation requires confirmation by further theoretical work.

The photoelectron asymmetry measurements for the 2π orbital are plotted in Fig. 3(b) and agree well with line source measurements.[28] Oscillations in the measurements below 20 eV we attribute to the autoionization and $\epsilon\sigma$ resonances observed in the partial cross section. The MSM correctly predicts the rise of $\beta(\epsilon)$ with increasing energy, but the calculated values are too high by about 0.6 β unit.

Results for NO^+ $b^3\Pi$ are plotted in Fig. 4. The cross section measurements show a broad resonant feature centered near the energy position of the $5\sigma \rightarrow \epsilon\sigma$ resonance predicted by the MSM. The calculated feature is somewhat more narrow and intense than experiment. Very good agreement was obtained among the present $\beta(\epsilon)$ measurements, line source measurements,[28] and the calculated $\beta(\epsilon)$ curve. Structure in the measurements at low energies likely results from autoionization of the Rydberg-excited 4σ electron.[20]

Partial cross section measurements for NO^+ $c^3\Pi$ are plotted in Fig. 5(a). The present results are in conflict with previous measurements[26] based on synchrotron radiation for the energy position and intensity of the $4\sigma \rightarrow \epsilon\sigma$ shape resonance. The measurements of Ref. 26 place the resonance maximum near 29 eV, while the maximum was observed near 27 eV in the present measurements and with an absolute intensity 40 percent smaller. The (e,2e) data[25] and MSM calculation[1] also indicate the resonance maximum lies at higher energy than we report here. The present results were obtained over a more limited energy range, and we note an indication of two maxima in the data of Ref. 26, as was observed above for the 2π orbital. Thus, perhaps the first maximum was observed here. The difference in the magnitudes of the measured cross sections indicates a discrepancy in the measured photo-electron branching ratios. Table I shows that the present branching ratio measurements are in good agreement with the (e,2e) results. Note that the (e,2e) cross sections plotted in Fig. 5(a) are for the combined $c^3\Pi$ and $B^1\Pi$ ionic states,[27] which could not be resolved in the (e,2e) spectra. As shown in Table I and in Ref. 26, the $B^1\Pi$ band accounts

for 30 percent of the total $c^3\Pi + B^1\Pi$ intensity. Hence, the (e,2e) data are in good agreement with the present measurements for cross section magnitude, and the cross sections reported in Ref. 26 appear too large. The $\beta(\epsilon)$ measurements plotted in Fig. 5(b) exhibit the resonance minimum predicted by the MSM; however, the observed minimum lies 3 eV lower in energy and the calculated values are too high by 0.6 β unit.

Photoejection from the 1π and 5σ orbitals produces a series of seven overlapping bands in the photoelectron spectrum between 15.7 eV and 20.0 eV binding energy (see Fig. 2 and Refs. 18 and 19). It was not possible, in the present experiment, to isolate a single ionic state derived from the 1π orbital. However, at low energies it was possible to approximately deconvolute the intensities of the two 5σ-derived final states $b^3\Pi$ and $A^1\Pi$. The remaining intensity was due to the five final states, $a^3\Sigma^+$, $w^3\Delta$, $b'^3\Sigma^-$, $A'^1\Sigma^-$, and $W^1\Delta$, derived from the 1π orbital. Figure 6 shows $\beta(\epsilon)$ measurements pertaining to the average over these five $(1\pi)^{-1}$ ionic states.[31] The results are in very good agreement with fixed-nuclei MSM calculations[2] for the 1π orbital.

The present measurements and MSM calculations for NO and previous results[4-7] for N_2, CO, and O_2 show that π molecular orbitals produce qualitatively different $\beta(\epsilon)$ curves near threshold than do σ orbitals. For π orbitals, β is ≤ 0 near threshold, and it increases with energy to positive values. For the σ orbitals, β is generally large and positive at threshold, decreases somewhat (particularly through a shape resonance), then remains large and positive to high

energy. This observation is consistent with Chang's analysis[32] of molecular photoionization transitions in terms of parity favored-ness.[33] More simply, however, the $\beta(\epsilon)$ values produced near threshold likely reflect the orbital angular momentum composition of the molecular orbitals. Single-center expansions of σ molecular orbitals generally contain large components of $\ell = 0$ (s atomic orbital) angular momentum. Thus, the large $\beta(\epsilon)$ values for σ orbitals near threshold likely reflect large ns $\rightarrow$ ϵp components, which have[34] $\beta_{ns} = 2$. However, the π molecular orbitals contain $\ell \geq 1$ components, which produce smaller β values. For example,[34] $\beta(np \rightarrow \epsilon s) = 0$ and $\beta(np \rightarrow \epsilon d) = 1$.

C. Conclusions

The partial photoionization cross sections measured for the 2π, 5σ, and 4σ orbitals of NO exhibit shape resonance features attributed to the σ continuum in qualitative agreement with MSM calculations.[1] A strong shape resonance in the $(2\pi)^{-1}$ cross section is attributed to the π and δ continua and was not reproduced by the MSM theory. MSM calculations of photoelectron asymmetries for the 1π and 5σ orbitals are in very good agreement with the measured $\beta(\epsilon)$ values, but strong deviations between theory and experiment were obtained for the 2π and 4σ orbitals.

Shape resonances now appear to be prevalent, characteristic features in molecular photoionization spectra. The MSM has generally predicted these features and has clarified their dynamical nature.[11] However, the MSM is a semi-quantitative, one-electron model calculation, roughly equivalent to the Hartree-Slater (central field) model

of atomic photoionization.[35] More accurate theories of molecular photoionization in small molecules, on the level of Hartree-Fock accuracy, are highly desirable, so that one-electron processes are treated quantitatively, and the importance of many-electron and electronic-nuclear interactions can be assessed systematically. The IVO method[13] provides such a theoretical framework for the accurate calculation of partial photoionization cross sections. However, the present measurements on NO demonstrate that the photoelectron asymmetry $\beta(\epsilon)$ also is very sensitive to the accuracy of the theoretical calculation. Calculations of $\beta(\epsilon)$ for small molecules on the level of Hartree-Fock theory are currently in progress,[36] and the first results[37] are highly promising.

Vibrationally resolved measurements using synchrotron radiation, analogous to the work[9,10] on N_2 and CO, would help clarify the understanding of resonant photoionization of NO. Vibrationally dependent measurements for the NO^+ $X^1\Sigma^+$ state seem particularly feasible, because the ground state is energetically well separated from higher ionic states and several vibrational levels are populated.[18,19] Such measurements could be of particular value in clarifying the origin of the strong, broad resonance observed in the vibrationally-summed $(2\pi)^{-1}$ cross section.

Acknowledgements

We are grateful to Dr. S. Wallace and to Dr. V. McKoy and their respective co-workers for helpful discussions and communication of results prior to publication.

References

1. S. Wallace, D. Dill, and J. L. Dehmer, J. Chem. Phys., to be published.

2. S. Wallace, Ph. D. Thesis, Boston University (1980).

3. P. R. Woodruff and G. V. Marr, Proc. Roy. Soc. Lond. A $\underline{358}$, 87 (1977); E. W. Plummer, T. Gustafsson, W. Gudat, and D. E. Eastman, Phys. Rev. A $\underline{15}$, 2339 (1977); A. Hamnett, W. Stoll, and C. E. Brion, J. Electron Spectrosc. Relat. Phenom. $\underline{8}$, 367 (1976).

4. R. M. Holmes and G. V. Marr, J. Phys. B: Atom. Molec. Phys. $\underline{13}$, 945 (1980).

5. G. V. Marr, J. M. Morton, R. M. Holmes, and D. G. McCoy, J. Phys. B: Atom. Molec. Phys. $\underline{12}$, 43 (1979).

6. S. Wallace, D. Dill and J. L. Dehmer, J. Phys. B: Atom. Molec. Phys. $\underline{12}$, L417 (1979).

7. D. G. McCoy, J. M. Morton, and G. V. Marr, J. Phys. B: Atom. Molec. Phys. $\underline{11}$, L547 (1978).

8. C. E. Brion, K. H. Tan, M. J. van der Wiel, and Ph. E. van der Leeuw, J. Electron Spectrosc. Relat. Phenom. $\underline{17}$, 101 (1979); T. Gustafsson, Chem. Phys. Lett. $\underline{75}$, 505 (1980).

9. J. L. Dehmer, D. Dill, and S. Wallace, Phys. Rev. Lett. $\underline{43}$, 1005 (1979); G. Raseev, H. Le Rouzo, and H. Lefebvre-Brion, J. Chem. Phys. $\underline{72}$, 5701 (1980); Ref. 37.

10. R. Stockbauer, B. E. Cole, D. L. Ederer, J. B. West, A. C. Parr, and J. L. Dehmer, Phys. Rev. Lett. $\underline{43}$, 757 (1979); B. E. Cole, D. L. Ederer, R. Stockbauer, K. Codling, A. C. Parr, J. B. West, E. D. Poliakoff, and J. L. Dehmer, J. Chem. Phys. $\underline{72}$, 6308 (1980); Refs. 14 and 16.

11. J. L. Dehmer and D. Dill, J. Chem. Phys. $\underline{65}$, 5327 (1976); and in Ref. 12.

12. Electron-Molecule and Photon-Molecule Collisions, T. Rescigno, V. McKoy, and B. Schneider, eds. (Plenum, New York, 1979).

13. T. N. Rescigno, C. F. Bender, B. V. McKoy, and P. W. Langhoff, J. Chem. Phys. $\underline{68}$, 970 (1978); P. W. Langhoff in Ref. 12.

14. T. A. Carlson, M. O. Krause, D. Mehaffy, J. W. Taylor, F. A. Grimm, and J. D. Allen, Jr., J. Chem. Phys. $\underline{73}$, 6056 (1980).

15. The present $\beta(\epsilon)$ measurements are for the average over vibrations of the final state $N_2^+ \, X^2\Sigma_g^+$. The measurements of Refs. 4 and 5 are also for the average over vibrations in the photon energy range 23-32 eV, but are for $v' = 0$ only in the range 16-23 eV. The measurements taken from Ref. 14 and plotted in Fig. 1 are for $v' = 0$. The predominant $v' = 0$ transition accounts for about 90 percent of the intensity (see Ref. 16), so that β for $v' = 0$ differs from β averaged over vibrations by less than 0.10 β unit.

16. J. B. West, A. C. Parr, B. E. Cole, D. L. Ederer, R. Stockbauer, and J. L. Dehmer, J. Phys. B: Atom. Molec. Phys. $\underline{13}$, L105 (1980).

17. P. Gürtler, V. Saile, and E. E. Koch, Chem. Phys. Lett. $\underline{48}$, 245 (1977).

18. D. W. Turner, C. Baker, A. D. Baker, and C. R. Brundle, <u>Molecular</u> <u>Photoelectron Spectroscopy</u> (Wiley, London, 1970).

19. O. Edqvist, L. Åsbrink, and E. Lindholm, Z. Naturforsch. <u>26a</u>, 1407 (1971).

20. B. Narayana and W. C. Price, J. Phys. B: Atom. Molec. Phys. <u>5</u>, 1784 (1972); M. Sasanuma, Y. Morioka, E. Ishiguro, and M. Nakamura, J. Chem. Phys. <u>60</u>, 327 (1974).

21. H. Lefebvre-Brion, Chem. Phys. Lett. <u>9</u>, 463 (1971); P. W. Thulstrup, E. W. Thulstrup, A. Andersen, and Y. Öhrn, J. Chem. Phys. <u>60</u>, 3975 (1974).

22. K. Watanabe, F. M. Matsunaga, and H. Sakai, Appl. Opt. <u>6</u>, 391 (1967).

23. J. L. Bahr, A. J. Blake, J. H. Carver, J. L. Gardner, and V. Kumar, J. Quant. Spectrosc. Radiat. Transfer <u>12</u>, 59 (1972).

24. J. Berkowitz, <u>Photoabsorption, Photoionization, and Photoelectron</u> <u>Spectroscopy</u> (Academic, New York, 1979), p. 113.

25. C. E. Brion and K. H. Tan, J. Electron Spectrosc. Relat. Phenom. <u>23</u>, 1 (1981).

26. T. Gustafsson and H. J. Levinson, Chem. Phys. Lett. <u>78</u>, 28 (1981).

27. In Ref. 25 the photoelectron band at 21.7 eV is assigned as the combined states $c^3\Pi + B^1\Pi$, and the band at 22.7 eV is assigned $B'^1\Sigma^+$. Regardless of the assignments, the (e,2e) measurement is for the sum of the bands at 21.7 eV and 22.7 eV.

28. M. H. Kibel and G. L. Nyberg, J. Electron Spectrosc. Relat. Phenom. <u>17</u>, 1 (1979).

29. O. Edqvist, E. Lindholm, L. E. Selin, H. Sjögren, and L. Åsbrink, Ark. Fys. $\underline{40}$, 439 (1970); S. Takezawa, J. Molec. Spectrosc. $\underline{66}$, 121 (1977).

30. A. Gerwer, C. Asaro, B. V. McKoy, and P. W. Langhoff, J. Chem. Phys. $\underline{72}$, 713 (1980).

31. An approximate band center of 17.5 eV binding energy was chosen for this sum of the five 1π-derived ionic states.

32. E. S. Chang, J. Phys. B: Atom. Molec. Phys. $\underline{11}$, L293 (1978).

33. D. Dill and U. Fano, Phys. Rev. Lett. $\underline{29}$, 1203 (1972).

34. J. Cooper and R. N. Zare, in Lectures in Theoretical Physics, S. Geltman, K. Mahanthappa and W. Brittin, eds. (Gordon and Breach, New York, 1969), Vol. 11C, p. 317.

35. See, for example, S. T. Manson and J. W. Cooper, Phys. Rev. $\underline{165}$, 126 (1968); S. T. Manson, J. Electron Spectrosc. Relat. Phenom. $\underline{1}$, 413 (1973).

36. R. R. Lucchese and V. McKoy, Phys. Rev. A $\underline{21}$, 112 (1980); R. R. Lucchese, G. Raseev, and V. McKoy, "Studies of Differential and Total Photoionization Cross Sections of Molecular Nitrogen," Phys. Rev. A, to be published.

37. R. R. Lucchese and V. McKoy, J. Phys. B: Atom. Molec. Phys. $\underline{14}$, L629 (1981).

Table I. Photoelectron branching ratios (%) for NO^+.

State	Binding energy (eV)	Present results			$(e,2e)^b$	
		29 eV	30 eV	31 eV	28 eV	30 eV
$X^1\Sigma^+$	9.3	26(2)	26(2)	28(2)	26	26
$(1\pi+5\sigma)^a$	15.7–20.0	63(5)	62(5)	60(5)	63	61
$c^3\Pi$	21.7	8.8(7)	8.5(8)	8.2(8)	11^c	13^c
$B^1\Pi$	22.7	1.5(3)	3.1(5)	3.8(5)		

^{a}For the combined states $a^3\Sigma^+$, $b^3\Pi$, $w^3\Delta$, $b'^3\Sigma^-$, $A'^1\Sigma^-$, $A^1\Pi$, and $W^1\Delta$ derived from the 1π and 5σ orbitals.

^{b}Dipole (e,2e) results, Ref. 25.

^{c}For the combined states $c^3\Pi$ and $B^1\Pi$ (see note 27).

Table II. Partial photoionization cross sections (Mb) for NO^+.

$h\nu$(eV)	$X^1\Sigma^+$	$b^3\Pi$	$c^3\Pi$
16.5	5.5(8)	...	...
17.0	8.4(10)	...	...
17.3	4.5(6)	...	...
17.5	4.1(5)	...	...
18.0	4.4(5)	...	...
18.6	4.5(6)	6.6(8)	...
19.1	4.4(6)	7.5(8)	...
19.6	4.0(5)	6.7(8)	...
20.0	3.2(3)	6.0(7)	...
20.5	3.2(2)	6.7(8)	...
21.2	3.7(3)	6.6(8)	...
21.6	4.0(3)	6.8(8)	...
22.0	3.7(3)	6.9(8)	...
22.5	3.4(3)	7.2(8)	...
23.0	4.1(3)	7.3(6)	...
23.7	3.8(3)	7.2(6)	1.1(1)
24.3	4.5(3)	7.6(6)	1.4(2)
25.0	4.6(3)	7.4(6)	1.6(2)
26.0	4.9(4)	6.9(5)	1.6(2)
27.0	5.0(4)	6.4(5)	1.9(2)
28.0	5.1(4)	5.5(4)	1.8(2)
29.0	5.3(4)	5.3(4)	1.8(2)
30.0	5.0(4)	4.5(4)	1.7(1)
31.0	5.2(4)	4.2(3)	1.6(1)

Table III. Photoelectron asymmetry parameters β for NO^+.

$h\nu$(eV)	$X^1\Sigma^+$	$b^3\Pi$	$(1\pi)^a$	$c^3\Pi$
16.5	0.16(10)	...	...	...
17.0	-0.02(5)	...	...	...
17.3	0.20(7)	...	...	...
17.5	0.34(6)	1.11(9)	...	...
18.0	0.31(6)	0.84(6)	...	...
18.6	0.19(5)	0.59(5)	-0.24(5)	...
19.1	0.14(5)	0.44(4)	-0.20(4)	...
19.6	0.20(4)	0.61(5)	-0.02(4)	...
20.0	0.18(8)	0.72(5)	-0.06(7)	...
20.5	0.15(4)	0.53(4)	0.08(4)	...
21.2	0.19(4)	0.65(4)	0.25(4)	...
21.6	0.16(6)	0.66(5)	0.19(5)	...
22.0	0.27(6)	0.60(5)	0.43(5)	...
22.5	0.37(5)	0.66(4)	0.40(5)	...
23.0	0.28(4)	0.49(4)	0.49(5)	...
23.7	0.40(5)	0.43(7)	0.65(6)	0.38(7)
24.3	0.43(4)	0.40(6)	...	0.22(5)
25.0	0.52(5)	0.43(6)	...	0.09(5)
26.0	0.55(5)	0.43(6)	...	0.22(5)
27.0	0.68(5)	0.40(6)	...	0.09(4)
28.0	0.71(6)	0.52(7)	...	0.20(6)
29.0	0.66(10)	0.39(7)	...	0.30(8)
30.0	0.80(14)	0.51(11)	...	0.54(9)
31.0	0.61(15)	0.47(9)	...	0.73(12)

[a]For the average over the five final states $a^3\Sigma^+$, $w^3\Delta$, $b'^3\Sigma^-$, $A'^1\Sigma^-$, and $W^1\Delta$ derived from the 1π orbital (see note 31).

FIGURE CAPTIONS

Fig. 1. Photoelectron asymmetries for N_2^+ $X^2\Sigma_g^+$ measured using synchrotron radiation. ●, Present results; □, Ref. 14; solid line, Refs. 4 and 5 (see note 15).

Fig. 2. Energy-converted TOF spectra of NO recorded at $0°$ and $54.7°$ with respect to the photon polarization vector, and at 24.3 eV photon energy.

Fig. 3. Partial photoionization cross section (a) and photoelectron asymmetry (b) for NO^+ $X^1\Sigma^+$ $(2\pi)^{-1}$. Experimental: ●, present results; O, Ref. 25; X, Ref. 28. The solid line is the MSM theoretical calculation, Ref. 1.

Fig. 4. Partial photoionization cross section (a) and photoelectron asymmetry (b) for NO^+ $b^3\Pi$ $(5\sigma)^{-1}$. Experimental: ●, present results; X, Ref. 28. The solid line is the MSM theoretical calculation for the average over nuclear motion, Ref. 1.

Fig. 5. Partial photoionization cross section (a) and photoelectron asymmetry (b) for NO^+ $c^3\Pi$ $(4\sigma)^{-1}$. Experimental: ●, present results; ■, Ref. 26; O, Ref. 25 (see note 27 and discussion in the text). The solid line is the MSM theoretical calculation for the triplet fraction of $(4\sigma)^{-1}$ only, Ref. 1.

Fig. 6. Photoelectron asymmetry for the average over the states $a^3\Sigma^+$, $w^3\Delta$, $b'^3\Sigma^-$, $A'^1\Sigma^-$, and $W^1\Delta$ derived from the 1π orbital (see note 31). The solid line is the MSM theoretical curve, Ref. 2.

$$N_2^+ \quad X^2\Sigma_g^+ \quad (3\sigma_g)^{-1}$$

170

Figure 1

XBL 817-10545

Figure 2

Figure 3

XBL 817-10548

(a)

NO$^+$ b$^3\Pi$ (5σ)$^{-1}$

cross section (Mb)

(b)

β

photon energy (eV)
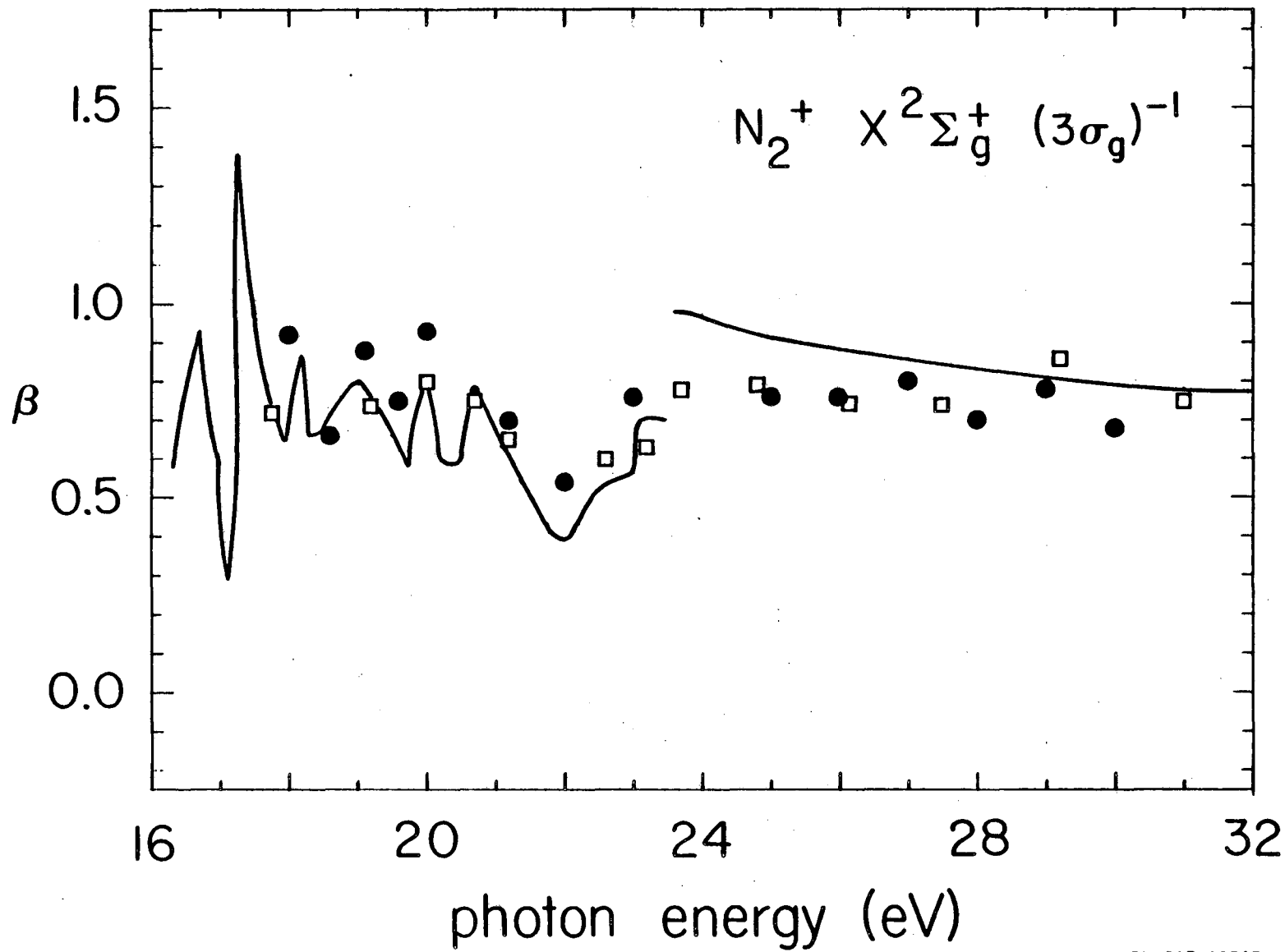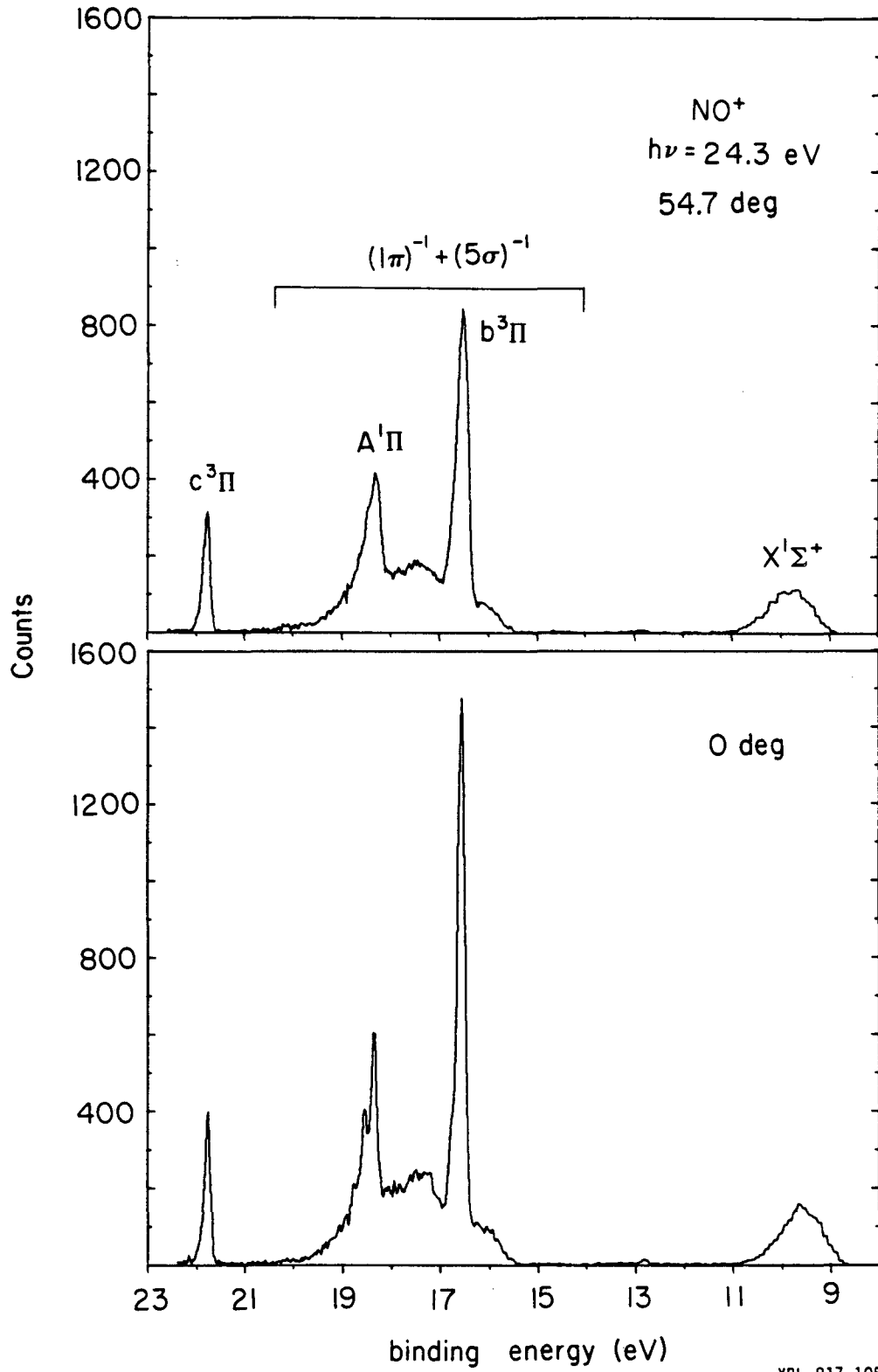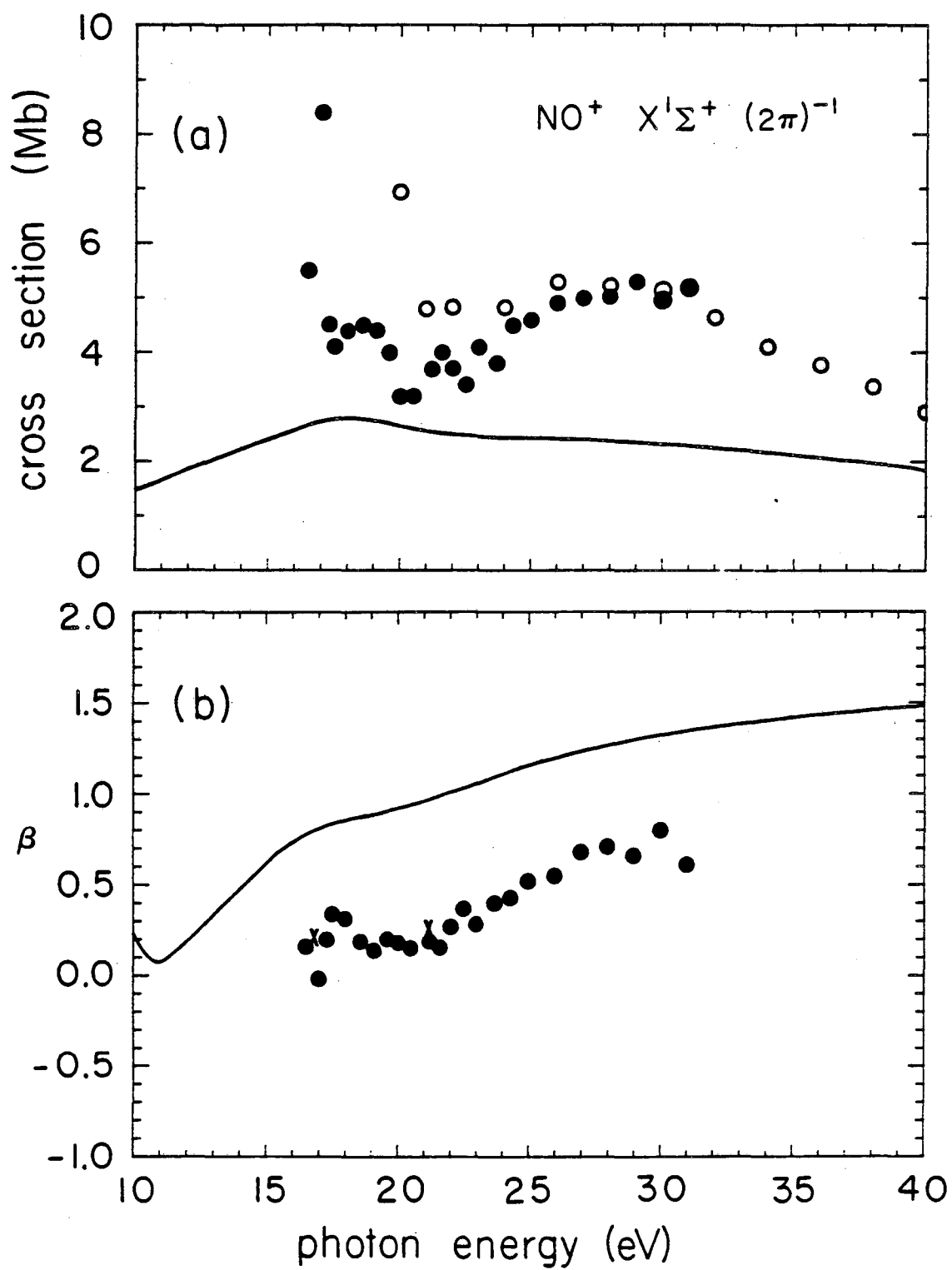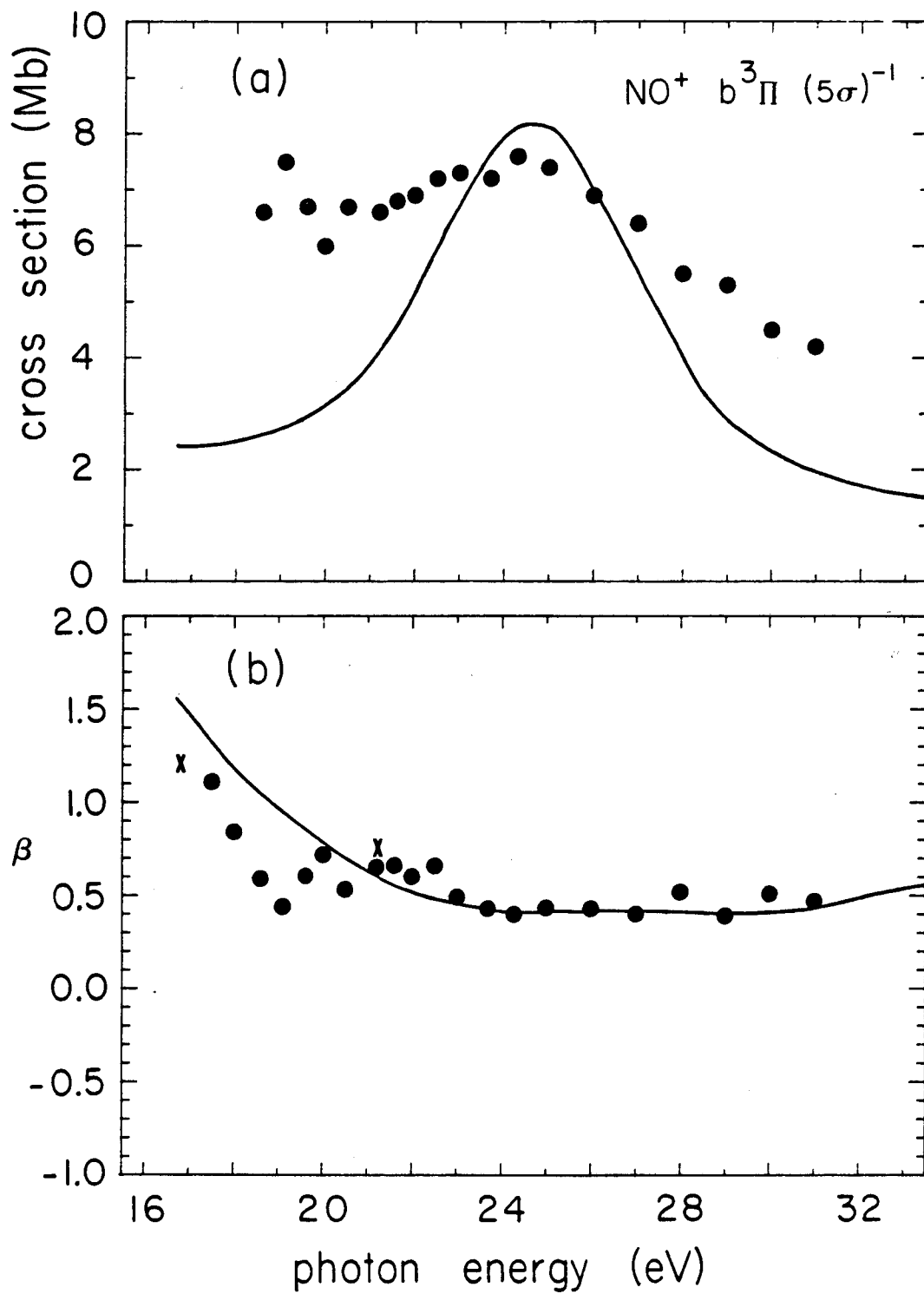
XBL 817-10549

Figure 4

Figure 5

XBL 817-10547

NO^+ $(1\pi)^{-1}$

β

photon energy (eV)
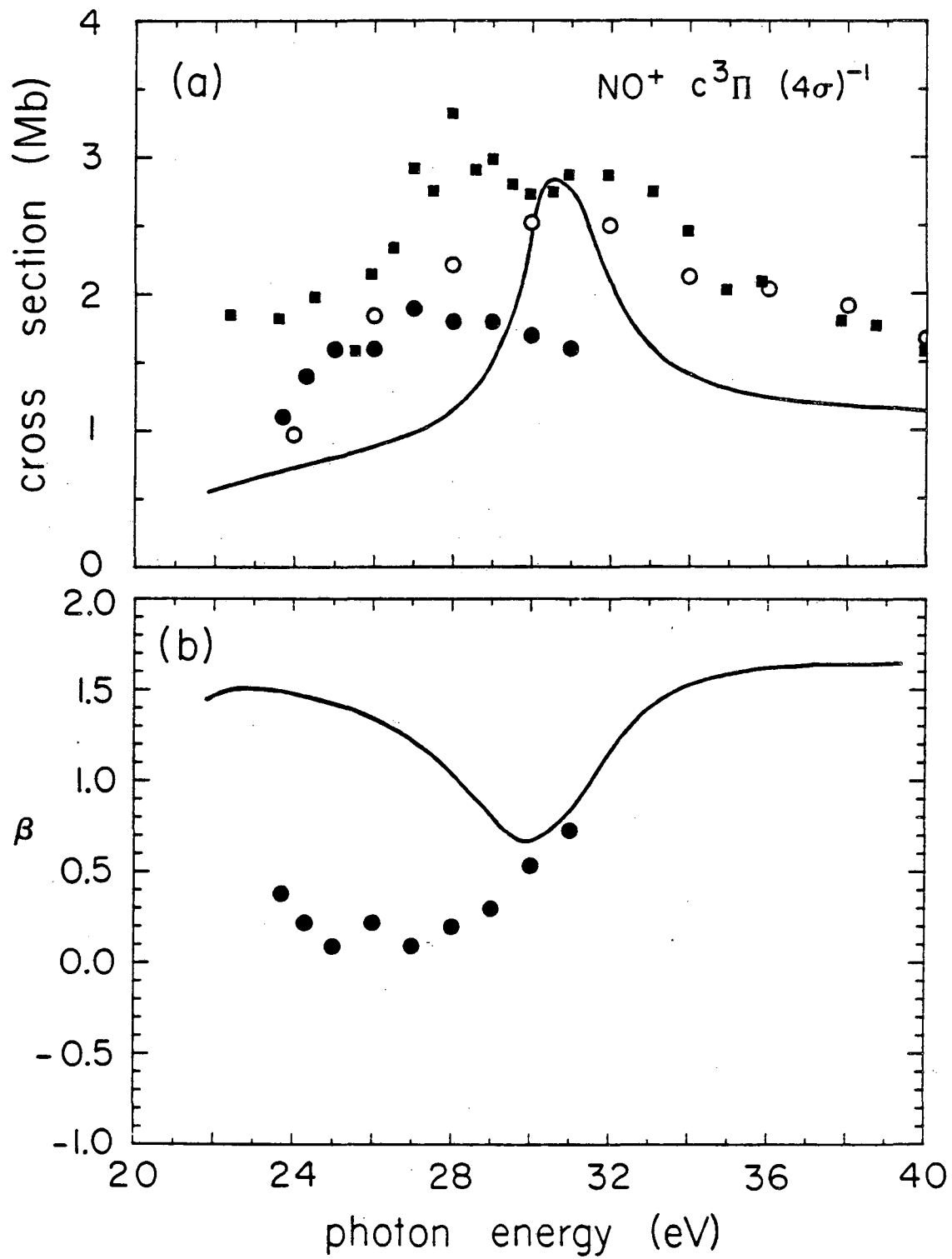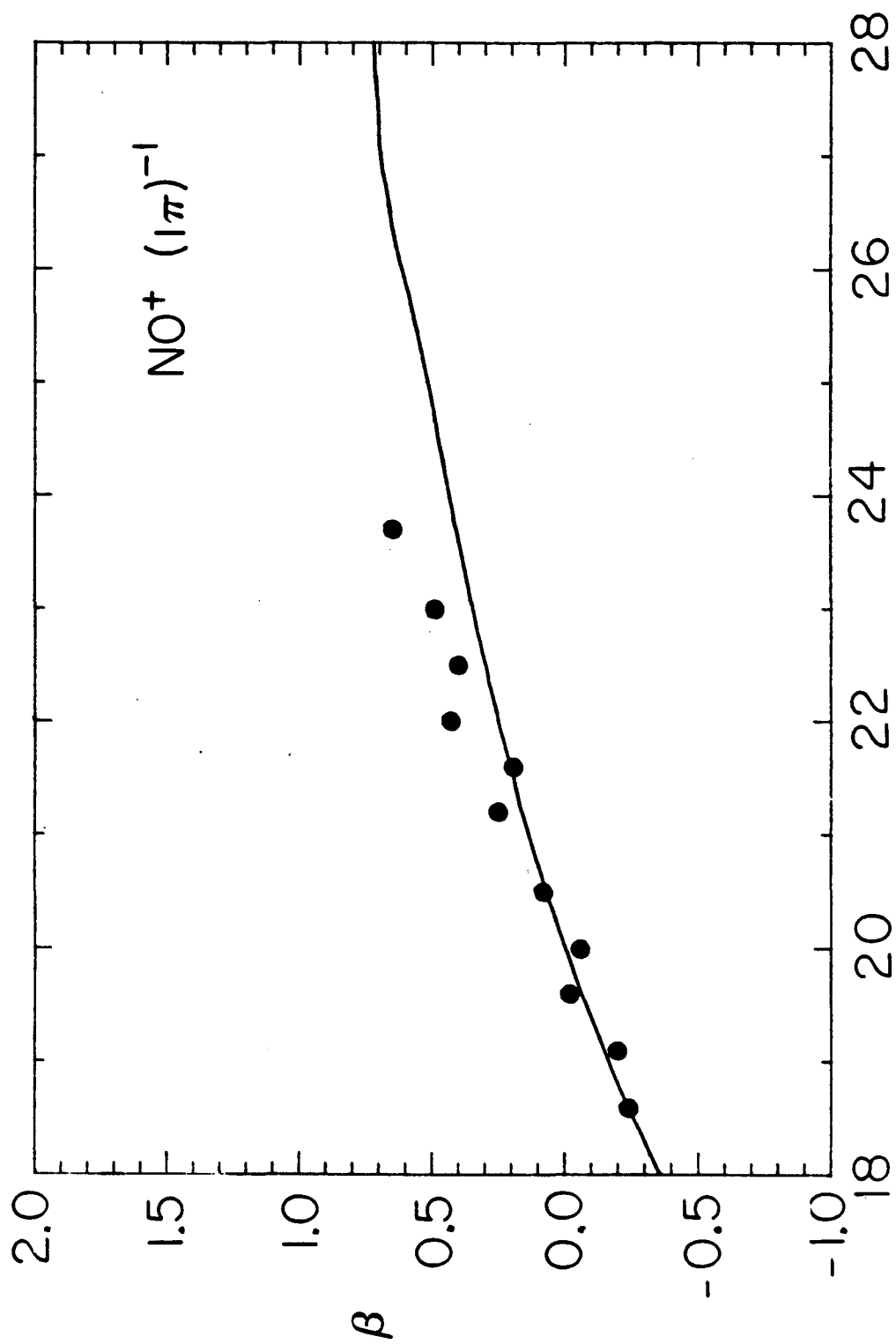
Figure 6

ACKNOWLEDGEMENTS

I am grateful to Vic Rehn, Jo Stöhr, Rolf Jaeger, and Brad Pate, who shared their knowledge and experience in aligning and operating the beam line optics and monochromators. Thanks also to the SSRL staff for their long hours on the job and generous assistance.

I thank two special ladies, Wini Heppler and Barbara Moriguchi, for their work well done and especially their friendship. Finally, I thank Connie Silva, Jean Wolslegel and June DeLaVergne for their skillful work in typing this manuscript.